2013 NSF/REU

Research Experience for Undergraduates in Physics

Notre Dame Science

The College of Science at the University of Notre Dame

Student Research Papers

Volume 24

REU Director

Umesh Garg, Ph.D.

REU Student Research Papers – Summer 2013
University of Notre Dame – Department of Physics

iLocater Mechanical Design

Michelle Berg

2013 NSF/REU Program
Physics Department, University of Notre Dame

Advisor: Dr. Justin Crepp

To Table of Contents

ABSTRACT

The infrared Large Binocular Telescope Exoplanet Recovery, iLocater, spectrometer is an instrument that will be built for use at the Large Binocular Telescope (LBT) Observatory to discover exoplanets around local M dwarf stars. The mechanical design for iLocater is based primarily off of the designs of the Palomar High Angular Resolution Observer (PHARO) and Project 1640 (P1640). iLocater is a fiber fed instrument and will be made almost entirely of aluminum alloy 6061-T6. It will be operating in the near infrared which forces the detector to be cooled to cryogenic temperatures and housed in a vacuum. Pictures and dimension for each part are included. Smaller aspects of the design need to be reviewed, and frequency and thermal simulations need to be run to test the instrument design.

Key words: Radial velocity, M dwarf, Spectrograph, Y-band, SOLIDWORKS

1. INTRODUCTION

The Doppler Effect, which enables the detection of planets through the shift of the emission spectrum of the host star, allows scientists to determine the orbital period and mass of these exoplanets (Mayor & Queloz 1995). *Kepler* has found many planets using the transit technique, and its findings provide the surprising conclusion that there is a larger occurrence of small planets around low mass stars, particularly M dwarfs (Howard et al. 2012, Muirhead et al. 2012). Furthermore, multiple planet systems are found more commonly around M dwarfs than any other type of star (Muirhead et al. 2012). M dwarf stars are the most common type of stars in the universe and are fortunately located close to the galactic plane and relatively nearby to the earth, making them easier to observe (Howard et al. 2012, Swift et al. 2012).

To Table of Contents

With the expansive list of planets found by *Kepler*, follow up ground based observations are now needed to determine if any of these planets are actually hospitable (Charbonneau et al. 2009). Because the population of planets is greater around M dwarfs, the possibility of finding a habitable planet orbiting this type of star is very likely. Extremely sensitive ground based spectroscopic observations of the radial velocity of the star is the best way to determine the characteristics of a planet and see if it is located in the habitable zone (Charbonneau et al. 2009).

The infrared Large Binocular Telescope Exoplanet Recovery, iLocater, spectrometer is a fiber fed instrument that will be built for use at the Large Binocular Telescope (LBT) Observatory. Due to the "extreme" adaptive optics system of the LBT, the radial velocity measurements of iLocater will be diffraction limited. iLocater will be operating at near infrared (NIR) wavelengths in the Y-band (.95 – 1.13 μm), which is free of telluric absorption (Reiners et al. 2010), to observe M dwarf stars. Because of the 110.8 m^2 of collecting area of the LBT and its ability to use one dish to monitor radial velocity shifts, iLocater will be able to make precision measurements of the host star's radial velocity to find planets in the habitable zone.

2. MECHANICAL DESIGN

iLocater will use the HAWAII-2RG (H2RG) detector supplied by Teledyne (Figure 9). It has a 2048 x 2048 pixel array with an 18 x 18 μm^2 pixel area (Beletic et al. 2008, Hawaii-2RG Technical Manual). When operating at 77K, its median dark current is $\leq$ .05 e-/s, and its median readout noise at 100 KHz readout rate is $\leq$ 18 e- (H2RG Product Sheet). Because this detector is operating in the IR, it must be cooled down by liquid nitrogen (LN_2) to 77K to prevent it from being saturated by thermal excitation. Lovis and Fischer (2011) also point out that variations in the index of refraction of air and thermal and mechanical effects of the instrument need to be corrected for to achieve high-precision radial velocity measurements.

The Infrared and Electro-optical Systems Handbook provides solutions to these problems. To combat changes in the ambient temperature and pressure, the spectrograph and optics will be placed in a vacuum chamber. Because the detector is so sensitive to movement, it needs to be isolated from vibrations; the instrument will be placed on a vibration isolation table which has pneumatic isolators in each leg (Erin et al. 1998). As an added measure, the instrument will be placed on pneumatic mounts to elevate it from the table. The addition of multilayer insulation (MLI) within the vacuum chamber, surrounding the detector and optics, will also reduce thermal radiation. MLI acts as a low emittance radiation shield that reduces temperature fluxuations (Lyle et al. 1973). Thermal radiation is minimized by reflective surfaces in the MLI, and thermal conduction is minimized by a spacer material (Gilmore 2002).

Most materials do not operate well at cryogenic temperatures. Marquardt et al. (2001) instructs that metals with lower thermal conductivity coefficients, higher specific heat, and small thermal expansion coefficients will work optimally in low temperature environments. Aluminum alloy 6061-T6 and stainless steel 304 are some of the best metals to use at cryogenic temperatures as seen in Figure 1. These metals also have some of the lowest outgassing rates (Danielson 2003). Outgassing is the process of releasing gas that is trapped or adsorbed in a material. This effect will decrease the vacuum and could lead to convection within the chamber (Danielson 2003). These materials are the two most commonly chosen for any instrument that operates at cryogenic temperatures. iLocater will be made almost entirely of aluminum alloy 6061-T6.

The designs of PHARO and P1640 gave a basis for iLocater's design. The details of these designs can be found in Hayward et al. (2001), Hinkley et al. (2010), and Hinkley et al. (2011). Figure 2 shows the design of P1640 and what is encompassed by the vacuum. For iLocater, the

3D Computer Aided Design software SOLIDWORKS was used to design the instrument. The optical design of the spectrograph is a double pass shown in Figure 3.

Figure 4 shows the full instrument, and Figure 5 shows a cutaway view of the instrument. The dimensions are .777m x .477m x .347m, and the weight without LN_2 is 264.47 lbs. The

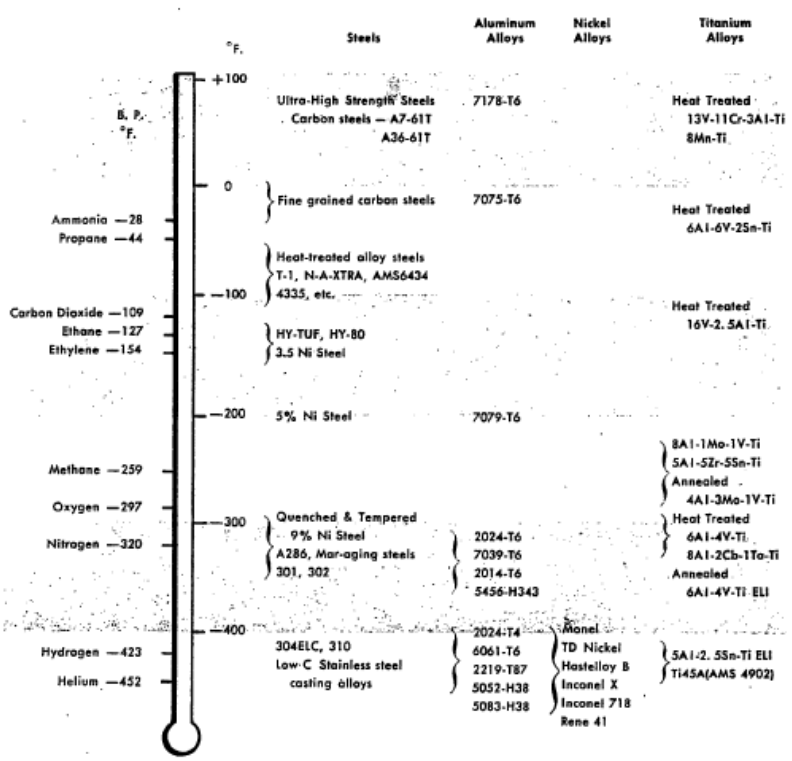

Figure 1. A listing of metals suitable for use at specific temperatures (Hurlich 1968). Aluminum alloy 6061-T6 and stainless steel 304 are some of the best metals for use at cryogenic temperatures.

optics sit on a breadboard that is .62m x .32m x .0254m with holes for optical mounts spaced 1in apart and .75in in from the sides (see Figure 6). There are only four points where the optical components are in contact with the outer shell (blue) and hence the ambient room temperature. Four G-10 fiberglass tabs, Figure 7, connect the breadboard to the outer shell. This material is a super insulator and will therefore suppress any temperature change to the optics and detector through thermal contact. Their dimensions are .0381m x .00556m x .000508m. The tabs become thinner in the middle where their thickness is .00278m.

To Table of Contents

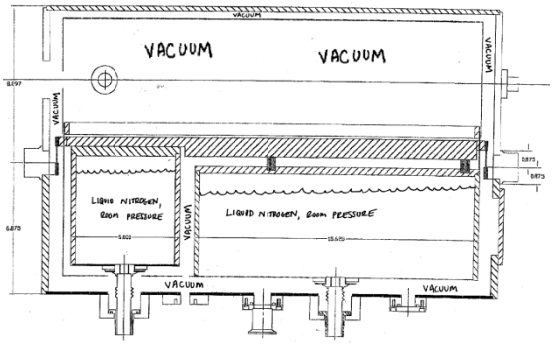

Figure 2. This sketch of the inside of P1640 shows what is encompassed by the vacuum (Hinkley et al. 2010).

Figure 3. iLocater has a double pass optical design that was created using the ray tracing program Zemax.

Figure 4. This is the outside view of iLocater. The dimensions are .777m x .477m x .347m, and it weighs 264.47 lbs.

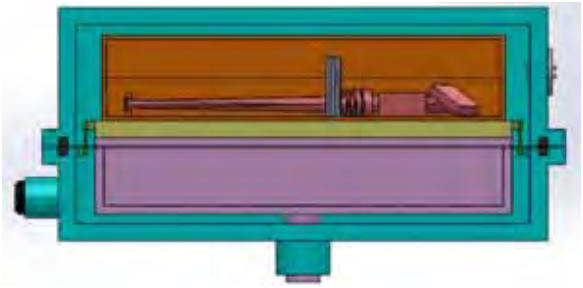

Figure 5. The inside of iLocater is seen in this cutaway view.

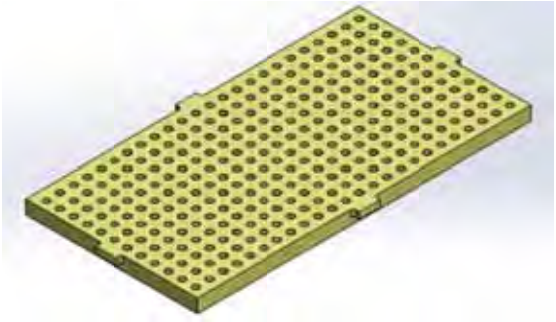

Figure 6. This is the breadboard the optics will be mounted on. It is .62m x .32m x .0254m with holes for optical mounts spaced 1in apart and .75in in from the sides.

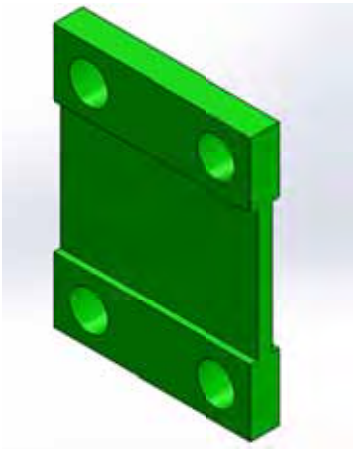

Figure 7. The super insulating G-10 fiberglass tabs will be the only points of contact between the optics and casing.

To Table of Contents

The purple LN_2 can in Figure 5 is .62m x .32m x .1127m with wall thickness .0127m. The tube for filling the can extends .1016m from the bottom and has an outer radius of .025m and inner radius of .02m. The volume that the can will hold is 15.34 L of LN_2. The can will be bolted to the bottom of the breadboard so the optics and detector will be cooled through thermal contact. The brown radiation shield in Figure 5 is made of MLI and surrounds the optics and detector. It is .6m x .3m x .1281m with wall thickness .00635m. In Figure 8 the detector (purple) and its housing are shown. This is not the final design, but was put in to help aid in understanding where the detector is located within the setup of the optics.

The length and width of the outer casing are .726m x .426m, but each section has a different height. The bottom is .1397m high, and the top is .2073m high, for a total instrument height of .347m. The walls are 1in thick and have a flange that is also 1in thick. Including the flange, the length and width are .777m x .477m. The black lining is an O-ring that is .5in thick that helps seal the casing and prevent air leaks in the vacuum. The screw holes on the flange are .1087m apart lengthwise and .115m apart widthwise. The bottom shell has two ports that extend

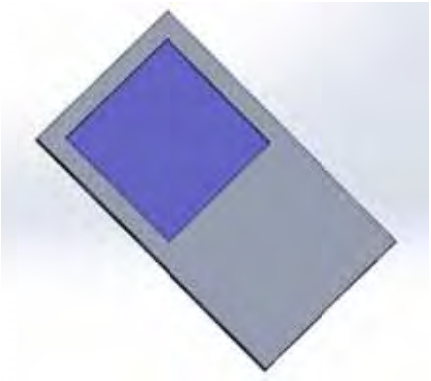

Figure 8. This is the sample detector and housing used to understand where the detector will be placed within the optics.

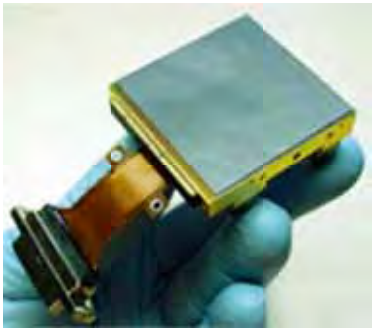

Figure 9. iLocater will use the HAWAII-2RG detector from Teledyne to make observations.

.0508m from the side with an outer radius of .03m and inner radius of .25m that will be used for the vacuum pump and vacuum gauge. A sample gauge is shown in Figure 10. The port extending .0508m from the bottom of the shell has an outer radius of .04m and inner radius of .03m. This port lines up with the port on the LN_2 can. The top casing has only one port of radius .025m which will be closed with the hermetically sealed feedthrough in Figure 11. The fiber optic cable will enter the chamber through the feedthrough, and the electrical information from the detector will come out. The smaller radius of the feedthrough is .025m, and the larger radius is .035m. The feedthrough is .03175m high. The two ports extend .005m off of the front and back and have an outer radius of .03175m and inner radius of .0015875m. The screw holes are placed .025m apart from each other.

Figure 12 shows a sample vibration table with pneumatic mounts elevating the instrument 5.5in above the table top. The table is modeled after the Newport M-RPR-36-8 vibrational isolation table that is .9m x 1.8m x 203mm. There is limited space where iLocater will be housed at the LBT, so a model of the room, Figure 13, was created make sure it would fit. The model person is 6ft tall, and the room space is 160in across and 140in back, though this length is shortened to 100in due to piping extending from the wall.

Figure 10. A sample vacuum gauge that measures the pressure inside the vacuum chamber.

Figure 11. The hermetically sealed feedthrough will feed the fiber optic cable to the optics inside the chamber.

Figure 12. iLocater on the sample vibration isolation table with pneumatic mounts.

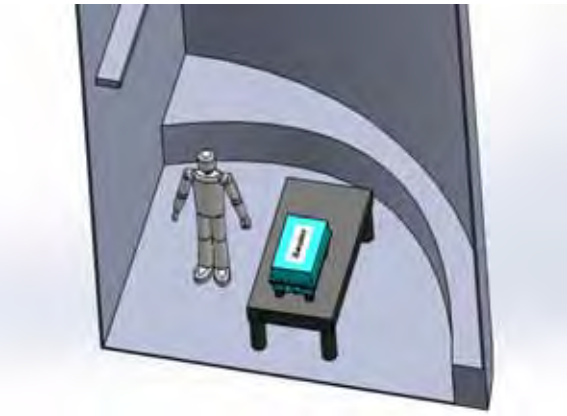

Figure 13. iLocater inside the simulated room at the LBT with a 6ft person.

3. CONCLUSION

The basic design of iLocater has been created, but there are still many smaller items that need to be decided upon like the types of screws that will be used to close the casing, sensors inside the chamber to monitor temperature and pressure, and a filter to only pass the Y-band wavelengths to the optics. There are also many considerations given by Teledyne to ensure the detector will perform at maximum efficiency, such as what type of metal the detector should be mounted on, which is covered in their Handling Manual. We also need to test how the materials act at cryogenic temperatures and to what extent the enclosure will be affected by vibrations. SOLIDWORKS has the capability to test the instrument through simulations in these areas, which will help determine if the design needs to be changed. The vibration simulation will be the most important; the space where iLocater will be housed is located by an elevator shaft, so it is crucial that it is isolated from those vibrations.

REFERENCES

Beletic, James W., et al. "Teledyne Imaging Sensors: Infrared Imaging Technologies for Astronomy & Civil Space." *Proc. SPIE*. Vol. 7021. 2008.

Blotter, P. and Batty, J. “Thermal and Mechanical Design of Cryogenic Cooling Systems.” *The Infrared & Electro-Optical Systems Handbook. Electro-Optical Components, Volume 3*. Rogatto, William D.,

Joseph S. Accetta, and David L. Shumaker. Ann Arbor, MI: Infrared Information and Analysis Center, 1993. 343-433. Print.

Charbonneau, David, et al. "A super-Earth transiting a nearby low-mass star." *Nature* 462.7275 (2009): 891-894.

Danielson, Phil. “Choosing the Right Vacuum Materials.” *R&D Magazine* (2003).

Donabedian, M. et al. “Insulation.” *Spacecraft Thermal Control Handbook, Volume I: Fundamental Technologies*. Gilmore, D. Reston, VA: American Institute of Aeronautics and Astronautics, 2002. 161-205. Print.

Erin, C., B. Wilson, and J. Zapfe. “An Improved Model of a Pneumatic Vibration Isolator: Theory and Experiment.” *Journal of Sound and Vibration,* 218.1 (1998): 81-101.

H2RG SCA Handling Manual. Thousand Oaks, CA: Teledyne Scientific & Imaging, LLC, 2010.

HAWAII-2RG Product Sheet. Thousand Oaks, CA: Teledyne Scientific & Imaging, LLC, 2012.

HAWAII-2RG Technical Manual. Thousand Oaks, CA: Teledyne Scientific & Imaging, LLC, 2009.

Hayward, T. L., et al. "PHARO: A Near-Infrared Camera for the Palomar Adaptive Optics System." *Publications of the Astronomical Society of the Pacific* 113.779 (2001): 105-118.

Hinkley, Sasha, et al. "A new high contrast imaging program at Palomar observatory." *Publications of the Astronomical Society of the Pacific* 123.899 (2011): 74-86.

Hinkley, Sasha, et al. *Project 1640 Design and Operations Documentation.* 2010.

Howard, Andrew W., et al. "Planet occurrence within 0.25 AU of solar-type stars from Kepler." *The Astrophysical Journal Supplement Series* 201.2 (2012): 15.

Hurlich, A. “Low Temperature Metals.” *Proc*. 1968.

Lovis, Christophe, and D. Fischer. "Radial Velocity Techniques for Exoplanets." *Exoplanets* (2010): 27. Print.

Lyle, Robert, Periklas Stabekis, and Robert Stroud. *Spacecraft Thermal Control.* Vol. 8105. National Aeronautics and Space Administration, 1973. Print.

Marquardt, E. D., J. P. Le, and Ray Radebaugh. "Cryogenic Material Properties Database." *Cryocoolers 11*. Springer US, 2002. 681-687. Print.

Mayor, Michel, and Didier Queloz. "A Jupiter-mass Companion to a Solar-type Star." *Nature* 378.6555 (1995): 355-359.

Muirhead, Philip S., et al. "Characterizing the cool KOIs. III. KOI 961: a small star with large proper motion and three small planets." *The Astrophysical Journal* 747.2 (2012): 144.

Reiners, A., et al. "Detecting planets around very low mass stars with the radial velocity method." *The Astrophysical Journal* 710.1 (2010): 432.

Swift, Damian C., et al. "Mass-radius relationships for exoplanets." *The Astrophysical Journal* 744.1 (2012): 59.

Damage of DNA in DNA-Gold Nanoparticle Mixture by Atmospheric Pressure Plasma Jet

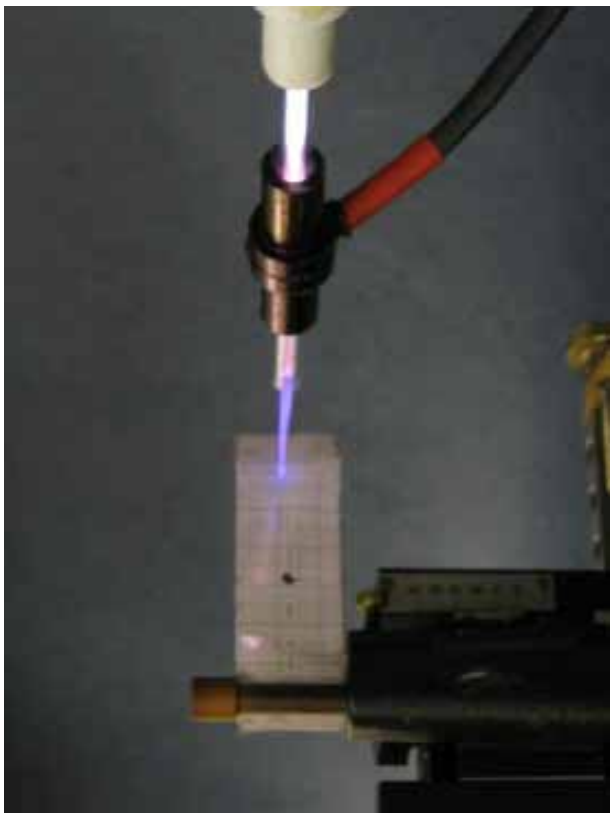

Elissa Canseco

2013 NSF/REU Program

Physics Department, University of Notre Dame

Radiation Laboratory

Advisor: Sylwia Ptasinska

Abstract

Plasma healthcare has made pronounced scientific encounters that are revealed clearly in many areas such as medicine, food safely, environmental hygiene, and cosmetics [1]. In medicine, the plasma synergy with gold nanoparticles (GNPs) could possibly yield greater DNA damage in tumor cells than that inflicted solely by the plasma. Our previous research that utilized Atmospheric Pressure Plasma Jet (APPJ) showed a high increase of strand breaks in DNA treated by APPJ [2]. It is well known that the addition of GNPs, which can penetrate biological tissue, has a significant potential as a treatment for infectious diseases and cancers. In the present work, our attention is on the use of APPJ and GNP, we compare qualitatively and quantitatively damage to DNA during APPJ exposure with and without GNPs in samples. The conclusion came through qualitative analyses via a standard gel electrophoresis technique for identifying damage in DNA samples. We are focused on the effects of the APPJ with the addition of gold nanoparticles at different times of plasma exposure, GNP concentrations, and distances from the plasma source. We have found that using both technologies, i.e., plasma and GNPs, the DNA molecule experiences more breaks in its sugar-phosphate backbone.

Introduction

The atmospheric pressure plasma jet (APPJ) [3] is a nonthermal, high pressure, uniform glow over a large gas volume, and high concentrations. APPJ is composed of UV light, radicals, positive and negative charged particles. The discharge functions on a feed gas (e.g., He), which flows between electrodes, one grounded, and one with applied high voltage (HV). While applying HV, the feed gas becomes excited, dissociated or ionized by electron impact

[4]. One purpose for why the APPJ is beneficial is because even though the electrons and other species which are formed are hot due to their high kinetic energy, the overall gas is at room temperature. In this way, APPJs are very attractive tools for the surface modification of temperature-sensitive materials. These plasmas destroy most surfaces they are applied meanwhile the plasmas functions at extraordinarily high temperatures and yield significant concentrations of ions. The APPJ ability to work with temperature-sensitive materials can far along be used to treat living tissue, which may possibly damage the DNA if the temperature is raised. Nonthermal atmospheric pressure plasmas can be used for biomedical applications such as in dentistry in which it is used for teeth bleaching, [5] and in material treating such as cleaning off surfaces. [6] In the case of micro plasmas, they have been found to be able to "inactivate microorganisms and destroy biomolecules," such as DNA and proteins. Hence, plasma has increased the purpose of a "bactericidal" agent and "decontamination technology to address contamination of surgical instruments. [7]"

The issue that scientists are falling upon is in regards to using plasma in the clinic in the abrupt future is that the mechanism by which plasma works on DNA and other biological molecules is unidentified. Further analyses have originated that plasma can be used to destroy tumors [7]. Plasma can cause a widespread arrangement of species and subsequently process by which plasma attacks DNA can happen through numerous mixed response pathways. In essence, the synergy of low-temperature plasma (APPJ) could aim for a great impact on modern medicine.

Gold Nanoparticles (GNP)

Nanotechnology is one of the widespread zones of scientific investigation, particularly for medical applications. Nanoparticle size allows them to infiltrate almost-anywhere but the toxicity still represents an area of considerable uncertainties. Gold nanoparticles remarkable ability to penetrate tissues brings a great potential as a treatment method for infectious diseases and cancers. Understanding the plasma and nanoparticles alone can demonstrate their individual potential for medicine and have different effects but at the same time challenge the same encounters in biomedicine. As nanoparticles have the capability to penetrate tissue; the plasmas stem from their non-equilibrium reaction chemistry with very high level of chemical dissociation. This concludes and highlights that with synergizing plasmas and nanostructures which can be comprehended when nanoparticle are fabricated within a low-temperature plasma and transported by the plasma to a disease target, a technology known as plasma nanotechnology. [9]

Materials and Methods

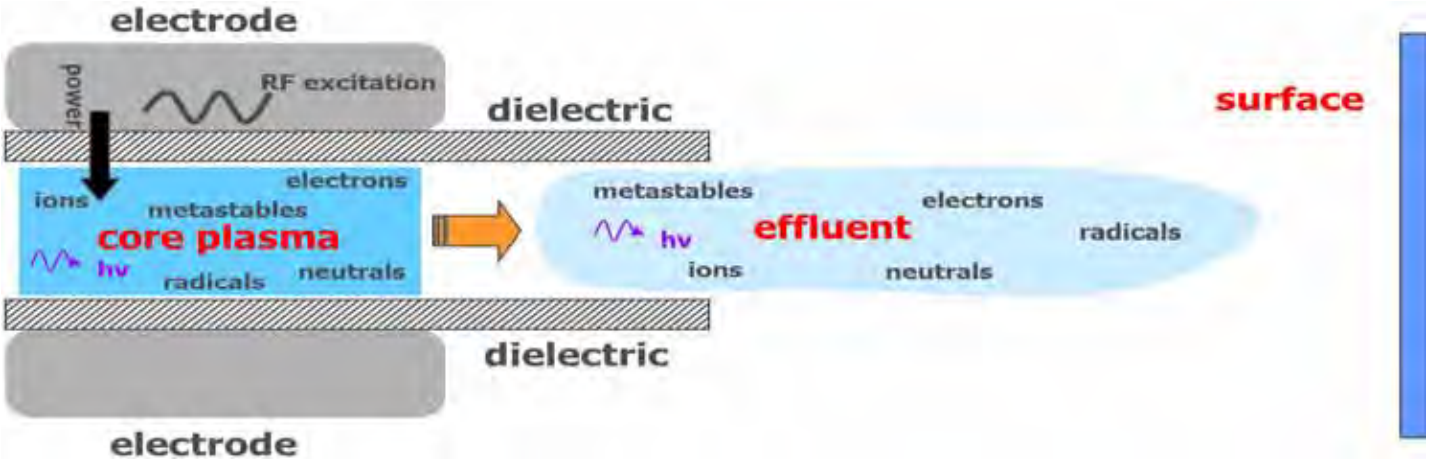

Figure 1: The APPJ: Scheme indicating the complexity of the diagnostic problem of the combined system of discharge core and effluent.

The Atmospheric Pressure Plasma Jet

APPJs are very attractive tools for the surface modification of temperature-sensitive materials. The source contains two tubular metal electrodes divided by a 3 cm gap through which a discharge current transpires once one of the electrodes is connected to the high voltage (HV) power supply. Within the electrodes lies a quartz cylindrical tube through which helium flows. To generate the plasma, we selected a specific shape of wave pulse, the frequency of pulses and the rate of helium gas flow. These considerations ensure the most stable form for the APPJ plasma. The flow rate used was 4.0 L/min, square pulse, voltage 10.8 kV, current 12 mA, and a frequency of 2.3 kHz. The plasma is launched through the exposed end of the quartz cylindrical tube into the sample with the addition of gold nanoparticles. The sample is irradiated at different times of plasma exposure, GNP concentrations, and distances from the plasma source.

DNA-GNP sample

First, we use the plasmid DNA, add the GNPs and place the solution in the microcentrifuge tube. Next we place the DNA-GNP solution into the silicate glass wells than irradiate the sample. After the irradiation, we recover the sample irradiated using PBS buffer three times for a total of 15μL of buffer. Finally we deposit sample to gel electrophoresis to run and analyze using the UV analyzer.

In the experiment we always run three different controls. “Freezer” which is only DNA with distilled water and is not irradiated. “Ice” is kept alongside with the other samples when they are being irradiated but is never taken out or irradiated. Our last control is the “flow gas

control;" we do not use the plasma but only treat the sample with helium gas. The reason for the flow control is to disregard the possibility of the helium stream causing damage to the sample.

Gel Electrophoresis

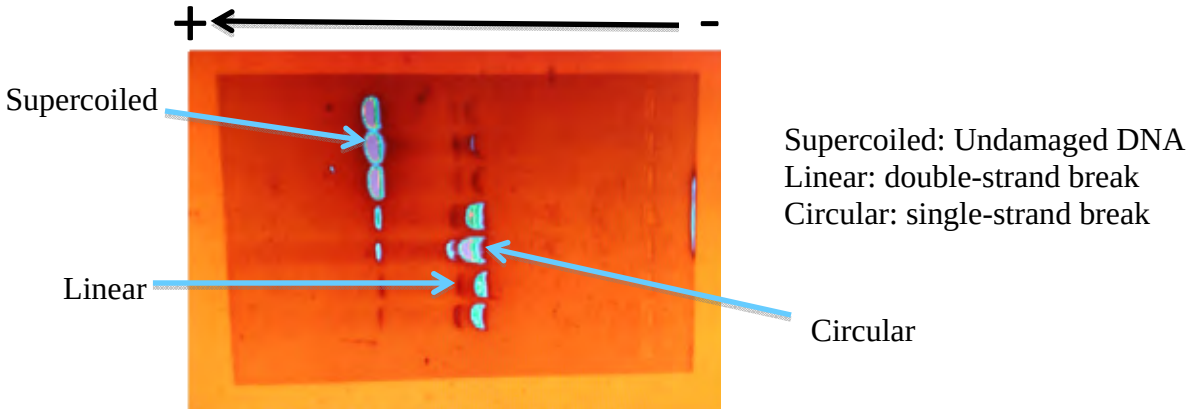

Figure 2: Example of a gel under the UV analyzer

After irradiation, we place all samples in their separate microcentrifuge tube and a dye is added to each sample; 3 µL of dye is added "freezer" and "ice "controls, 5µL is added to the rest of the samples. The different amount of dye is added due to the amount of sample is in the tube. Add sample into the gel which is in the electrophoresis chamber. We have two sizes of apparatus chambers and each one requires different times and voltage, depending on the number of samples needed.

The gel electrophoresis chamber consists of a positive and a negative electrode placed in opposite ends. Once the correct voltage is applied it separates the molecules according to the charge and size. DNA is negatively charged and therefore runs toward the positive electrode. The agarose matrix gel is porous, smaller fragments will travel faster than the larger fragments.

Supercoiled travels faster do to its small fragment size; supercoiled is undamaged DNA. The slowest is single strand break due to the form it adopts which is a hoop conformation. The double strand break adopts a linear conformation. The electric field within the gel electrophoresis chamber will separate the supercoiled, single strand break, and double strand break from each other. The separation of strands will be visible when the gel is viewed under UV light.

Image Analysis

To be able to analysis the gel it is placed inside the Trans UV analyzer and the Origin One program is used to provide the numerical values for the intensity of the bands and provides the quantity of DNA-GNP sample. The agarose gel is prepared by mixing TBE, argrose powder, boiled (microwaved), cooled to 60ºC, and then SYBR Green is added; the SYBR Green is used to make the band fluorescent under the UV light.

Results

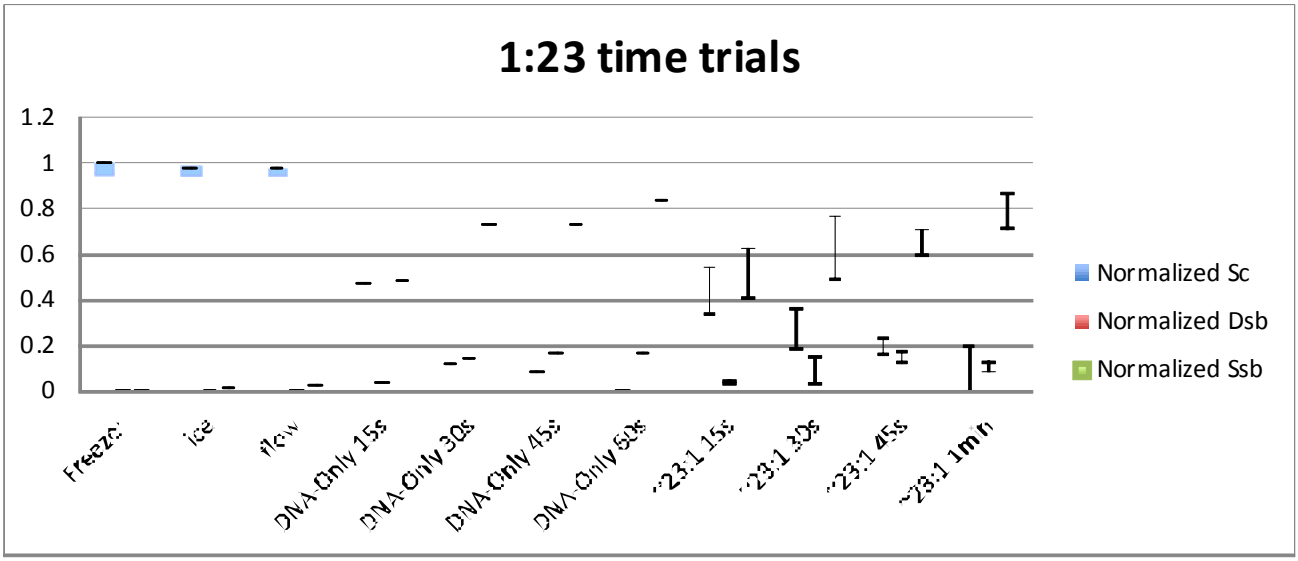

Figure 3: DNA-GNPs time duration under the APPJ source

Figure 3 shows the results of DNA-GNPs at different times. The mixture is using the maximum number of GNPs to one DNA particle. In the trial we had three controls, four DNA at different times and four DNA-GNPs mixture at different time ranges. In the graph for the average time trials we see as the sample is left under the source the increase of single and double strand increases.

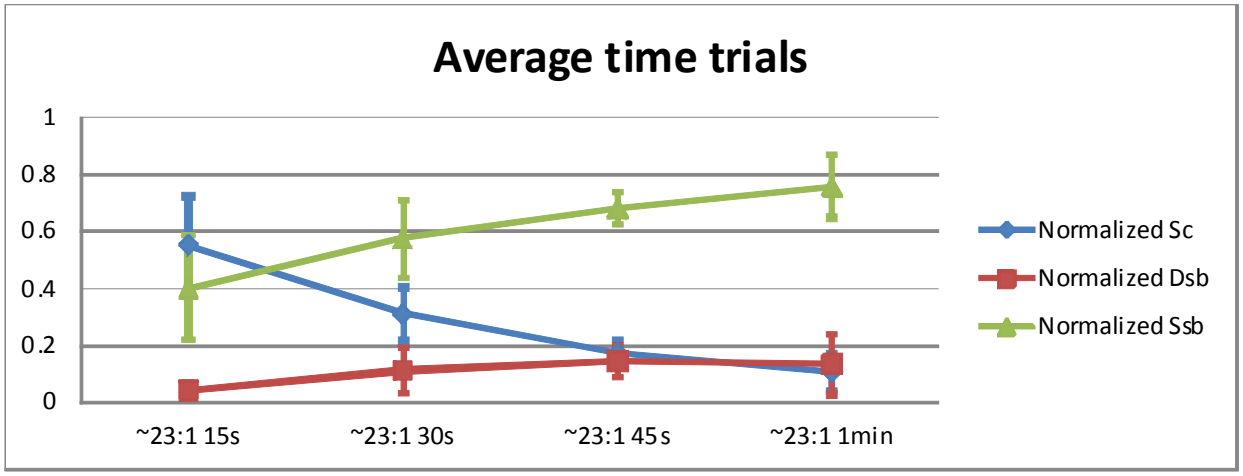

Figure 4: Average time trials of normalized data

The following data give the normalized data results for the different exposure time with the DNA-GNP mixture at its maximum amount of GNPs. In the data two trials were done and of each time six samples were irradiated. The data shows us that as the time is increased the number of supercoiled (undamaged DNA) is decreasing and the number of double stand breaks is increasing.

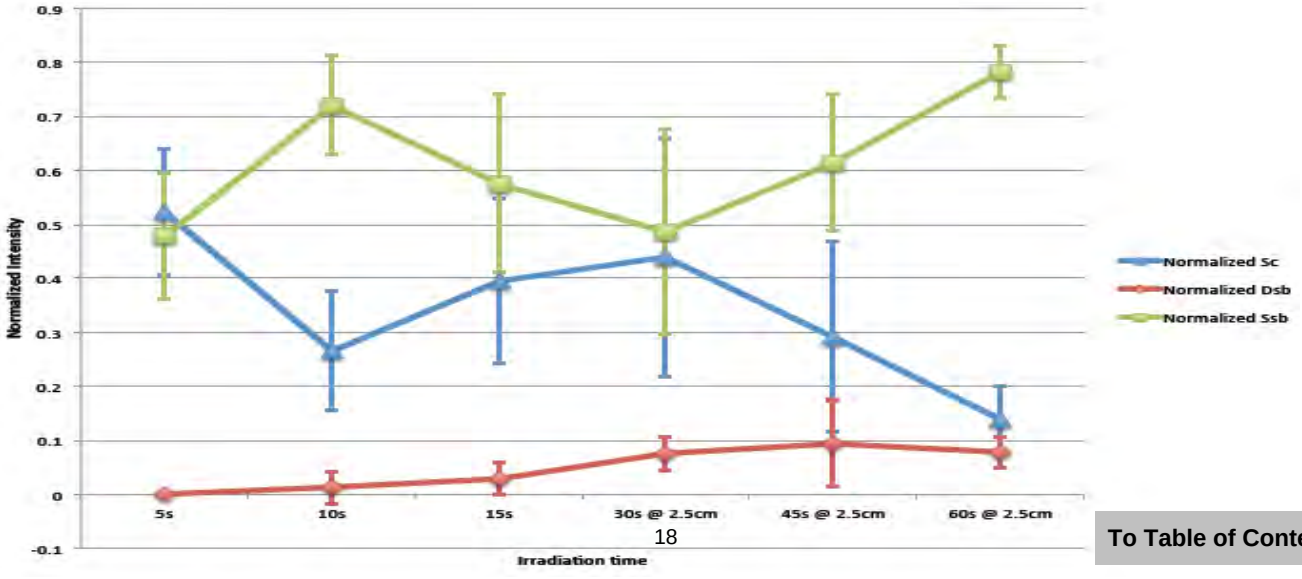

To Table of Contents

Figure 5: DNA only for different time durations under the plasma source

In the figure of DNA only we use to compare with our data of DNA-GNP solution, to see the increase or decrease of damage to the DNA. The figure shows an increase of single strand break it is under the plasma source for a long time period.

Discussion and Conclusion

The synergy of plasma and nanoparticles aims to take advantage of distinct and different strengths of each of the two technologies in terms of reactivity, safety and disease targeting. Its benefits go well beyond the simple combination but they each take a different roll.

In the results taken the past ten weeks we have seen different types of feedback and more trials and further experiments have to be taken in order to get a better understanding of the correlation between the GNPs and the APPJ.

The Ptasinska lab will remain with the DNA-GNP research and correspondingly asses the special effects of the APPJ directly on cancer cells. This research will help build new frontiers in the chiasm amongst plasma physics and medical applications to cure cancer and other disorders.

Acknowledgements

I would like to thank the Radiation Lab and especially Dr. Sylwia Ptasinska, my mentor. Xueqiang Zhang a graduate student, and Alex Cantrel undergraduate student for all their help and support. Thank you to the University of Notre Dame and particularly to Dr. Umesh Garg and the National Science Foundation for providing me the opportunity to conduct the research for the summer.

References

G E Morfill *et al* 2009 *New J. Phys.* **11** 115011 DOI:10.1088/1367-2630/11/11/115011

S Ptasinska et al. 2010 *Phys Chem Chem Phys*. **12** 7779 **DOI:** 10.1039/C001188F

A. Schütze, J. Y. Jeong, S. E. Babayan, J. Park, G. S. Selwyn, and R. F. Hicks, IEEE Trans. Plasma Sci. **26**, 1685 (1998).

H. W. Herrmann, I. Henins, J. Park, and G. S. Selwyn *Physics Division, Los Alamos National Laboratory, Los Alamos, New Mexico 87545*

Lee, Hyun Woo et al. (2009) Tooth bleaching with nonthermal atmospheric pressure plasma. *JOE* (587- 591)

Belkind, A. and Gershman S. (2008) Plasma Cleaning of Surfaces. *Vacuum Technology and Coating.*

Felipe Iza, et al. (2008). Microplasmas: Sources, Particle Kinetics, and Biomedical Applications. *Plasma Processes and Polymers*, 322- 344

Agnieszka Stypczynska, et al. (2010) The influence of amino acids on DNA damage induced by cold plasma radiation. *Physics Letters,* 500(4-6), pp. 313- 317

Kong, M.G., Keidar, M., Ostrikov, K. 2011. Plasma meets nanoparticles-where syngergies can advance the frontier of medicine. Journal of Physics D: Applied Physics, 44, 174018.

iLocater: Binary Stars Science Case

Taylor Corpuz
2013 REU Program
Physics Department, University of Notre Dame
Advisor: Justin Crepp

To Table of Contents

Abstract

This science case describes how the iLocater spectrometer can be used to detect and study extrasolar planets around stars in multiple systems, specifically binary stars, using the radial velocity method. Its several advantages include its location at the Large Binocular Telescope, the adaptive optics system, and its stable design. Binary stars offer a unique testing ground for current theories of planet formation, such as core accretion and disc fragmentation. iLocater will also be able to increase the current sample size of planets in multiple systems, giving the opportunity to confirm trends seen in the current sample, such as different mass-period and eccentricity-period distributions.

1 Context

iLocater, or the **I**nfrared **L**arge Bin**oc**ul**a**r **T**elescope **E**xoplanet **R**ecovery spectrometer, is a detector being developed for the Large Binocular Telescope (LBT) in Arizona. It will receive light in the near-infrared wavelengths (from .95–1.10 μm) [Crepp, 2013] and will use that to detect planets around other stars with the Doppler method.

iLocater's location at the LBT gives it several distinct advantages. The LBT has the largest collecting area of any telescope, giving it the highest spatial resolution, and its two mirrors allow for the monitoring of internal radial velocity drifts. Its "extreme" adaptive optics (AO) correction at near-infrared wavelengths gives iLocater the opportunity to be the world's first diffraction-limited spectrometer. Attaining such a high spectral resolution provides for a smaller size when compared to other instruments, leading to greater optical and thermal stability, less expensive optics, and a design that can use a single-mode fiber that will eliminate modal noise.

By using the radial velocity method to find extrasolar planets, iLocater has the ability to more easily detect planets in multiple star systems compared to other methods such as the transit method. The spectrometer also effortlessly determines the metallicity of

target stars, which is essential as high-metallicity stars have been found to be more likely to host planets. iLocater's high spectral resolution allows for the observation of binary stars with separations of less than 1", allowing for the exploration of a new area, as current Doppler surveys are biased against binaries with a separation closer than 2–6" [Eggenberger, 2010].

2 Science Goals

iLocater has three main science goals. The first will utilize its precision in the near infrared to find and observe planets around M-dwarf stars, as their black body radiation curves peak in such wavelengths. Another will involve following up on candidate planet-host stars discovered by NASA's TESS (Transiting Exoplanet Survey Satellite) telescope.

The focus of this paper is iLocater's goal to gather data regarding the formation of giant planets around both the components of binary stars and binaries themselves. This is done by increasing the current sample size of planet-hosting binary stars and searching for stellar companions to existing planet hosts. Increasing our sample size will allow us to determine the frequency of such planets, test theories for giant planet formation, and confirm or refute current trends seen in the existing sample of extrasolar planets in binary or multiple systems.

3 Background

3.1 Binary Stars

About one third of stars in the Milky Way have at least one stellar companion. This means that they are gravitationally bound to another, ranging from those with periods of thousands of years to those that are so close they exchange matter. Solar-type stars are actually more likely to be found with a stellar companion than alone [Eggenberger, 2010].

This signifies that stars in multiple systems, given their abundance, must be studied alongside and with as much vigor as single stars, especially in regard to planet formation.

The transition area from close to wide, common proper motion binaries is about 200–300 AU [Desidera and Barbieri, 2007]. Very wide binaries, those with separations of 1000 AU or more, act very much like single stars. As the separation between the two stars shrinks, they interact more and more until they are close enough that they even transfer mass from one to the other. iLocater will specifically look at visual binaries, where the stars are far enough apart that the spectra of both stars in the pair can be resolved individually.

3.2 Exoplanets

The idea of planets around other stars has captured everyone's imagination, from science fiction writers to scientists themselves, since before the discovery of the first extrasolar planet, 51 Peg b, in 1995. In recent years, the study of such planets has exploded with the finding of nearly 1000 planet candidates in over 700 planetary systems [Exo, 2013]. These planets stood outside existing theories of planet formation and introduced new ideas that had only been imagination. Astronomers found planets that orbit pulsars, are twice the size of Jupiter, circle their star in less than a day, and even orbit multiple stars.

Studying exoplanets gives scientists an extraordinary opportunity to explore the universe and inevitably leads to questions involving life: Is it possible on other worlds, and if so, how common is it? Observations allow for new constraints on current theories of planet formation, especially the study of extrasolar planets around binary or multiple star systems.

There are several methods of detecting planets around other stars. NASA's Kepler space observatory has been highly successful using the transit method, finding more than 3000 planet candidates and more than 100 confirmed planets [Kep, 2013]. It finds planets by measuring the brightness of target stars over time. If a planet, in the course of its

orbit, transits in front of the star, the detected flux of the star varies a small amount. From these light curves, it is possible to determine the size of the planet, the period of its orbit, the mass of the star, and an approximate distance for that star's habitable zone. It is also possible to directly image a planet around a star, especially in those with orbital planes that lie orthogonal to the line of sight, unlike those for which the transit method is used. The approach iLocater uses to search for planets is the radial velocity method, which involves using miniscule shifts in the absorption and emission lines in a stars spectrum to determine any radial velocity changes that can indicate the existence of an extrasolar planet.

There are two main theories regarding the formation of planets from a protoplanetary disk, formation that occurs via a different mechanism than what forms stars and brown dwarfs. For terrestrial planets, it is generally accepted that they form by the accumulation of solid particles due to gravity: Larger and larger planetesimals form and then collide into the formation of a solid, rocky planet. This is called core accretion and forms the first half for a model of giant planet formation. In this model, a planetesimal that reaches a critical mass will then begin to accrete gas until it carves out a swath of empty space and no more material is available. Another model for giant planet formation is disc fragmentation, in which planets form as instabilities in the protoplanetary disc collapse and clump together. Both theories would indicate that giant planets would form beyond the ice line, as ices along with rock and gas would aid in accumulating material, but this does not explain the "hot Jupiters" that have been found.

3.3 Exoplanets in Multiple Star Systems

In 1941, Isaac Asimov published "Nightfall," a story about a planet in a system with six suns. Although it seemed like the ultimate science fiction when it was published, the discovery of KIC 4862625 b, a circumbinary planet in a quadruple star system, made the idea of planets in systems similar to that in "Nightfall" a reality.

Current planet formation theories are based almost solely on data from the observation of single stars. To truly understand how planets form, it is essential to study planets in systems with more than one star, as information about them can add important constraints on current models. For example, the presence of a stellar companion is known to transfer angular momentum to the disc and truncate both its inner and outer radii [Eggenberger et al., 2004]. It is also believed that the presence of a companion when a planet is still embedded in the disc can both increase the mass accretion rate and lower the inward migration time [Udry et al., 2004]. Studying planets in binaries can then possibly confirm these theoretical predictions or create new ones.

Several models explaining the presence of hot Jupiters involve the presence of a massive third body or a stellar companion [Bechter et al., 2013]. A third body could cause the eccentricity of the other two objects to fluctuate periodically via the Kozai mechanism, thus creating inward migration of the planet. Other mechanisms include dynamical interactions with the companion star or planet-planet scattering.

4 Relevant Instrument Properties

Spectral Resolution	Wavelength Range	Spatial Resolution	Field of View
R=120,000	.96–1.11μm	20 mas	40”

5 Science Objectives

iLocater's detection and observation of extrasolar planets will be used to understand planet formation around binary stars. Currently there are about 80 planets in multiple star systems that have been discovered, and trends among them are beginning to emerge. iLocater will help increase the sample size of planets around binaries and thus allow for the confirmation of these trends or the exposure of new trends.

iLocater can be used to examine the existence of companion stars to planet-hosts or

the properties of the binary stars themselves. Planet formation has already been shown to be linked to star metallicity, which iLocater can easily study by analyzing the spectra of the target stars. The binary mass ratios and separations may also play a role in planet formation. There is currently a lack of planets in binaries with separations of 20–100 AU [Desidera and Barbieri, 2007], possibly indicating that close stellar companions exhibit a negative impact on planet formation. However, this depopulated area is also due to selection effects, as current Doppler surveys are biased against such close binaries. iLocater can investigate binaries like this and confirm or refute the trend seen.

Other distributions seem to be different between planets in binaries and planets in single stars. The mass-period distribution of planets in multiple star systems have two interesting characteristics: There are no short-period planets with a mass $M_2 \sin(i) \geq 5M_J$, and the most massive short-period planets reside in systems with at least one stellar companion [Eggenberger et al., 2004]. The lack of large short-period planets cannot be attributed to selection effects as they are the easiest planets to find via radial velocity measurements. Such massive planets with short periods could be due to dynamical interactions with the stellar companion. The eccentricity-period distribution shows that all short-period planets with $P \leq 40$ days in multiple star systems have an eccentricity of $e \leq 0.05$, far lower than those around single stars. At the same time. the largest eccentricity longer-period planets are also found in multiple star systems. Possible explanations for such trends include tidal circularization lowering the eccentricity of close orbiting planets, or the Kozai mechanism oscillating the eccentricities. A larger sample size is needed to confirm what has been seen.

6 Conclusion

iLocater's status as the world's first diffraction-limited spectrometer and its many advantages allow for many opportunities to study planet formation around binary stars. Not

To Table of Contents

only can it be used for the detection of stellar companions to planet-host stars, it also can be used for the detection of extrasolar planets themselves. Studying such planets will give scientists the chance to expand the current sample of planets in multiple star systems, test the current planet formation theories, and perhaps generate new ones.

References

[Exo, 2013] (2013). The exoplanet encyclopaedia.

[Kep, 2013] (2013). Kepler: About the mission.

[Bechter et al., 2013] Bechter, E. B., Crepp, J. R., Ngo, H., Knutson, H. A., Patygin, K., Hinkley, S., Muirhead, P. S., Johnson, J. A., Howard, A. W., Monet, B. T., Matthews, C. T., and Morton, T. D. (2013). Wasp-12b and hat-p-8b are members of triple star systems. *arXiv preprint*.

[Crepp, 2013] Crepp, J. R. (2013). ilocater. *American Astronomical Society*, 221.

[Desidera and Barbieri, 2007] Desidera, S. and Barbieri, M. (2007). Properties of planets in binary systems: the role of binary separation. *Astronomy & Astrophysics*, 462:345–353.

[Duchene, 2010] Duchene, G. (2010). Planet formation in binary systems; a separation dependent mechanism? *The Astrophysical Journal Letters*, 709:L114–L118.

[Durisen et al., 2006] Durisen, R., Boss, A., Mayer, L., Nelson, A., Quinn, T., and Rice, K. (2006). Gravitational instabilities in gaseous protoplanetary disks and implications for giant planet formation. *arXiv preprint*.

[Eggenberger, 2010] Eggenberger, A. (2010). Detection and characterization of planets in binary and multiple systems. *EAS Publications Series*, 42:19–37.

[Eggenberger and Udry, 2010] Eggenberger, A. and Udry, S. (2010). *Planets in binary star systems*. Springer.

[Eggenberger et al., 2007] Eggenberger, A., Udry, S., Chauvin, G., Beuzit, J., Lagrange, A., Segransan, D., and et al. (2007). The impact of stellar duplicity on planet occurrence and properties: observational results of a vlt/naco search for stellar companions to 130 nearby stars with and without planets. *Astronomy & Astrophysics*, 474:273–291.

[Eggenberger et al., 2004] Eggenberger, A., Udry, S., and Mayor, M. (2004). Statistical properties of exoplanets: planet properties and stellar multiplicity. *Astronomy & Astrophysics*, 417(353-360).

[Eggenberger et al., 2008] Eggenberger, A., Udry, S., Mayor, M., Chauvin, G., Markus, B., Beuzit, J., and et al. (2008). *Multiple stars across the H-R diagram*. Springer.

[Hill et al., 2007] Hill, J. M., Green, R. F., and Slagle, J. H. (2007). The large binocular telescope. *SPIE Conference*, 6267.

[Holman and Wiegert, 1999] Holman, M. J. and Wiegert, P. A. (1999). Long-term stability of planets in binary systems. *The Astronomical Journal*, 117:621–628.

[Howard, 2013] Howard, A. W. (2013). Observed properties of extrasolar planets. *Science*, 340:572–576.

[Kaib et al., 2013] Kaib, N. A., Raymond, S. N., and Duncan, M. (2013). Planetary system disruption by galactic perturbations to wide binary stars. *Nature*, 493:381–384.

[Kraus et al., 2011] Kraus, A. L., Ireland, M. J., Hillenbrand, L. A., and Martinache, F. (2011). The role of multiplicity in disk evolution and planet formation. *The Astrophysical Journal*, 745.

To Table of Contents

Using Gamma Ray Bursts to Estimate Luminosity Distances

Shanel Deal

University of Notre Dame Summer Research Experience for Undergraduate 2013 Program

Dr. Peter Garnavich

August 2, 2013

Abstract

Gamma ray bursts (GRBs) are short flashes of gamma-rays that occur in star forming regions of galaxies. In the early 2000s, a correlation between the isotropic equivalent energy radiated by the gamma ray burst and the spectral peak energy was found. This is now known as the Amati Relation. With this correlation GRBs could be used as cosmic standard candles. GRBs distances can be estimated by using the calculated isotropic energy and the observed fluence with the inverse-square law. We used the NASA Swift database to identify approximately 150 gamma ray bursts with known redshifts. From the database, we collected the duration, fluence, and the Band Function parameters such as alpha, beta, and the peak energy. We fitted a linear relation between the spectral peak energy and the isotropic energy to test the Amati Relation. We see a rough correlation with scatter and many GRBs fall far from the Amati Relation. We also applied the inverse-square law test. Our results suggest that the Amati Relation will not provide reliable distances to GRBs but other methods of estimating luminosity distance merit further research.

Introduction

In 1973, a report of a discovery of unexpected burst of gamma-rays was detected by military satellites. The best way of detecting a large number of gamma-rays was to use omnidirectional detectors. In early stage of gamma-ray bursts (GRBs) research, the GRB distribution appeared to be isotropic. This led to the theory that the sources of GRBs were galatic but in close proximity. The major properties of GRB: duration, rapid, variability, lack of periodicities, existence of two classes of GRBs. GRBs are short flashes of gamma-rays. GRBs are categorized by short and long. A short GRB is a burst that last less than 2 seconds. Short GRBs have harder spectrum and sharper high energy light curves. A long GRB last more than 2 seconds. At cosmological distances, GRBs are the most powerful explosions in the Universe. Over ten seconds they can emit energy equivalent to the energy produced by the Sun over it's lifetime. The beaming angle ranges from 1° to 10° which means that less than 1% of GRBs has jets that are aimed towards the Earth. The Burst and Transient Source Experiment (BATSE) gave great results but could not help identify the source of GRBs because of the absence of counterparts to all wavelengths. The Hubble Space Telescope showed that GRBs occur in star-forming regions of star-forming galaxies. In 1998, there was an idea that GRBs had a possible connection with a supernova. GRBs can be generated by one of the two processes the collapse of a young massive star or the merging of two neutron stars which makes a black hole and invokes the emissions of relativistic jets. GRB redshift were measured by optical spectroscopy with large ground-based telescopes. The problems with GRBs are: GRBs are not standard candles because their isotropic energy spans more than three orders of magnitude. Currently, research is being done to get better correlations to standardize GRBs energies and make them useful as "standard candles" to constrain the cosmological parameter. A lot of similar research references the Amati

Relation to understand GRBs and luminosity distance. The Amati Relation found correlation between the isotropic energy (E_{iso}) and the peak energy (E_{peak}) using 12 GRBs from the BeppoSax detector. The Amati Relation uses the Band function in order to obtain the E_{peak}. The Band function is a function of two power laws that is continuously joined. This function is used to fit GRB spectra. The Band function uses four parameters E_{peak}, alpha, beta and χ^2.

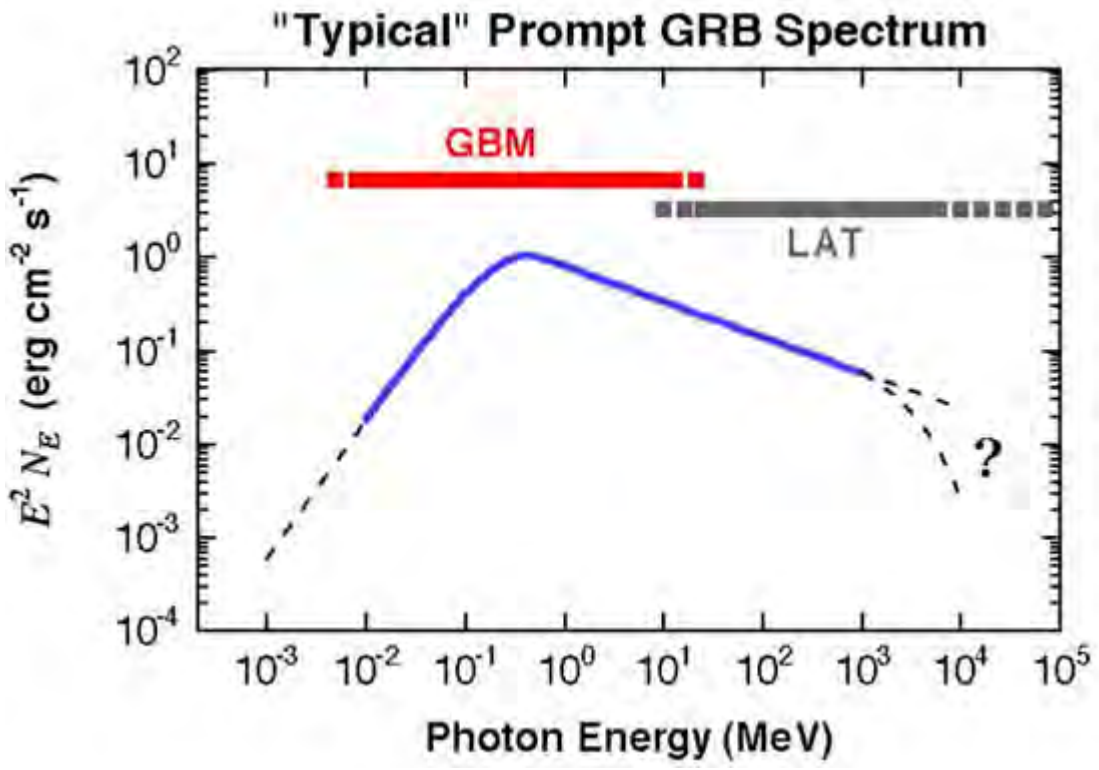

Figure 1. Band function fit of Fermi GRB. (Band, "Typical Prompt GRB Spectrum")

Methodology

We used Gamma-ray Coordinate Network (GCN) Circulars to identify 40 GRBs with known redshifts. After, we used the NASA Goddard Space Flight Center's Swift GRB Table and Lookup to identify 145 GRBs with known redshifts. Once we used collected data from Burst Alert Telescope (BAT). We collected the T90 duration, the Band Function parameters of alpha, beta, E_{peak}, and norm at 50 keV, total fluence, and redshift in a Microsoft Excel spreadsheet.

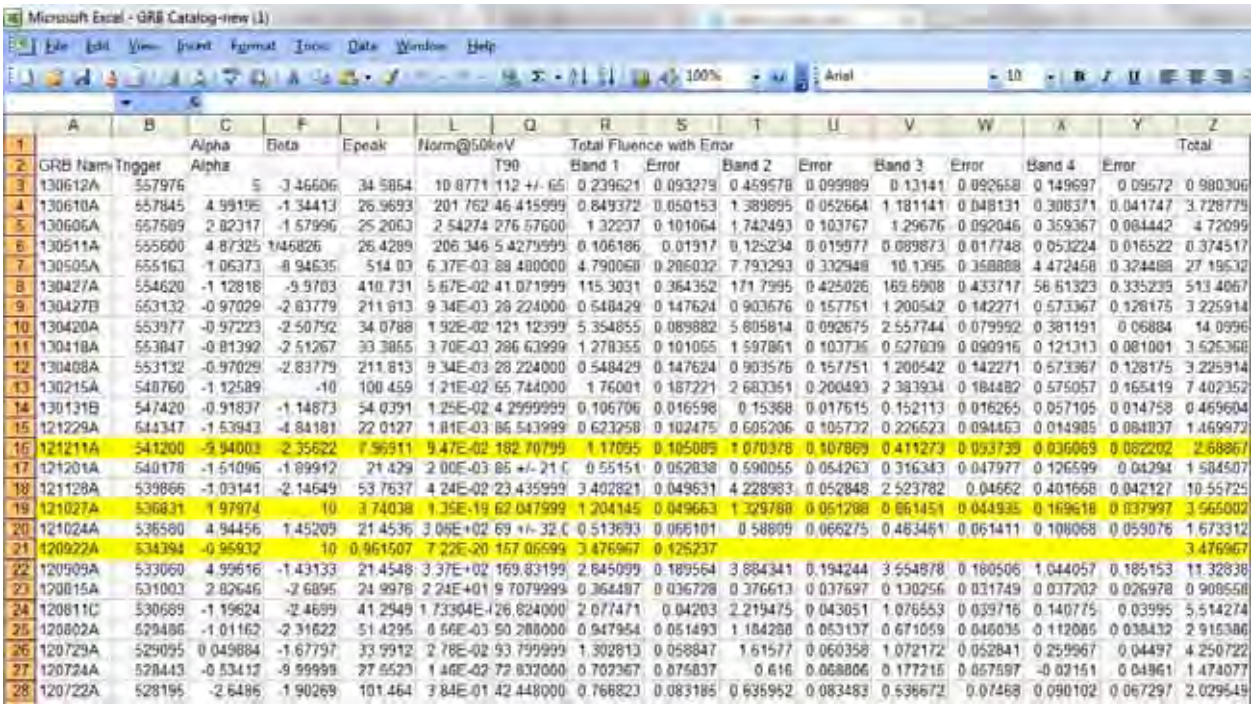

	A	B	C	F	I	L	Q	R	S	T	U	V	W	X	Y	Z
1			Alpha	Beta	Epeak	Norm@50keV		Total Fluence with Error								Total
2	GRB Nam	Trigger	Alpha				T90	Band 1	Error	Band 2	Error	Band 3	Error	Band 4	Error	
3	130612A	557976	5	-3.46606	34.5854	10.8771	112 +/- 65	0.239621	0.093279	0.459578	0.099989	0.13141	0.092658	0.149697	0.09572	0.980306
4	130610A	557845	4.99196	-1.34413	26.9693	201.762	46.415999	0.849372	0.050153	1.389895	0.052664	1.181141	0.048131	0.308371	0.041747	3.728779
5	130606A	557589	2.82317	-1.57996	25.2063	2.54274	276.57600	1.32237	0.101064	1.742493	0.103767	1.29676	0.092046	0.359367	0.084442	4.72099
6	130511A	555600	4.87325	1/46826	26.4289	206.346	5.4279999	0.106186	0.01917	0.125234	0.019977	0.089873	0.017748	0.053224	0.016522	0.374517
7	130505A	555163	1.06373	-8.94635	514.03	6.37E-03	88.480000	4.790068	0.286032	7.793293	0.332948	10.1395	0.358888	4.472458	0.324488	27.19532
8	130427A	554620	-1.12818	-9.9703	410.731	5.67E-02	41.071999	115.3031	0.364352	171.7995	0.425026	169.6908	0.433717	56.61323	0.335235	513.4067
9	130427B	553132	-0.97029	-2.83779	211.813	9.34E-03	28.224000	0.548429	0.147624	0.903676	0.157751	1.200542	0.142271	0.573367	0.128175	3.225914
10	130420A	553977	-0.97223	-2.50792	34.0788	1.92E-02	121.12399	5.354855	0.089882	5.805814	0.092675	2.557744	0.079992	0.381191	0.06884	14.0996
11	130418A	553847	-0.81392	-2.51267	33.3855	3.70E-03	286.63999	1.278355	0.101055	1.597861	0.103735	0.527609	0.090916	0.121313	0.081001	3.525368
12	130408A	553132	-0.97029	-2.83779	211.813	9.34E-03	28.224000	0.548429	0.147624	0.903676	0.157751	1.200542	0.142271	0.573367	0.128175	3.225914
13	130215A	548760	-1.12589	-10	100.459	1.21E-02	65.744000	1.76001	0.187221	2.683351	0.200493	2.383934	0.184482	0.575057	0.165419	7.402352
14	130131B	547420	-0.91837	-1.14873	54.0391	1.25E-02	4.2999999	0.106706	0.016598	0.15368	0.017615	0.152113	0.016265	0.057105	0.014758	0.469604
15	121229A	544347	-1.53943	-4.84181	22.0127	1.81E-03	86.543999	0.623258	0.102475	0.695206	0.105732	0.226523	0.094463	0.014985	0.084837	1.469972
16	121211A	541200	-5.94003	-2.35622	7.96911	9.47E-02	182.70799	1.17095	0.105089	1.070378	0.107869	0.411273	0.093739	0.036069	0.082202	2.68867
17	121201A	540178	-1.51096	-1.89912	21.429	2.00E-03	85 +/- 21.0	0.55151	0.052838	0.590055	0.054263	0.316343	0.047977	0.126599	0.04294	1.584507
18	121128A	539866	-1.03141	-2.14649	53.7637	4.24E-02	23.435999	3.402821	0.049631	4.228983	0.052848	2.523782	0.04662	0.401668	0.042127	10.55725
19	121027A	536831	1.97974	-10	3.74038	1.35E-19	62.047999	1.204145	0.049663	1.329788	0.051288	0.861451	0.044935	0.169618	0.037997	3.565002
20	121024A	536580	4.94456	1.45209	21.4536	3.06E+02	69 +/- 32.0	0.513693	0.066101	0.58809	0.068275	0.463461	0.061411	0.108068	0.059076	1.673312
21	120922A	534394	-0.95932	-10	0.961507	7.22E-20	157.06599	3.476967	0.125237							3.476967
22	120909A	533060	4.99616	-1.43133	21.4548	3.37E+02	169.83199	2.645099	0.189564	3.884341	0.194244	3.554878	0.180506	1.044057	0.185153	11.32838
23	120815A	531003	2.82646	-2.6895	24.9978	2.24E+01	9.7079999	0.364497	0.036728	0.376613	0.037697	0.130256	0.031749	0.037202	0.026978	0.909558
24	120811C	530689	-1.19624	-2.4699	41.2949	1.73304E-4	26.624000	2.077471	0.04203	2.219475	0.043051	1.076553	0.039716	0.140775	0.03995	5.514274
25	120802A	529486	-1.01162	-2.31622	51.4295	6.56E-03	50.288000	0.947954	0.051493	1.184288	0.053137	0.671059	0.046035	0.112085	0.038432	2.915386
26	120729A	529095	0.049884	-1.67797	33.9912	2.78E-02	93.799999	1.302813	0.058847	1.61577	0.060358	1.072172	0.052841	0.259967	0.04497	4.250722
27	120724A	528443	-0.53412	-9.99999	27.5523	1.46E-02	72.832000	0.702367	0.075837	0.616	0.068806	0.177215	0.057597	-0.02151	0.04961	1.474077
28	120722A	528195	-2.6486	-1.90269	101.464	3.84E-01	42.448000	0.766823	0.083185	0.635952	0.083483	0.536672	0.07468	0.090102	0.067297	2.029549

Figure 2. Screenshot of Microsoft Excel Spreadsheet

T90 duration is defined as the time interval where 90% of the total background subtracted counts are observed. The Alpha and beta parameters are low energy index and high energy index respectively. Fluence is the flux of a GRB integrated over time. Redshift is the displacement of spectral lines toward longer wavelength in radiation from distant galaxies and celestial objects. Once we collected all the data from Swift BAT we used a program to calculate the luminosity distance from the redshift. With the luminosity distance calculated and converted to centimeters, we used $L(z)=(P(z)\ 4\ \pi\ d^2)/(1+z)$ (Meszaros et al., 2012). Where L(z) is the isotropic energy, P(z) is the total fluence, d is the luminosity distance, and z is the redshift. The energy of radiation is inversely related to its wavelength $E= hc / \lambda$ where h is Planck's constant. Since the Band function peak energy is the observed energy E_{obs} then the wavelength λ_{obs}. Due to the expansion of the universe the wavelength is stretched by (1+z). So the wavelength is emitted at a shorter wavelength $\lambda_{emit} = \lambda_{obs} / (1+z)$. Meaning the energy emitted is $E_{emit} = hc/ \lambda_{emit}$ and with

substitution of λ_{emit} you get $E_{emit} = E_{obs} * (1+z)$, this is the corrected E_{peak} (E_{peak}') and L(z) a plot was made to understand the correlation. A best fit line was calculated to understand the correlation between L(z) and E_{peak}'. The equation to best describe the data is $L(z) = 2.75106\times10^{50}$erg $keV^{-.768687}$ $E_{peak}'^{.768687}$ (Figure 3). While the Amati Relation equation is $E_{iso}= 9.2 *10^{47}$ erg $keV^{2.04}$ $[E_{peak} (1+z)]^{2.04}$. (Collazzi et al., 2012)

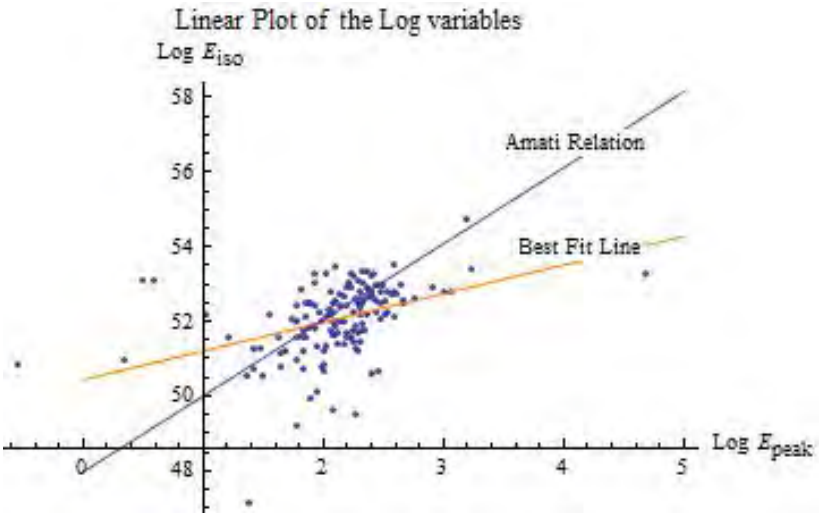

Figure 3. Linear Plot of Log variable with Amati Relation and best fit line

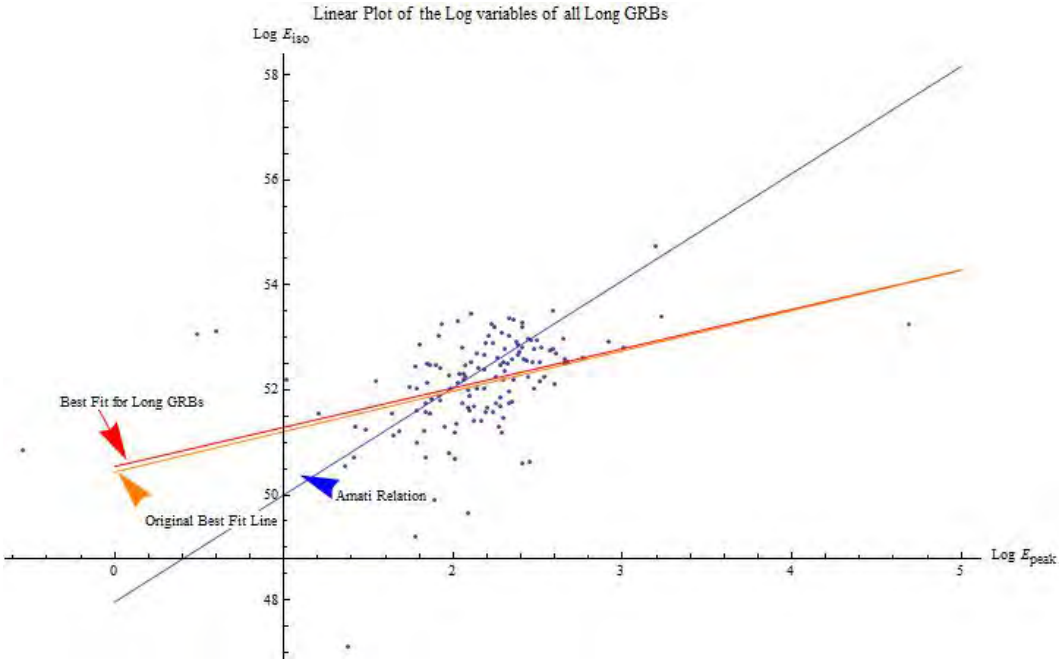

Figure 4. Plot of on Long GRBs

To Table of Contents

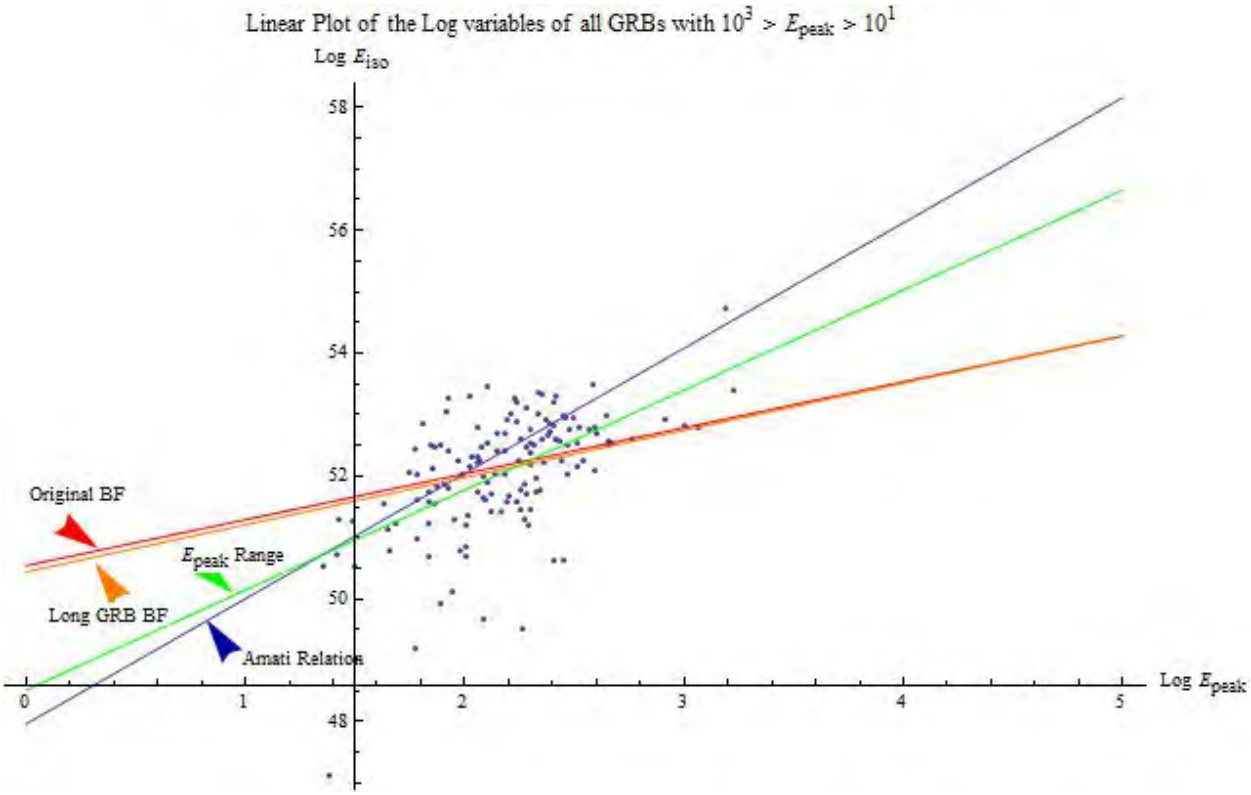

Figure 5. Plot of GRBs with E_{peak} in the range of 10^1 to 10^3 keV

The figure 3 shows that the best fit line is not close to the Amati Relation. Short GRB were removed from the data and plotted against the original best fit line and the Amati Relation. Figure 4 shows that the best fit line of only long GRBs did not change much from the original data. The best fit line for only long GRBs is $E_{iso} = 3.48676\times10^{50}$ erg $keV^{0.748137} * E'_{peak}{}^{0.748137}$. GRBs with 10^3 keV < E_{peak} < 10^1 keV was removed and plotted against the original best fit line, Amati Relation and long GRB fit line. Figure 5 shows the best fit of GRBs with 10^1 keV < E_{peak}< 10^3 keV. The best fit line for the range of E_{peak} is $E_{iso}= 3.2961*10^{48}$ erg $keV^{1.62799}$ $E'_{peak}{}^{1.62799}$. Though the green best fit line is close to the Amati Relation it is not close enough. The Amati Relation does not work for our data because selection effect. (Collazzi et al, 2012). There are

more faint and low energy GRBs than high energy GRBs. The Swift detector can not detectable faint GRBs therefore an absence of more common GRBs.

Conclusion

GRBs are the most powerful explosions in the universe. GRBs can be use to estimate luminosity distances. After identifying 145 GRBs with known redshifts, we plotted the E_{peak} against E_{iso} and found the best fit line of our Swift data. We also removed the short GRBs and found that the best fit line to describe the long GRBs related closely with the original data. We plotted all the GRBs that have E_{peak} in the range of 10^1 and 10^3 keV. The best fit changed significantly but not enough to prove the Amati Relation to be correct. We have found that the Amati Relation is not useful for cosmological measurements because of it heavily rely on the selection effects. We believe that there are better relations for cosmological measurements. We would like to test other relations such as the Ghirlanda Relation.

References

Amati, L. et al. (2012) Intrinsic spectra and energetics of bepposax gamma-ray bursts with known redshifts.*Astronomy and Astrophysics, 390*, 81-89. doi: 10.1051/0004-6361:20020722

Band, B. (Photographer). (2008, October 28). Typical Prompt GRB Spectrum [Web Graphic]. Retrieved from http://polywww.in2p3.fr/activites/physique/glast/workbook/pages/sciAnalysis_pages/iLat/iLat_grbSpectralAnalysis.htm

Collazzi, A. et al (2012). A signifcant problem with using the amati relation for cosmological purposes. *The Astrophysical Journal, 747*(1), 39-53. doi: 10.1088/0004-637X/747/1/39

Meszaros, A. et al. (2012). Cosmological effects on the observed flux and fluence distributions of gamma-ray bursts: Are the most distant bursts in general the faintest ones?. *International Astronomical Union Symposium, 279*, 385-386. doi: 10.1017/S1743921312013464

Vedrenne, G., & Atteia, J. (2009). *Gamma ray bursts: The brightest explosions in the universe*. Chichester, UK: Praxis Publishing Ltd.

To Table of Contents

Detangling the Cosmic Web

Computational Models of Galaxies in Filaments

Sarah Dietz

2013 REU Program

Physics Department, University of Notre Dame

Advisor: Professor Arielle Phillips

Abstract

Sheets, filaments, and voids are Large Scale Structures (LSS) that describe patterns of galaxy organization in what is known as the Cosmic Web. Filaments contain galaxies, gas and dark matter, and it is of interest to study how galaxies interact with the filaments they are embedded in. We modify an existing fluid dynamics program to create a two-dimensional computational model of a galaxy in a filament. We studied both galaxies with spins parallel to the flow of their host filaments and galaxies with spins perpendicular to their filaments, in order to observe how the exchange of material between galaxy and filament differed for each case. The program solves the incompressible Navier-Stokes Equation allowing us to model the exchange of energy between galaxies and filaments. However it does not allow for variable density and the modeling matter exchange between galaxies and filaments. We therefore turn to programs that provided solutions to the compressible Navier-Stokes Equation to study the models.

Introduction

This paper details the construction of a computational simulation of a galaxy moving through a filament. A filament is an astronomical object that contains gas, galaxies, and dark matter, and describes a pattern of galaxy organization. Filaments, sheets, and voids are all Large Scale Structures (LSS) that are part of what is known as the Cosmic Web, a term describing the way in which galaxies and other LSS materials are distributed throughout the universe.[1][2] Through mechanisms like supernovae, galaxies can eject material into their host filaments, and the gravitational force a galaxy exerts on the filamentary material it travels through it allows it to accrete matter from its surroundings as well. Currently, many large-scale astronomical

[1] (Colberg 337-347)
[2] (Tempel, Stoica, and Saar)

simulations approximate galaxy outflow to be evenly distributed over a galaxy's surface, but our model simulates a galaxy with localized outflow and inflow points. We focused on the case of a disc galaxy (with a very simplified shape) and observed how the gas flow around a galaxy changed for the case of a galaxy with a spin perpendicular to its host filament and a galaxy with a spin parallel to its filament. We chose these cases in hopes of determining what effect galaxy orientation has on the distribution of feedback materials.

Method

The base code for this program was taken from a Java listing from "A Survey of Computational Physics" modeling the two-dimensional flow of water over a beam. A galaxy moving through filamentary gas can roughly be modeled as a stationary obstruction sitting in a stream of liquid, so this program is an appropriate starting point. It also has certain limitations, which we will discuss later.

In the program, a beam of specified dimensions is placed on a two-dimensional grid. The stream function and vorticity field are initialized, and initial conditions are set around the inlet, outlet, surface, and centerline[3] of the grid, as well as around the sides of the beam.

The stream function relates to the velocity as follows:

$$\vec{v} = \vec{\nabla} \times \vec{u}(\vec{x})$$

For the two-dimensional case we are studying:

$$v_x = \frac{\partial u}{\partial y}$$

[3] This simulation models the "top" half of a galaxy with symmetric features, so the bottom of the grid represents the line of symmetry, not the boundary of the filament.

$$v_y = -\frac{\partial u}{\partial x}$$

The vorticity measures how much the fluid rotates[4]:

$$\vec{w} = \vec{\nabla} \times \vec{v}(\vec{x})$$

This program is designed to solve for the stream function at each point on the grid through successive overrelaxation. However, it is sometimes easier to gauge from the velocity graphs whether our data matches our theoretical model than it is to reference the stream function plots for the same purpose. We can go backwards a bit and have the same program solve for velocity as well.

Given the value of the stream function at all points on the grid, the velocity at a point (i, j) can be calculated using the central difference approximation:

$$v_x = \frac{u(i, j+1) - u(i, j-1)}{2h}$$

$$v_y = -\left(\frac{u(i+1, j) - u(i-1, j)}{2h}\right)$$

Because we have solved this problem somewhat backwards—solving for the stream function first, then the velocity—we can alter v_x and v_y by changing the value of the stream function around points at which we wish to simulate the outflow or inflow of gas.

For both galaxy configurations, inflow is parallel to the plane of the galaxy (located along the rim of the galaxy disc), and outflow is perpendicular to the plane of the galaxy.

[4] A Survey of Computational Physics

For perpendicular galaxies, inflow conditions mandate that gas moving towards the side of the rim facing the grid inlet will move towards the rim at a faster rate due to the gravitational force the galaxy exerts on this gas. Gas moving past the opposite rim will slow down (in the x-direction) because it is being pulled back towards the galaxy by the same force. Outflow conditions mandate that gas around outflow points will experience increased velocities in the y-direction.

For parallel galaxies, inflow conditions mandate that gas located around the galaxy's rim will experience decreased velocities in the y-direction due to the galaxy's gravitational force. Outflow conditions mandate that gas located around outflow points on the side of the galaxy facing towards the grid inlet will experience decreased velocities in the x-direction because the gas flowing from the inlet is retarded by outflowing gas from the galaxy moving in the opposite direction. Gas located around outflow points on the side of the galaxy facing away from the grid inlet will experience increased velocities in the x-direction because the outflow gas on this side of the galaxy flows towards the positive x-direction.

For both models, inflow conditions were placed at several points extending outwards from the rim of the galaxy, with points closer to the galaxy having stronger inflows, to simulate the gravitational force extending outwards from the galaxy, growing weaker as the distance from the center of the galaxy increases.

Results

Included below are several graphs representing the outflow and inflow conditions listed above for both galaxy models. The displayed magnitudes for inflow and outflow velocities were

selected to maximize visibility, they are not representative of actual galaxy properties.

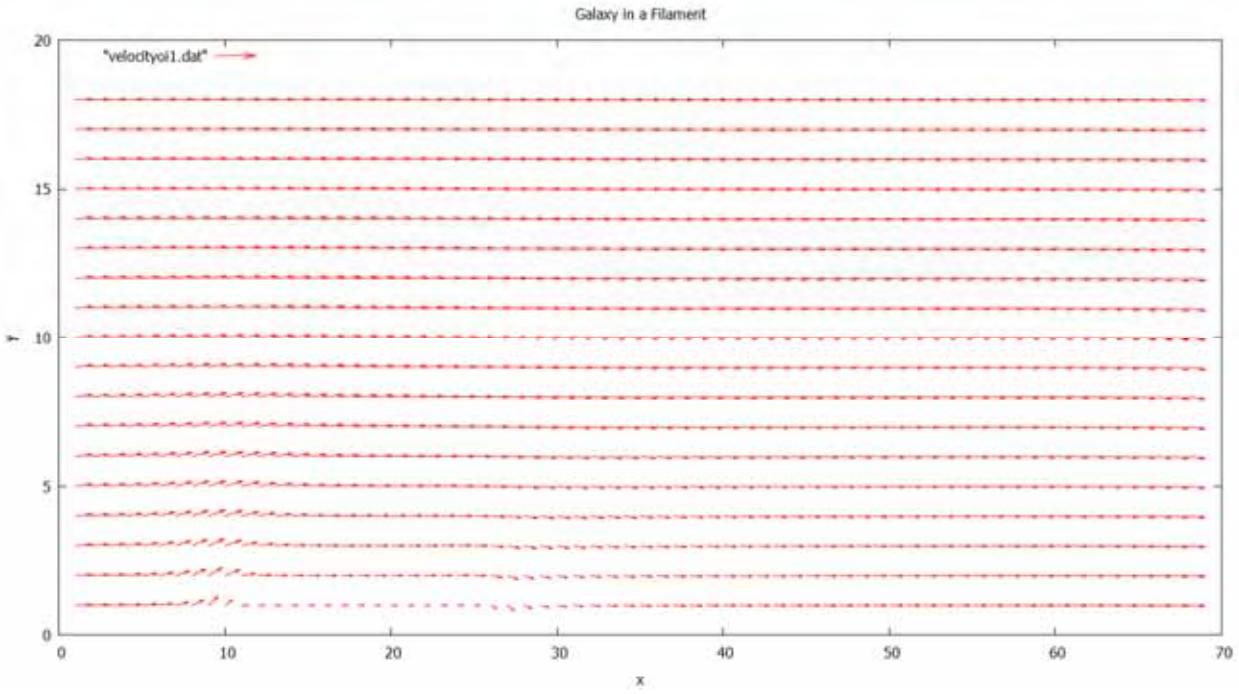

Figure 1: Perpendicular galaxy without outflow/inflow, velocity vector field

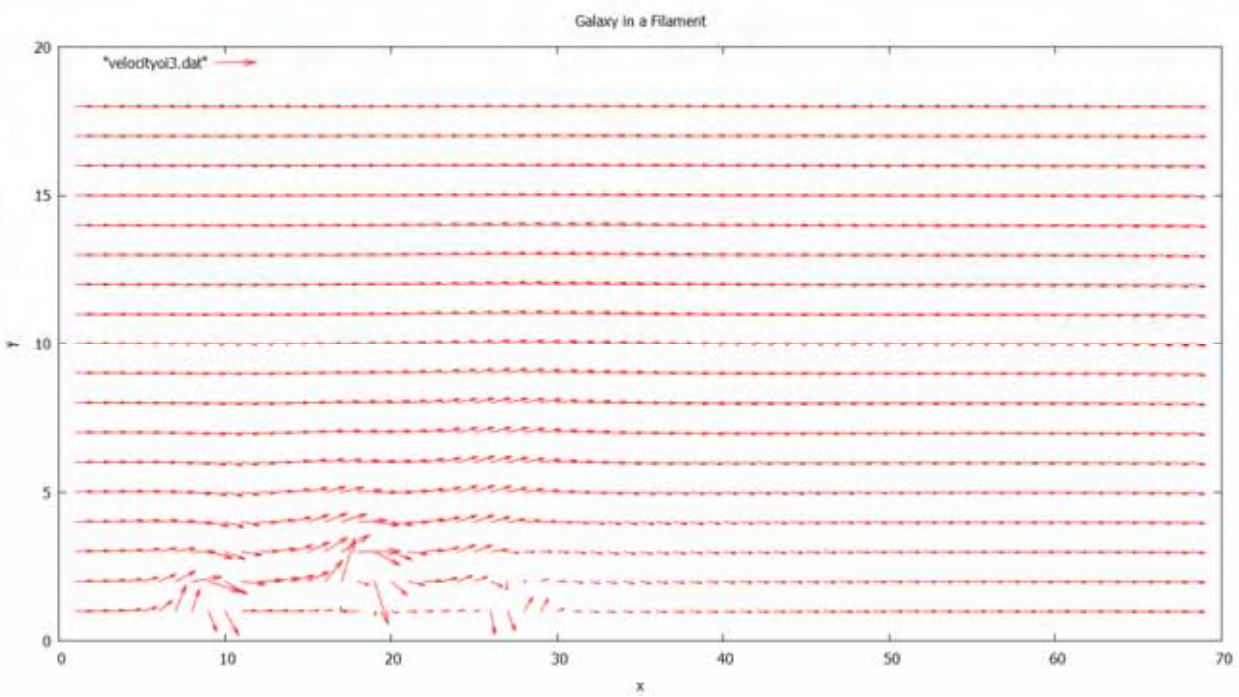

Figure 2: Perpendicular galaxy with outflow and inflow, velocity vector field

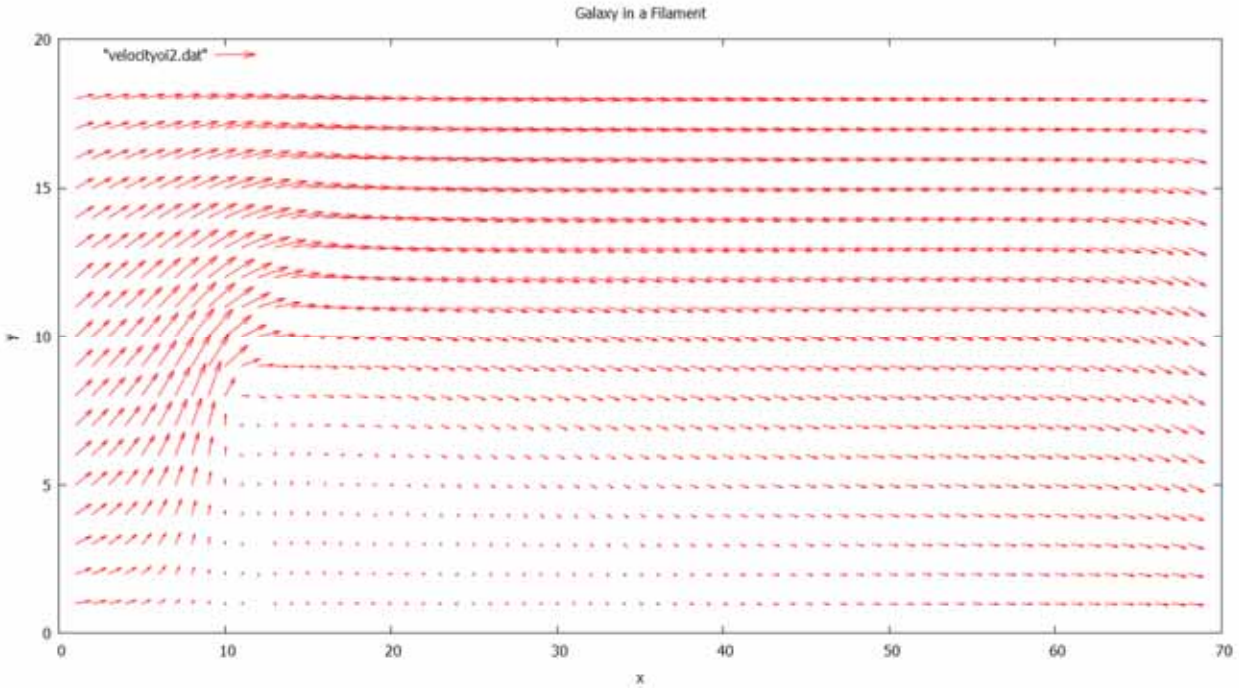

Figure 3: Parallel galaxy without outflow/inflow, velocity vector field

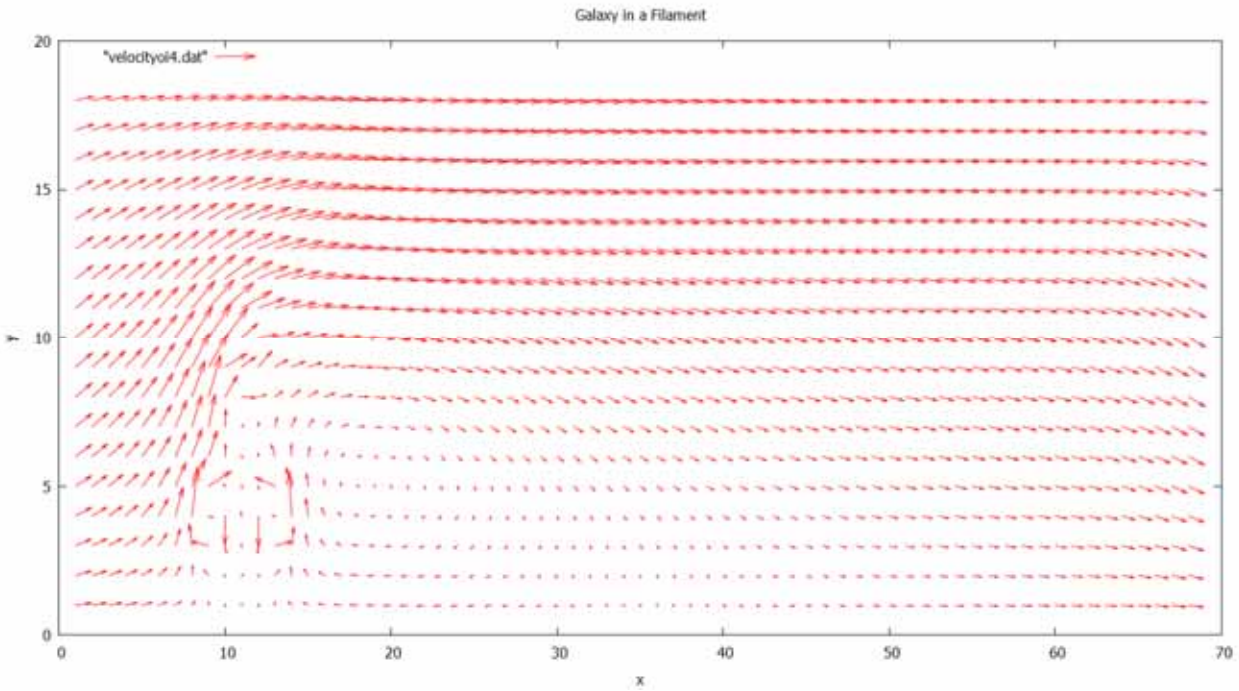

Figure 4: Parallel galaxy with outflow and inflow, velocity vector field

The perturbations in the gas observed for the parallel case are significantly larger than for the perpendicular case, but this appears to be mainly due to galaxy orientation rather than inflow and outflow conditions. The effect of the inflow and outflow conditions on the surrounding gas seem to depend largely on the strength of said conditions, so, until realistic galaxy inflow and outflow rates are applied to this simulation, we cannot determine how the effect of the inflow and outflow of these two models on filamentary gas differs.

Conclusion

Although this simulation has allowed us to model the perturbations in the velocity of filamentary gas caused by galaxy outflow and inflow, it is not an adequate tool for modeling the exchange of mass between galaxy and filament. To do this we need to create a new model utilizing the compressible Navier-Stokes equation, which allows for non-constant density.

Solving this equation is a daunting project in and of itself, but computational tools exist to aid us in this endeavor. Unfortunately, modeling this equation is outside the scope of this project. Critiques of preexisting compressible Navier-Stokes equation solvers and suggestions for how to use these tools can be found in Appendix A.

After considering density-flow models, the next step in refining this simulation would be to apply theoretical values for the velocities, viscosities, densities, etc. for the types of galaxies and filaments we are studying to the simulation. Known inflow and outflow patterns could be applied to our model to make it a more accurate reflection of a real galaxy, and increasing the number of iterations the program runs through could demonstrate how the flow around a galaxy might look over many years.

Bibliography

Colberg, Jorg M. "Quantifying Cosmic Superstructures." *Monthly Notices of the Royal Astronomical Society*. 375 (2007): 337-347 . Web. 2 Aug. 2013.

Landau, Rubin H., Manuel José Páez, and Cristian C. Bordeianu. *A Survey of Computational Physics: Introductory Computational Science*. Princeton University Press, 2008. Print.

Tempel, E., R. S. Stoica, and E. Saar. "Evidence for spin alignment of spiral and elliptical galaxies in filaments." *MNRAS*. (2012): n. page. Web. 2 Aug. 2013.

Appendix A

Nektar++ is a multifaceted “solver” program that includes a Compressible Flow Solver for two-dimensional fluid dynamics problems. Some assembly is required, knowledge of C++ would be helpful. It may be more difficult to run the program with Windows than with a Mac or Linux computer.

www.nektar.info

This Interactive Computational Fluid Dynamics Solver was created at the University of Central Arkansas and includes both compressible and incompressible CFD solvers. We have not been able to get the program to run successfully, so it is possible that the program is out-of-date or contains some errors. The email address of one of the program’s creators is included in the webpage listed below, so it may be possible to contact him and discuss program difficulties directly.

http://faculty.uca.edu/clarenceb/ComputationalScience/Interactive_CFD_UCA.html

New Targets for New Accelerators

Bryce Frentz

2013 NSF/REU Program

Physics Department, University of Notre Dame

Nuclear Science Laboratory

Advisors:

Ani Aprahamian

Khachatur Manukyan

Abstract

New accelerators, such as the 5MV Sta Ana accelerator, at the University of Notre Dame, will produce more powerful beams up to 100's of μAmps. These accelerators require a complete rethinking of target preparation since the high intensity of such beams would melt conventional targets. Traditionally, accelerator targets are made with a tantalum backing. Tantalum, while being a successful material to stop hadron beams, is also brittle, a poor conductor, and, if produced commercially, often contains impurities (e.g. fluorine) that produce undesirable background signals and reaction products. Despite tungsten's brittle structure and poor conductivity, its high proton number, allowing it to stop hadron beams, and lack of impurities make tungsten a more desirable backing than tantalum. In conjunction with tungsten's properties, copper is robust and a far superior conductor of heat. We describe a new method of reactive joining, which we developed for creating targets by using the advantageous properties of both tungsten and copper. This process involved placing a reactive mixture (Fe_2O_3+Mg, Ti+C+Ni, or Ti+C+Si) between tungsten and copper and applying a load force. The mixture is then ignited, and while under pressure, the system produces conditions to join the materials. We present our investigation to optimize the process of reactive joining, as well as some of the final target's properties.

1 Introduction

A new generation of accelerators, such as the St. ANA accelerator at the University of Notre Dame and the accelerator in the proposed Dakota Ion Accelerators for Nuclear Astrophysics (DIANA) project at the Sanford Underground Research Facility (SURF), will produce higher intensity beams than ever previously attained. Beam intensities are estimated to be on the order of hundreds of μAmps and tens of mAmps, respectively. These new intensity thresholds introduce significantly higher temperatures at points where the ion beam interacts with the beamline, either at the experimental target or the beam slits. These temperatures would be to the point that they would destroy the current generation of solid targets and slits in the beamline, both made from tantalum [1]. Tantalum is traditionally used for targets and slits in the beamline because it has a high proton number, making it effective for stopping ion beams. However, it is quite brittle, a poor conductor of heat, and often contains impurities (e.g. fluorine) when produced commercially. All of these negative characteristics pose serious problems when considering tantalum's use in new accelerators. Tungsten, like tantalum, is both brittle and a poor conductor of heat but rarely contains impurities, making it a desirable candidate to replace tantalum in beam and target applications. Copper is well known as a robust material that is also a superior conductor of heat.

By joining tungsten to copper, one can take advantage of copper's characteristics, compensating for tungsten's deficiencies, making this joined product desirable for accelerator applications.

The joining of dissimilar materials, such as copper and tungsten, continues to garner high attention and focus in materials science due to the abundance of possible applications of joined materials in military, industrial, and academic fields. For clarification, we define dissimilar materials to be those with significant differences in their structures and physical properties, such as lattice structure, thermal conductivity, or shear strength. One system of dissimilar materials which no one has yet been able to join copper and tungsten. The difficulties with these materials arise namely due to the disparity in melting temperatures, with copper melting at ∼1350 K and tungsten melting at ∼3700 K, because few reactive mixtures generate the heat necessary to melt and bond them. Additionally, copper's surface is not conducive to joining because of its tightly-bound crystal structure. To overcome this, intermediary layers must be incorporated in the design to ensure a quality bond with copper. Despite these difficulties, many methods exist for joining dissimilar materials, such as spark plasma sintering, hot pressing, and combustion joining. Mukasyan and White [2] detail the primary combustion methods, including our method. We chose combustion joining because it relies on localized heating, making this method cost-effective and compact. In this paper, I describe a system developed to join copper and tungsten, thus introducing a new generation of solid targets, accompanying the new generation of accelerators constructed for nuclear experiments.

2 Experimental Method

2.1 Thermodynamic Calculations

The thermodynamic calculations for the combustion reaction of each compound (Fe_2O_3+Mg, Ti+C+Ni, and Ti+C+Si) are performed using the THERMO software [3]. These calculations receive the initial mixture composition, pressure, and temperature then output the adiabatic temperature of the reaction as well as the final equilibrium products for the given scenario. Following these calculations, the feasible thermodynamic systems are selected for further experimental study.

2.2 Sample Preparation and Joining Experiments

The joining experiments were performed under optimal conditions, determined through a series of experiments identifying ideal parameters. Typically, the sample preparation consisted of hand-mixing the reagent compounds (Alfa Aesar, -325 mesh) for twenty minutes with no extra atmospheric requirements. Once mixed, the amalgamated powder of choice was pressed into two 1.0 g pellets in a 20 mm cylindrical die. Following the pressing of the reagent pellets and cleaning the copper in an acid bath, the materials were assembled, as shown in Fig. 1, using one piece of tungsten foil (Alfa Aesar), one piece of 100 μm Ni foil (Alfa Aesar), one piece of 25 μm, Ni foil (Alfa Aesar), and two pieces of 40 μm Ni+Al nanofoil (Indium Corporation, 20 nm layers of Ni and Al), sandwiched between two plungers. Typical experiments placed these sample under a load force between 4000 and 5000 lbs for 90 s, while the reaction was triggered by igniting the Ni+Al nanofoil with a tungsten coil connected to variable voltage source.

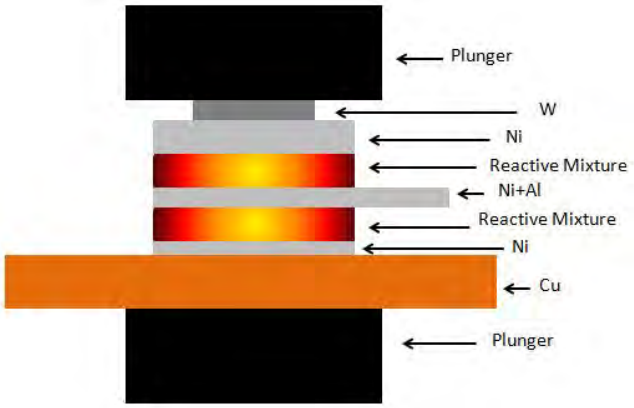

Figure 1: The optimal configuration of materials.

2.3 Characterization of Samples

The phase compositions of combustion reaction products were determined by X-ray diffraction (XRD) analysis with Ni-filtered Cu K_α radiation (Scintag, X1 Advanced Diffraction System), operated at 40 kV and 40 mA. Step-scan with size of 0.02° and counting time up to 1 s were recorded for the angular range $10° - 80°$ (2θ).

Thermal analysis of the reaction and the reacted sample were also used to characterize the final result. A high-speed infrared (IR) camera (FLIR Systems, SC6000) was used to monitor combustion wave characteristics. It provided two dimensional maps for the temperature-time history of the process inside the reaction. The thermal videos were captured over several different temperature ranges which included temperatures as high as 2000°C and frame rates upwards of

1000 frame per second with spatial resolution of $\sim 5\mu$m. Additionally, certain join products were chosen to analyze their ability to withstand high temperatures. These samples were placed in a quartz tube, purged with an argon atmosphere to prevent oxidation, and subsequently heated to 650°C over two hours, then held constant at that temperature for two hours, before being cooled over another two hours. While this test was designed to investigate the ways in which the samples responded to prolonged heating, simulating accelerator conditions, it is important to stress that materials will never reach such high temperatures because they will be water cooled in the accelerator.

Scanning electron microscopy (SEM) was employed to characterize the composition and structure of the post-reaction samples. The SEM analysis was conducted using a Magellan 400 microscope (FEI, USA), equipped with an energy dispersive X-ray spectrometer (EDS) (Oxford Instruments, INCA). Before the microscopy, the samples were mounted in epoxy resin, cut in half using a diamond coated saw to prevent damage to the sample, and then polished using fine grain sandpaper to prepare a cross-section of the sample. These images were used to analyze the quality of the join, judged primarily on the porosity (a trait that can roughly correlates to strength of join) and the extent to which the layers melted together. Additionally, this analysis was used to examine the ways in which heating affected the microstucture of the samples to ascertain if heating will pose future problems implementing the materials.

3 Results and Discussion

During this experiment, three different thermodynamic systems were chosen to study: Fe_2O_3+Mg (commonly known as thermite), Ti+C, and Ti+Si. These compounds were selected for their reactive properties and historical use in combustion joining. Preliminary calculations showed that all reactions generated the necessary heat to join the materials; however, it became apparent that both the thermite and Ti+C systems introduced defects to the reacted layer that either did not create a stable join or left a low quality join layer. In regards to the thermite system, a large problem arose because one of the final equilibrium products was an oxide, specifically MgO. Oxides are poor thermal conductors and brittle, implying that this final reaction product would not work well

for the intended application. The other major issue was shared between the thermite and Ti+C reactions. Both were very violent as gas phases developed in the reaction causing material to be ejected, ultimately leaving the sample unable to generate the necessary heat to join the materials. The Ti+Si system presented neither of these difficulties and was therefore provided more desirable join layer. Thus, the following analysis focuses on the Ti+Si system and its results. Within the system, we introduced Ni to moderate the reaction temperature (to prevent damage to tungsten) and strengthen the final reaction products.

3.1 Thermodynamics

It is important to note that the calculations performed give the adiabatic temperature (T_{ad}) of the reaction, which is the maximum temperature the reaction is predicted to achieve with no heat loss outside the system. The results of these calculations are presented in Fig. 2. Fig. 2(a) demonstrates that the highest temperature reactions and the accompanying reaction products, those useful for joining copper and tungsten, are found to have Ni content $< 30\%$ and produce Ti_5Si_3 as equilibrium products. Ti_5Si_3 is also a desirable reaction product because of its high refractory melting temperature, making it better suited for accelerator applications. Fig. 2(b) indicates optimal initial ratios to produce Ti_5Si_3 in the reaction.

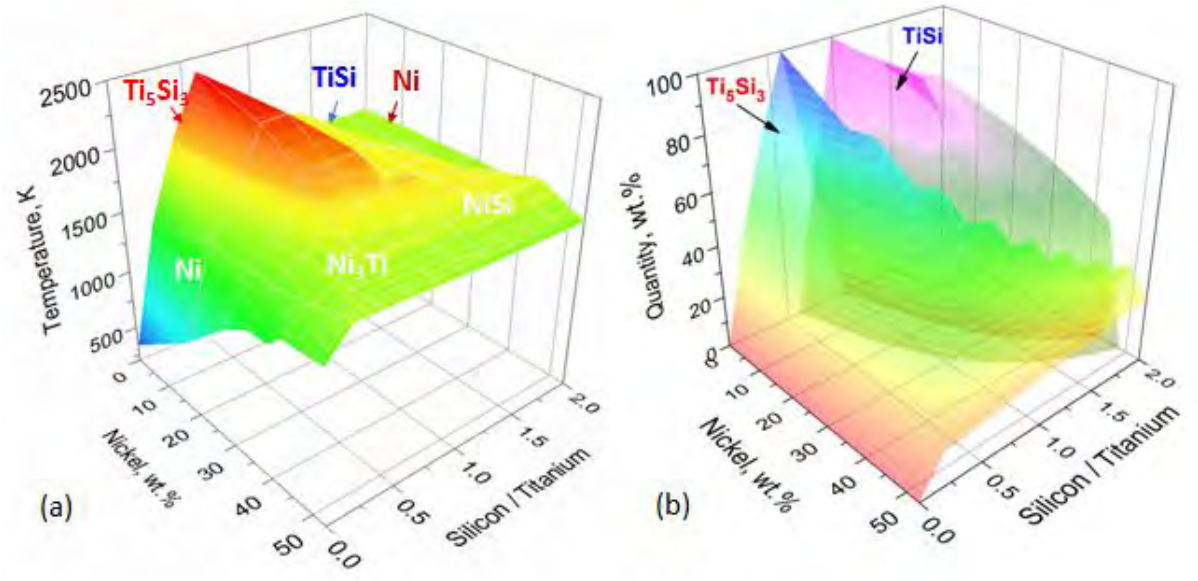

Figure 2: T_{ad} (a) and equilibrium product percentage (b) as functions of both Ni percentage and Si/Ti ratio.

To Table of Contents

3.2 Measurement of Reaction Temperature

The temperature-time profiles, as measured by the IR camera, are presented below in Fig. 3. This is significant because they show the actual reaction temperature for the varying compositions. As expected, the addition of Ni to the mixture lowers the reaction temperature because this takes heat away from the Ti+Si reaction. This is shown in the Fig. 3(a), as the 0% Ni sample has a higher reaction temperature than Fig. 3(b)-(d), those with Ni. However it is also important to note that the addition of Ni introduces a secondary oxidation reaction in the samples that provides prolonged heat, an effect minimized in our reactions because the reactive layer has minimal exposure to air. Thus, the initial reaction peak is the most representative of our samples.

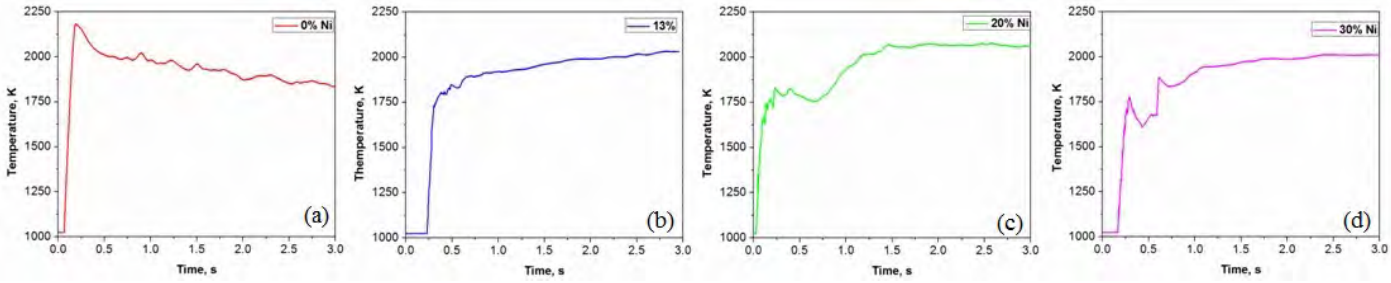

Figure 3: The temperature-time profiles for compositions with varying Ni content: 0% (a), 13% (b), 20% (c), and 30% (d).

3.3 XRD

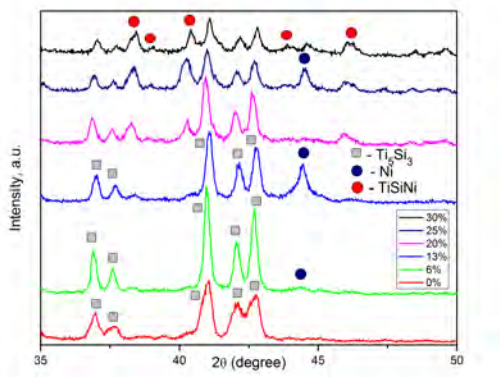

Figure 4: Results of XRD analysis of combustion product mixtures with varying Ni content.

To analyze the phase composition of the reacted samples, XRD analysis was performed on the join layers. After the reaction, material was collected and ground into powder for examination. These data are presented in Fig. 4. Examining these data, there is a clear absence of pure Ti and Si, indicating that conversion degree of reactants is ~100%. It is important to note that as Ni content reaches 20% there is the introduction of the TiSiNi phase which was not predicted in the calculations because the software does not contain the compound's data.

3.4 SEM Analysis

Typical SEM images of the samples with varying Ni contents are shown in Figs. 5-9. The first image presents a low magnification image to highlight the major differences between the samples of varying Ni content, an optimization condition. From this image it is clear that at higher Ni percentages the samples become less porous, indicating a stronger join between the materials. In terms of porosity, the 20% Ni sample was the least porous, indicating that this layer is the highest quality join. Additionally, cracks in the join layer are present for both the 0% Ni and 30% Ni samples, indicating that the optimal Ni content lies in this range.

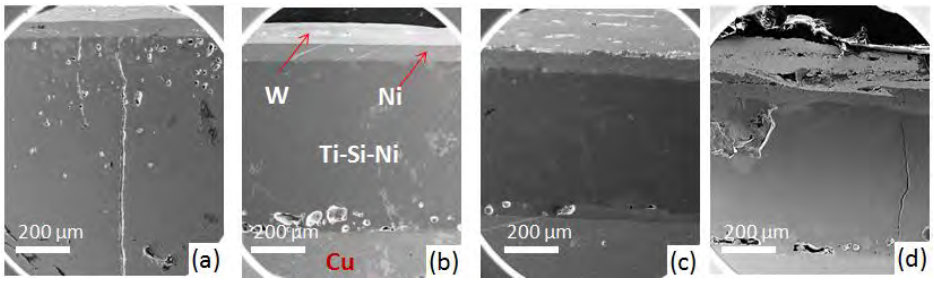

Figure 5: Low magnification images of join layer cross section for Ni content 0% (a), 13% (b), 20% (c), and 30% (d). These samples were joined with 50 μm tungsten under 4000 lbs of pressure.

The next image, Fig. 6, shows a close image of the tungsten layer for the samples, again with varying Ni content. This image indicates that there are only subtle differences between the tungsten side joins and that all are quality. However, upon examination, the tungsten is uneven in both the 0% and 20% samples, indicating that the in the reaction a low melting point Ni-W intermetallic phase is forming.

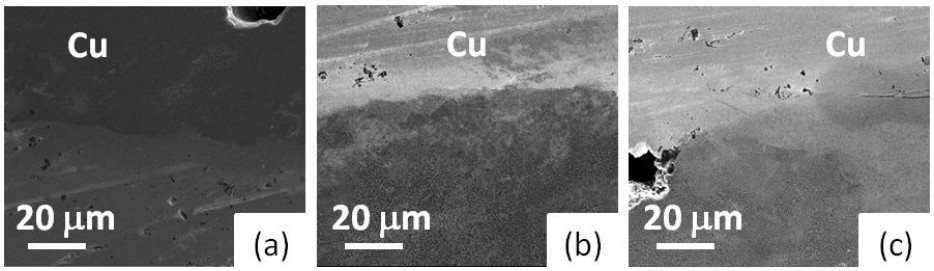

Figure 6: High magnification images of the tungsten layer cross section for Ni content 0% (a), 13% (b), 20% (c), and 30% (d). These samples were joined under 4000 lbs of pressure.

With the next image, Fig. 7, we highlight the join region on the copper side of the sample. With this, it is obvious that unlike the previous images this only shows three samples and excludes

To Table of Contents

the 0% sample. This is due to the fact that there was not a quality join on the copper side of the sample so we couldn't prepare an image to present. That aside, there is clear evidence of defects on the 30% sample, further demonstrating that it has undesirable qualities. However, both of the other samples have no sign of defects, indicating that they are both quality joins.

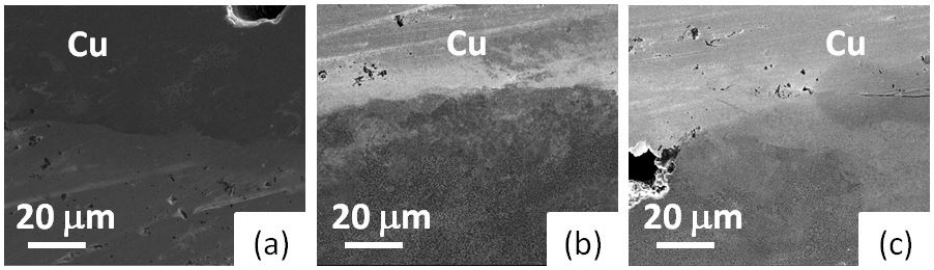

Figure 7: High magnification images of tungsten layer cross section for Ni content 13% (a), 20% (b), and 30% (c). These samples were joined under 4000 lbs of pressure.

Following from this, we changed the pressure under which the reaction occurs to further optimize the process. Typical results are shown for the 20% sample under 5000 lbs in Fig. 8. Examining this sample, there are virtually no pores and the layers show high quality joins on both side. Additionally, further investigation of the join layer shows, at high magnification, that there is an even distribution of reaction products, indicating a high quality with high thermal properties.

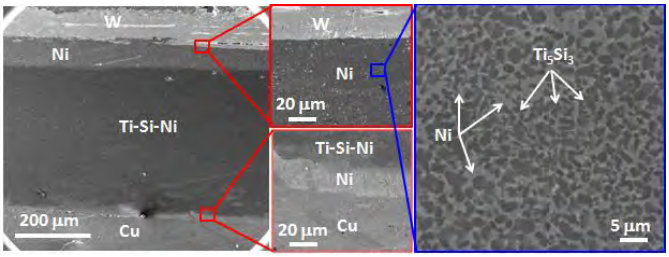

Figure 8: Images of join layer cross sections for Ni content 20%, joined under 5000 lbs of pressure, enlarged to show tungsten and copper layers, as well as join layer composition.

Finally, Fig. 9 presents the microstructure of the 20% sample after the heating test. From this, it is clear that the heating of the sample reduced the porosity and eliminated cracks. Therefore, reheating the mixture allowed it to expand to fill these previous defects - it improved the quality of the join.

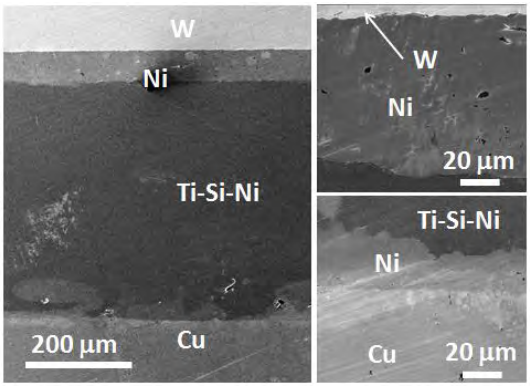

Figure 9: Images of join layer cross sections for Ni content 20% sample that underwent heat treatment.

4 Concluding Remarks

The optimal conditions for joining copper and tungsten were found to be with the configuration described in section 2.2, a reactive mixture of Ti_5Si_3 moderated with 20% Ni, under 5000 lbs of pressure. This results in a join that is free of cracks and pores. It was also demonstrated that this sample does not deteriorate through heating - remarkably it actually reduces and eliminates defects in samples. Future study would be to use the joined material and test it in an accelerator as a target backing to determine its behavior and effectiveness.

5 Acknowledgments

This work was supported by the National Science Foundation as part of the Notre Dame REU program and under Grant PHY-1068192. I would like to acknowledge Prof. Umesh Garg for his work directing and coordinating the Notre Dame REU program. For their continual support and fruitful discussion I would like to thank Prof. Alexander Mukasyan, Dr. Ya-Cheng Lin, Prof. Paul McGinn, and Tatyana Orlova.

References

[1] U.S. Department of Energy, *Accelerators for Discovery Science,* Accelerators for Americas Future, 70–83 (2010).

[2] Mukasyan, A. S. and White, J. D. E., *Combustion joining of refractory materials,* AInternational Journal of Self-Propagating High-Temperature Synthesis, **16** 154–168 (2007).

[3] Shiryaev AA. *Thermodynamics of SHS processes: an advanced approach.* Int J SHS, **4** 351–362 (1995).

Understanding the Role of Strontium in the Stability of $SrAu_3Ge$

Diana Gutierrez Zedano

Group: Professor Kathie Newman and Danielle McDermott

NSF/REU Program Summer 2013

University of Notre Dame

Department of Physics

Abstract

We study the effect of valence charge on the material properties of compounds with the geometry of experimentally synthesized $SrAu_3Ge$. By replacing strontium with barium, calcium, sodium, magnesium and cerium, we examine the geometry and bonding of a compound formed of gold-germanium octahedra. Using Density Functional Theory (DFT), we calculate the energy, geometry, and electronic structure for each compound. Initial calculations show the structure of $BaAu_3Ge$, $CaAu_3Ge$ and $MgAu_3Ge$ are similar to that of $SrAu_3Ge$ while cerium and sodium, which have a different valence charge than strontium, undergo structural rearrangements. A comparison between the compounds can help us understand the bonds between gold and germanium. These bonds call tell us whether the number of valence electrons contributes to the stability of gold-germanium bonds.

Introduction

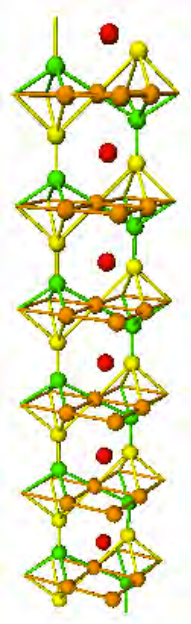

Figure 1: $SrAu_3Ge$

Part of the motivation to study this compound is because researchers have been able to synthesize it in a lab (Lin). The unit cell consists of nine atoms of which six are gold, two are germanium and one is strontium. Germanium, a semiconductor, and gold, a metal, form unusual bonds between each other, and thus can help us understand metal-semiconductor bonding. Also, understanding germanium-gold bonds allows us to assimilate the synthesis of germanium nanowires for which gold is used as a nano-catalyst (Gamalski). In addition, we believe that the formation of stable gold-germanium octahedra is due to the presence of strontium.

In this project, we have studied the effect strontium has on the geometry, Figure 1, and bonding of the compound. The strontium atom that sits between the octahedra was replaced with other atoms that have similar and different electronic charge to investigate the effect on the structure. We modified $SrAu_3Ge$ by switching the strontium atom with other elements to make $CaAu_3Ge$, $MgAu_3Ge$, $BaAu_3Ge$, $NaAu_3Ge$ and $CeAu_3Ge$ for which we found the lattice constant with minimum energy and the binding energy of each system. Also, measurements of the lengths of the basal gold-gold bonds and germanium-gold bonds in all of the compounds were made to compare all the structures with stable $SrAu_3Ge$.

Spanish Initiative for Electronic Simulations with Thousands of Atoms (SIESTA) and Density Functional Theory

SIESTA calculates the ground state properties of a many-body system using Density Functional Theory (DFT) which describes electron-electron interactions. SIESTA requires the positions of the atoms within the unit cell, the pseudopotentials, basis sets and the exchange correlation functional in the input file. The corresponding pseudopotential is placed on the position of the respective atom and the basis set describes the wavefunction. DFT allows us to reduce a complex system with N atoms each with 3 dimensions to a system described with the electronic density. By using functionals of the electronic density, the system is simplified.

SIESTA	Inputs
k-grid cut off	15 Ang
MD.TypeOfRun	cg
MD.NumCGsteps	100
MD.MaxCGDispl	0.1 Ang
MD.MaxForceTol	0.005 eV/Ang
MeshCutoff	200.0 Ry

Table 1

Atoms	Bond length
Au1-Ge	2.56 Å
Au1-Au2	2.83 Å
Au1-Au1	3.13 Å
Sr-Au1	3.53 Å
Sr-Au2	3.28 Å

Table 2: The experimental bond lengths.The basal gold is indicated by Au1 while the apical gold is denoted by Au2.

SIESTA Inputs and Procedure

The SIESTA inputs are listed in Table 1. As for the geometry the compound has a tetragonal lattice system with the experimental unit cell dimensions *a* and *b* equaling 6.26 Angstroms and *c* measuring 5.51 Angstroms. To determine the atomic coordinates of each atom, we used the experimental bond lengths listed in Table 2 (Lin).

The basis set for strontium was taken from the SIESTA database which was optimized for bulk cubic $SrTiO_3$. We believe this is a good approximation for the compound because pseudopotentials approximate the effect of each atom's core electrons with an effective potential. Calcium's, barium's pseudopotentials and basis sets were also taken from the SIESTA database which were optimized for $CaTiO_3$ and $BaTiO_3$ respectively. Sodium's pseudopotential was optimized for bulk Na. As for magnesium, the pseudopotential was taken from the SIESTA directories and no basis set was used, but the basis size was set to DZP.

To find the geometry of each compound with the minimum amount of energy, we varied the lattice constant for each of the compounds. The lattice constant ranged from 5.0 to 7.0 Å in increments of 0.1 Å. After identifying the minimum, we zoomed in and calculated the energy using more points to find a more precise lattice constant.

To calculate the bulk modulus, we used the data we obtained from changing the lattice constant as long as the system relaxed. Some systems did not relax, but they were toward the end of the range. We fit our data to the Murnaghan equation of state:

$$E(\Omega) = E_0 + \frac{B_O \Omega}{B'_O}\left[\frac{\left(\frac{\Omega_O}{\Omega}\right)^{B'_O}}{B'_O - 1} + 1\right] - \frac{\Omega_O B_O}{B'_O - 1}$$

Using Jmol, we measured the bond lengths between the atoms that make up the unit cell depicted in a software package, Figure 2. Figure 3 shows the Au1-Au1 lengths which were averaged. While Figure 4 shows the side view to highlight the length between the apical gold and the germanium atom. The binding energy for each compound was calculated by finding the total energy of each individual atom, adding all the atoms corresponding to each compound and comparing that result to the energy calculated using the entire compound. For the isolated atom calculations, we used 0.04 eV/Angstrom for the Md.MaxForceTol instead of 0.005 eV/ Angstrom.

Figure 2: Unit cell of $SrAu_3Ge$. Gold is depicted by yellow, Sr by cyan and Ge by grey.

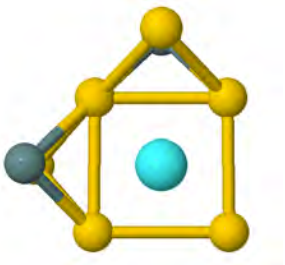

Figure 3: View looking from the top

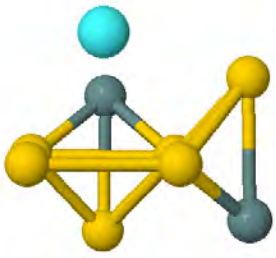

Figure 4: Side view

To Table of Contents

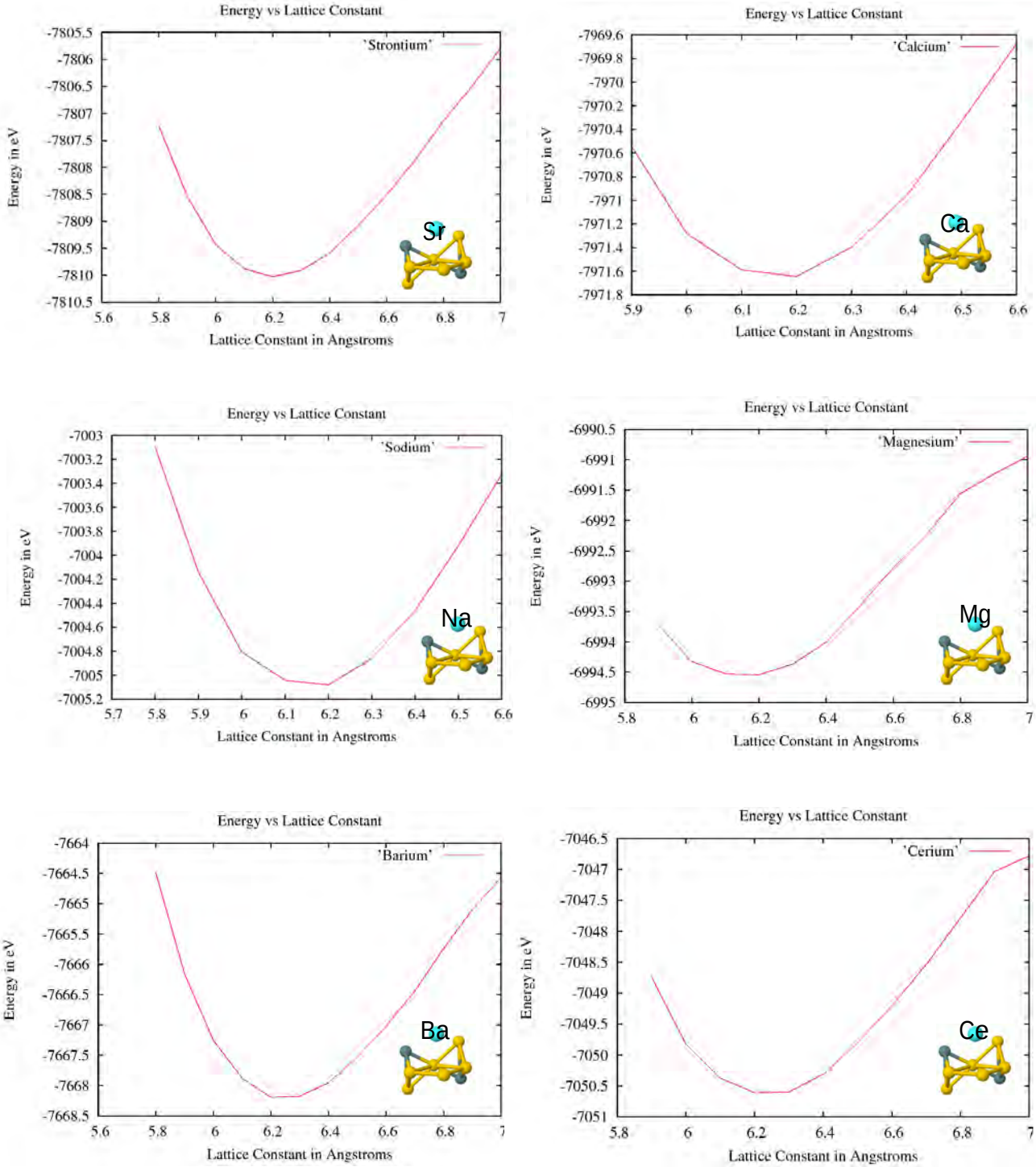

Figures 6-11: From left to right graphs of Energy vs lattice constant for $SrAu_3Ge$, $CaAu_3Ge$, $NaAu_3Ge$, $MgAu_3Ge$, $BaAu_3Ge$ and $CeAu_3Ge$.

To Table of Contents

Results

The energy versus lattice-constant figures for each of the compounds are depicted by figures 5-11. Most of the compounds have a minimum lattice constant of around 2.20 Angstroms. However, the minimum lattice constants for Magnesium and Cerium were not found by zooming in to the depicted graphs as mentioned in the previous section.

The bulk modulus for all the compounds are listed on Table 1. As you can see the bulk modulus for the experimentally synthesized compound $SrAu_3Ge$ is about four times smaller than that of the other bulk moduli. This eccentricity is most likely due to the compound's uniaxial negative thermal expansion along *c*. The researchers who experimentally synthesized $SrAu_3Ge$, heated the compound from 110K to 295K for which uniaxial negative thermal expansion along *c* was measured (Lin). In the horizontal direction, *a* and *b* expand while contractions happens vertically along *c*. Perhaps strontium is in part responsible for this property since switching it with other elements increases the bulk moduli. Also, the compound consisting of magnesium has a smaller bulk moduli compared to the rest but still larger than that of $SrAu_3Ge$.

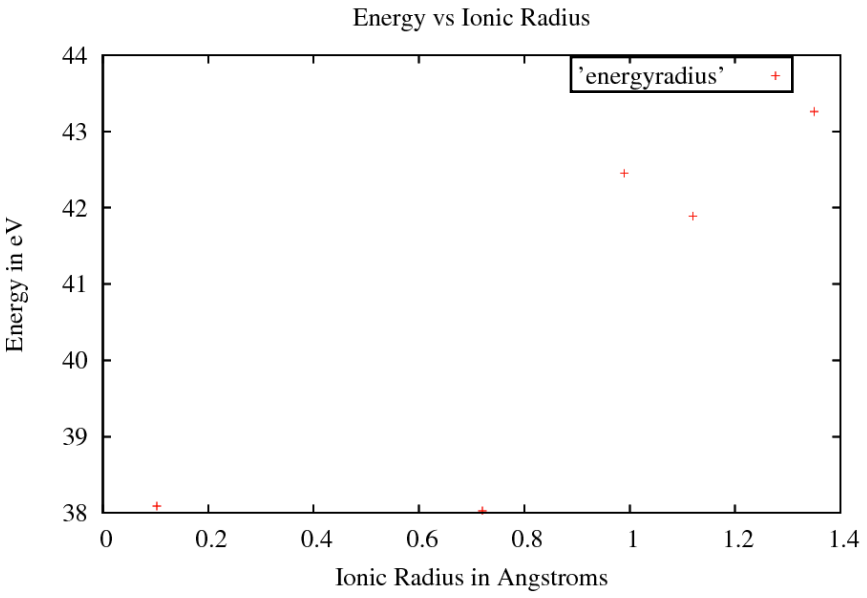

Figure 12: Binding energy in eV vs ionic radius in Angstroms for $NaAu_3Ge$, $MgAu_3Ge$, $CaAu_3Ge$, $SrAu_3Ge$ and $BaAu_3Ge$ from left to right.

Table 2 shows the binding energy

To Table of Contents

for each compound. A lower binding energy than that of $SrAu_3Ge$ may be of interest. With the binding energy, we can look for a relationship between it and the positions of the elements in the periodic table as shown in Figure 12. Finally Table 3 lists the average lengths measured using Jmol for all of the compounds.

System	Isolated Energy in eV	SIESTA Energy in eV	Binding Energy in eV
$SrAu_3Ge$	-7768.15	-7810.04	41.89
$BaAu_3Ge$	-7624.94	-7668.2	43.26
$CaAu_3Ge$	-7929.2	-7971.65	42.45
$MgAu_3Ge$	-6956.51	-6994.54	38.03
$NaAu_3Ge$	-6967	-7005.09	38.09
$CeAu_3Ge$	-7007.27	-7050.61	43.34
Au	-1118.73	-	-
Ge	-110.99	-	-
Sr	-833.79	-	-
Ba	-690.58	-	-
Ca	-994.84	-	-
Mg	-22.15	-	-
Na	-32.64	-	-
Ce	-72.91	-	-

Table 1: Binding energy in eV along with mid calculations

Compound	Lattice Constant	Bulk Modulus
$SrAu_3Ge$	6.18 Å	18.8 GPa
$BaAu_3Ge$	6.25 Å	70.36 GPa
$CaAu_3Ge$	6.16 Å	90.67 GPa
$MgAu_3Ge$	6.20 Å	38.97 GPa
$NaAu_3Ge$	6.16 Å	78.62 GPa
$CeAu_3Ge$	6.20 Å	88.7 GPa

Table 2: Lattice constant in Angstroms and bulk modulus in GPa for each compound.

Compound	Au1 - Au1 nm	Ge - Au2 nm	Ge - Au1 nm	* - Au1 nm
$SrAu_3Ge$	0.32725	0.304	0.2535	0.347
$BaAu_3Ge$	0.3205	0.305	0.255	0.35625
$CaAu_3Ge$	0.30225	0.304	0.253	0.34725
$MgAu_3Ge$	0.302	0.306	0.2545	0.40475
$NaAu_3Ge$	0.3025	0.304	0.25325	0.34875
$CeAu_3Ge$	0.307	0.304	0.254	0.34875

Table 3: The average lengths between atoms. The asterisk stands for the atom in place of strontium. Au1 is the basal gold and Au2 is the apical gold. Measurements are in nanometers

Conclusions

More calculations can be made to understand strontium's role in the structure of $SrAu_3Ge$ by calculating the phonon dispersion and the density of states of all the compound and making comparisons. In addition, further geometry calculations using the bond lengths can be made to find how much the strontium atom moved from the experimentally synthesized compound measurements.

Acknowledgements

I would like to thank Danielle McDermott and Professor Kathie Newman for helping me with the project. Many thanks also goes to Professor Garg, Lois Eslinger and Shari Herman for coordinating this program. Finally, I would like to thank the National Science Foundation for funding.

References

Lin, Qisheng and Corbett, John D. J. Am. Chem. Soc., 2012, 134 (10), pp 4877–4884

A. D. Gamalski, C. Ducati, and S. Hofmann, J Phys C 2011, 115, pp. 4413-4417 (2011)

http://www.uam.es/siesta

Carbon-14 AMS: Establishing a Carbon Dating Method at Notre Dame

Kirby Hermansen

2013 NSF/REU Program
Physics Department, University of Notre Dame

Professor Philippe Collon

Abstract: Accelerator mass spectrometry is a method detecting radioactive isotopes at very low concentrations. This is done with isobar separation that limits normal mass spectrometry. One of the applications of this tool is in radiocarbon dating. By determining the isotopic ratio $^{14}C/^{12}C$ in a specific sample, it is possible to determine the age of the sample. In this way, AMS is similar to standard mass spectrometry, but the inclusion of an accelerator allows for analysis of the particles at a higher energy, which affords smaller sample sizes and shorter experiment times. However, ^{14}C AMS is complicated by the presence of many contaminants, notably $^{7}Li_2$ and ^{14}NH, which maintain the same mass-to-charge ratio as ^{14}C and interfere with the detection of ^{14}C, lowering the sensitivity. Data collected in a July run on the 11-MV FN Tandem accelerator in the Nuclear Science Laboratory (NSL) confirm these contaminants, but a lack of sufficient beam time prevented the application of solutions. Noting the past problems and their possible solutions, new settings will be ready for full experimentation in the fall. Optimizing this procedure will then allow for the NSL to work in conjunction with other departments at Notre Dame on precise dating of artifacts and samples.

Background: In 1946 at the University of Chicago, Professor Willard Libby first discovered that the atmospheric production of ^{14}C ($t_{1/2}$=5730 years) due to cosmic radiation must be in equilibrium with the rate of disintegration of the radioisotope [1]. From here, it was then possible to date an organic object based on the amount of ^{14}C present in a sample. Once an organism dies it no longer produces ^{14}C, and with atmospheric production in equilibrium, no ^{14}C is added to the concentration. This leads to the standard half-life equation (Eq. 1) where N_0 is the initial number of atoms of ^{14}C, N is

$$N = N_0 e^{-\lambda t}$$

Equation 1

the final number of atoms, λ is the decay constant for an element, and t is the time elapsed. Since the starting concentration is equal to the standard ratio of $^{14}C/^{12}C$, and the decay constant of ^{14}C is known, the only unknowns that remain are the final concentration and the time. Carbon-dating processes seek to find the final concentration. The sample makeup could be found through the process of decay counting, where a decay rate is determined from a sample. From this decay rate, the abundance of an

isotope can be found. However, this process requires very large samples and a very large period of time to acquire sufficient counts of an isotope like ^{14}C. This process is dramatically improved through the use of AMS. AMS allows for a much smaller sample size and a much faster process time by using an accelerator setup to separate out and count the individual atoms in a sample. Once the system is calibrated correctly only a few calculations are necessary to achieve a much more precise age of a sample than by simple decay counting.

Setup: At the University of Notre Dame, the 11-MV Tandem Van de Graaff accelerator in the Nuclear Science Laboratory (NSL) is used to conduct AMS experiments. The setup is as follows (Fig. 1). Negative ions are injected from the MC-SNICS source (Multi

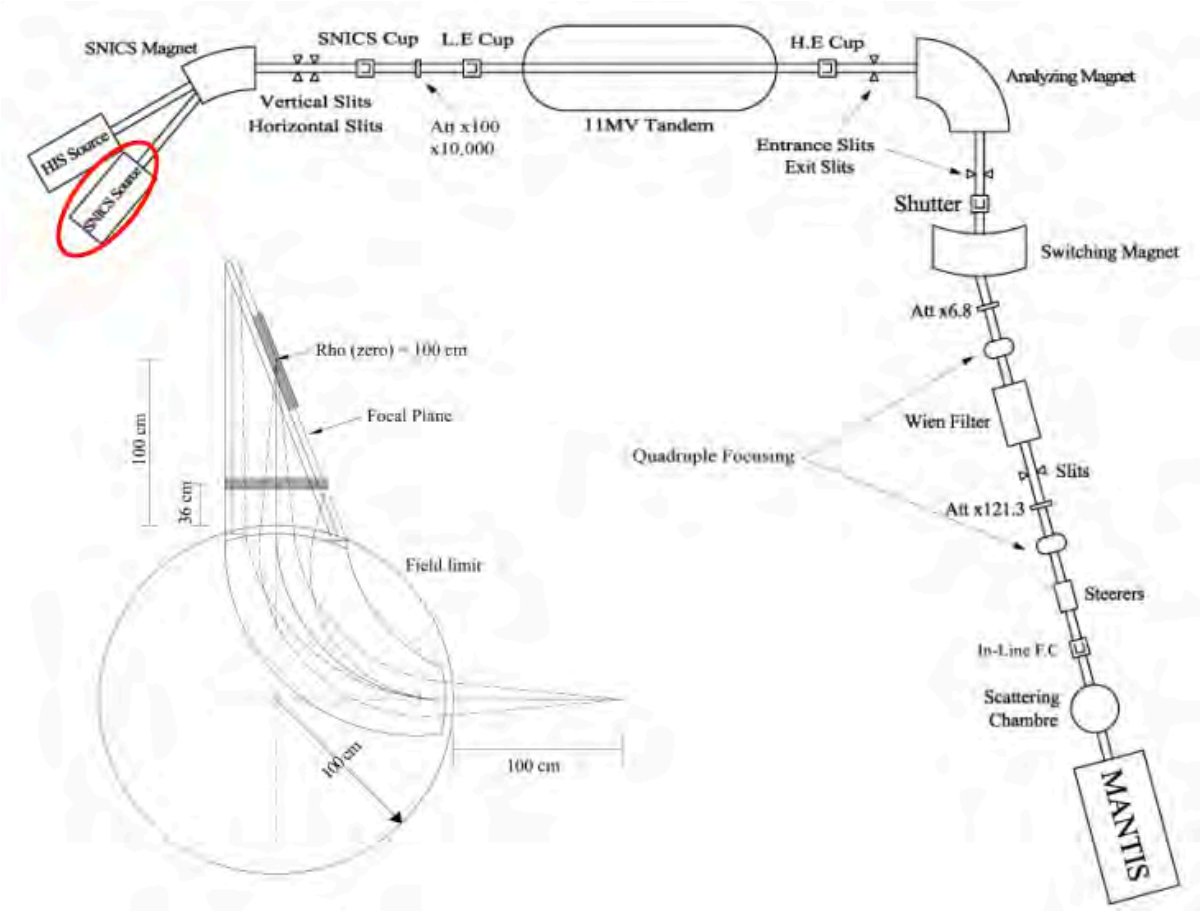

Figure 1

To Table of Contents

Cathode Source of Negative Ions via Cesium Sputtering) selecting a certain injection mass m at the SNICS (low-energy or LE) magnet. The beam then proceeds through the Tandem accelerator and is stripped to a charge state q across a potential V. Another m/q selection is done at the analyzing (high-energy or HE) magnet before entering the AMS specific beamline. Once in this beamline the beam passes through a Wien filter, which selects a certain velocity before reaching the silicon detector in the Scattering Chamber (SC). Important Faraday Cups include the SNICS, Shutter and SC cups.

Procedure: The goals of the experiment were as follows: 1) Establish a reproducible tune and scale a beam between ^{12}C, ^{13}C, and ^{14}C. 2) Establish a background for ^{14}C measurements. 3) Reach an acceptable sensitivity (a ratio of ~10^{-16} $^{14}C/^{12}C$) for ^{14}C dating to be possible. The cathodes used for this experiment included an International Atomic Energy Agency (IAEA) blank (zero ^{14}C) cathode, an IAEA C-6 sucrose ^{14}C-enriched sample [2], and a standard carbon sample (^{14}C-enriched) from PRIME Lab at Purdue. The accelerator was tuned to 3.5 MV and operated at a charge state of 4+ (for a total energy of 17.5 MeV) to maximize transmission levels. After tuning the beam, runs were conducted in fifteen minute intervals and running each cathode four times for an hour of total run time per cathode.

Data and Analysis: As is visible in Figures 2, 3, and 4, the data from the runs clearly identified a large number of counts in the region (as indicated by the arrows) where ^{14}C would be expected due to the energy of the particles. However, the same peak was visible in not only the enriched cathode (Fig. 2) and the standard sample (Fig. 3), but also

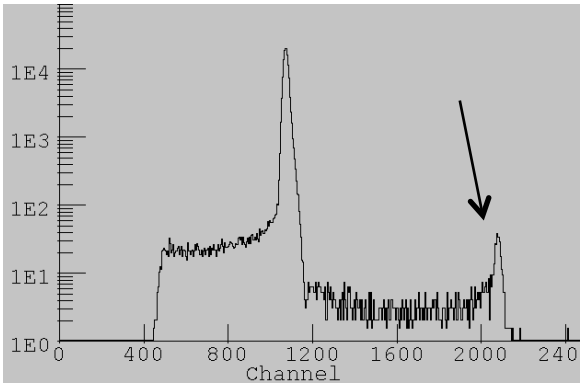

Figure 2: Sum of 2 runs (30 min total) on C-6

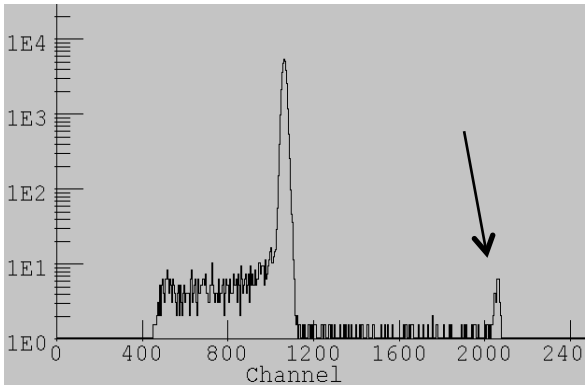

Figure 3: Sum of 2 runs (30 min total) on the standard

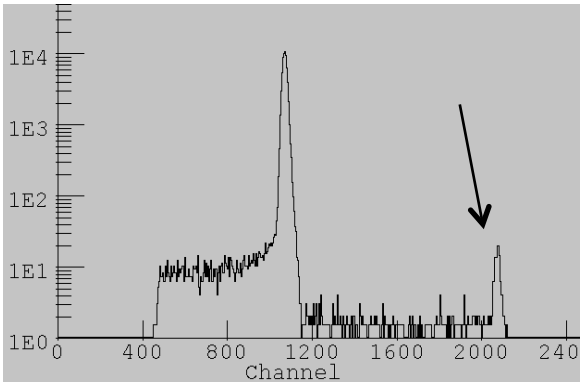

Figure 4: Sum of 2 runs (30 min total) on the blank

in the blank cathode (Fig. 4). This is clearly a major problem as the IAEA blank is certified to contain absolutely zero amounts of ^{14}C. What is actually being read by the detector is not known for a certainty. A number of possibilities include: 1) severe memory effects on the detector resulting in counts being read from previous runs, 2) injection of hydrides of ^{12}C or ^{13}C at mass 14 that are mostly separated along the beamline but leave behind a tail that swamps out the ^{14}C, and 3) when injecting mass 14, some mass 15 also is allowed (particularly $^{14}NH^-$ which breaks up into ^{14}N in the terminal and is very difficult to separate from ^{14}C).

The first possibility is unlikely to be a major cause, especially because the ^{14}C peak appeared on the first blank runs, which were conducted before any ^{14}C was sent through to the detector. Additionally, the runs showed no noticeable trend of a drop off in counts as the runs continued (see Appendix 1).

Ion	13C 4+	14C 4+	14NH 4+	7Li 2+
M(u)	13.0034	14.003241	14.003074	7.016004
E (MeV)	17.5	17.5	16.32505784	8.75
q	4	4	4	2
vel (m/s)	1.61E+07	1.55E+07	1.50E+07	1.55E+07
v/c	0.05393	0.05197	0.05019	0.05192
%Diff From 14C	3.6361%	0.0000%	-3.5354%	-0.1027%

Table 1

The second possibility is unlikely as well because although it would be possible for ^{13}C to survive the analyzing magnet, the Wien filter should certainly be able to separate ^{13}C with its highly disparate velocity from ^{14}C (see Table 1). Priller et al. 1997 discuss both this ^{13}C tailing and the possibility of ^{14}NH contamination in experiments at VERA in the 1990s [3]. In that study a 3-MV tandem accelerator was operated at a 3+ charge state tuned to detect ^{14}C. Results showed a heavy background with a large ^{13}C peak (Figure 5a). A Wien filter was then implemented to separate out most of this background into the much more condensed spectra visible in Figure 5b. However, while this demonstrates the efficiency of the Wien filter, not all of the ^{13}C was eliminated.

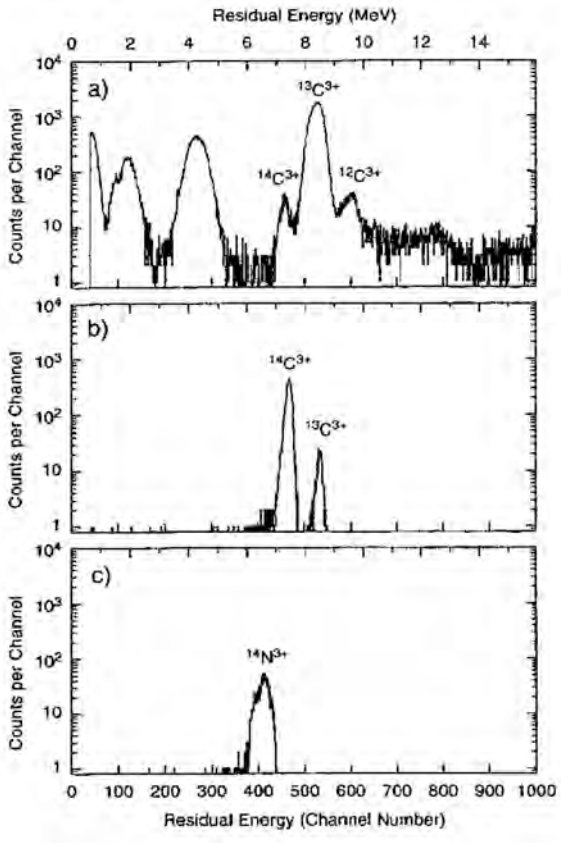

Figure 5

Additionally, ^{14}N will come in at a velocity that is actually closer to the velocity of ^{14}C (Table 1) and so would be equally difficult to fully sort out. The ^{14}N peak visible in Figure 5c is the result of an explicit injection of mass 15 into the system while the rest of the system was tuned to detect ^{14}C.

With ^{14}N proving to be a significant problem, it is then important to guarantee

To Table of Contents

that only mass 14 is injected into the system. However this currently cannot be known for a certainty. In past experiments with ^{55}Mn, when looking to inject mass 55, mass 56 particles ($^{55}MnH^-$ instead of ^{55}Mn) were also injected, leading to problems at the detector [4]. This is a problem that will eventually be fixed with the new Low-Energy Injection system, but for the time being there is unfortunately little that can actually be done to correct this problem.

There is an additional peak that stands out among the data visible in Figures 2, 3, and 4. Since it is coming in at about half the energy that would be expected for ^{14}C, it is presumably a peak in $^{7}Li^{2+}$ that was injected as $(^{7}Li)_2^{4+}$ and broke apart in the terminal. The resultant ^{7}Li would then hit the detector at about half the energy of ^{14}C but would be undisturbed by the Wien filter as it comes in at a velocity very close to that of ^{14}C as evidenced in Table 1. This being the case it is clear that it will be very difficult to separate out this ^{7}Li peak at the 4+ state. However, shifting to a 3+ charge state would of course eliminate the presence of ^{7}Li entirely as it would not exist at that state. This is not absolutely necessary, as the peak of ^{7}Li is considerably separated from the ^{14}C region so it would be trivial to simply ignore the ^{7}Li altogether, but getting a clear and isolated peak is preferable.

Another problem not evident in the previous figures but that is hinted at in Appendix 1 is the fluctuation of counts detected and eventual drop off in transmission throughout the course of the experimental runs. Over the course of the 18 total runs, there is no correlation between the beam current produced in the source and the counts read on the detector. The two scrapped runs were cancelled precisely because of this massive fluctuation in counts detected. For those two scrapped runs a moderate current of only a

few μA resulted in thousands of counts per second on the detector, and subsequently the cancellation of the runs in order to protect the detector from damage.

Additionally, Appendix 1 alludes to the drop in overall transmission, specifically towards the conclusion of the experiment. Though the initial transmission was about 2.5% from the SNICS to the SC (see Fig. 1), following the final run a significant transmission value was unable to be obtained entirely. The experiment ended with a transmission nearing 0%. This could be due to a number of problems within the system, but given the time constraint it was impossible to properly troubleshoot. Both the fluctuation in counts and drop in overall transmission are important to consider for future runs.

Conclusion and Outlook: In April 2013, preliminary ^{14}C runs were conducted in order to get a bearing on exactly where the program was. At that time it appeared prudent to operate under a 4+ charge state so as to maximize the transmission through the beamline (as $^{14}C^{4+}$ has a better transmission rate than $^{14}C^{3+}$). However, the overshadowing presence of ^{7}Li swamping the detector seems to outweigh any benefit gained by this move to a 4+ charge state. Additionally, the optimum terminal voltage for $^{14}C^{4+}$ is around 5.5 MV for a foil stripper tandem [6] like that in the NSL. It then appears to be the case that neither the optimum charge state nor the optimum terminal voltage for that charge state was used for these runs. Going forward both charge states remain strong possibilities. However, it is important that for the 3+ state a terminal voltage of 3.5 MV is used while for the 4+ state 5.5 MV is required. Both possibilities should be explored in order to guarantee that the resulting method is as efficient as possible.

Since it is impossible to discern for a certainty what is present in the peaks near the ^{14}C region, it is also impossible to determine the exact counts of ^{14}C for each run, and therefore impossible to determine a sensitivity ratio ($^{14}C/^{12}C$) and from that date an actual object. This is among the primary goals that need to be accomplished in the fall, as already there are potential suitors at Notre Dame requiring objects to be dated.

In summary, the goals moving forward are to 1) compile enough data to establish an accurate background for ^{14}C, and 2) use this compiled background to reach an acceptable sensitivity level from which to date objects. Unfortunately these goals are rather similar to those from the beginning of the summer. However with the knowledge gained during the brief runs completed in July the goals can be more efficiently completed and the problems more easily solved.

References:

[1] W.F. Libby (1946). "Atmospheric Helium Three and Radiocarbon from Cosmic Radiation". *Physical Review* **69** (11–12): 671–672.

[2] "Reference Sheet for Quality Control Material." *International Atomic Energy Agency (IAEA)*. N.p., 30 Mar. 2007. Web. 01 Aug. 2013.

[3] A. Priller, R. Golser, P. Hille, W. Kutschera, W. Rom, P. Steier, A. Wallner and E. Wild, "First performance tests of VERA", *Nucl. Instrum. and Meth. B* 123 (1997) 193-198.

[4] P. Collon. "Low Energy Injection MRI." January 2013.

[5] Tuniz, C. *Accelerator Mass Spectrometry: Ultrasensitive Analysis for Global Science*. Boca Raton, FL: CRC, 1998. 25-26. Print.

Cathode #	Run #	Start Current (μA 12C)	End Current	Avg. Current	Counts in 14C Region	Counts/(s*(μA 12C))	Centroid of Peak in 14C Region
14 (blank)	6	1.435	5.938	3.6865	730	0.220022002	2080.66
	7	6.29071	7.177	6.733855	2970	0.490061042	2075.64
	8	7.308	7.322	7.315	348	0.052859421	2079.38
	9	7.457	8.06	7.7585	1419	0.203217976	2074.11
17 (C6)	10	0.805	1.863	1.334	929	0.773779777	2072.34
	11	2.891	0.936	1.9135	95	0.055163604	2074.02
	12	scrapped					
	13	scrapped					
14 (blank)	14	2.7133	3.3309	3.0221	273	0.100371706	2067.04
	15	3.4066	9.592	6.4993	152	0.025985704	2070.41
	16	9.771	10.861	10.316	253	0.027250011	2071.11
	17	10.927	10.698	10.8125	136	0.013975594	2070.32
8 (standard)	18	0.438	2.072	1.255	132	0.11686587	2064.02
	19	2.089	2.303	2.196	112	0.056668691	2061.81
	20	2.338	2.521	2.4295	41	0.018751	2057.31
	21	2.549	2.668	2.6085	48	0.020445978	2054.83
14 (blank)	22	9.923	10.674	10.2985	13	0.001402578	2044.82
	23	10.143	11.096	10.6195	4	0.000418517	2045.02

Appendix 1
Start and end currents were read from the SNICS Faraday Cup

Magnetic Field of an Accretion Disk and the Formation of Relativistic Jets

Jared Johnson

2013 NSF/REU Program

Physics Department, University of Notre Dame

Project GRAND

Advisor:

John Poirier

Contributors:

Adrien Saremi

Aaron Sawyer

Magnetic Fields and the Formation of Relativistic Jets

Abstract: When matter falls towards a black hole, it will form a disk around the black hole known as the accretion disk. Accretion disks give rise to relativistic jets coming from the central object. The hypothesis is that the twisting of the magnetic field produced by the accretion disk collimates the outflow along the rotation axis of the central object, so that when conditions are suitable, a jet will emerge from each face of the accretion disk.[4] Along with the theory that the magnetic field is twisted due to the spin of the black hole, a particles motion in the *z* direction, that of the rotation axis, can be associated with the formation of relativistic jets. We have constructed a model of the magnetic field produced by an accretion disk around a black hole in an active galactic nucleus, and used it to show that particles coming off the accretion disk move in the *z* direction. A computer program was created to simulate the motion of a particle in the magnetic field. The particle is shown to leave its circular motion and move in the *z* direction.

Magnetic Field for an Accretion Disk

The magnetic field due to a current carrying loop is described by the Biot-Savart Law. The Biot-Savart Law (1.11) gives an expression for the magnetic field contribution, $d\vec{\mathbf{B}}$, from the current source, I $d\vec{\mathbf{s}}$, with μ_0 (1.12) as the *permeability of free space constant*. Let *r* denote the distance from the current source to the field point, and **r** as the corresponding unit vector.

$$d\vec{\mathbf{B}} = \frac{\mu_0}{4\pi}\frac{I\, d\vec{\mathbf{s}} \times \hat{\mathbf{r}}}{r^2} \qquad (1.11)$$

$$\mu_0 = 4\pi \times 10^{-7}\ \mathrm{T \cdot m/A} \qquad (1.12)$$

A circular loop of radius R in the *xy*-plane carries a current *I*, as shown in Figure 1.13. The loop is symmetrical about the *x* and *y* axes.[3]

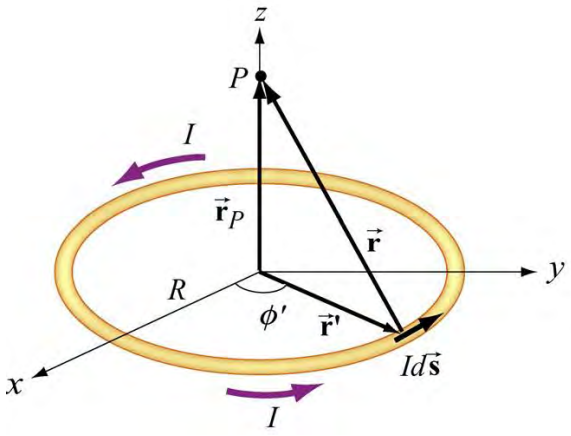

Figure 1.13 Circular loop carrying current.

We have imagined that the source point not be on the *z*-axis, but somewhere in the *yz*-plane. Thus the field point's position vector is given by $\overrightarrow{\mathbf{r}_p} = y\hat{\mathbf{j}} + z\hat{\mathbf{k}}$ and the position of the field point from the loop is given by $\vec{\mathbf{r}} = -Rcos(\varphi')\hat{\mathbf{i}} + (y - Rsin(\varphi'))\hat{\mathbf{j}} + z\hat{\mathbf{k}}$.

In Cartesian coordinates, the differential current element can be written as

$Id\vec{\mathbf{s}} = IRd\varphi'(-\sin(\varphi')\hat{\mathbf{i}} + \cos(\varphi')\,\hat{\mathbf{j}})$ and the cross product as

$Id\vec{\mathbf{s}} \times \hat{\mathbf{r}} = IR\big(zcos(\varphi')\hat{\mathbf{i}} + zsin(\varphi')\hat{\mathbf{j}} + \big(R - ysin(\varphi')\big)\hat{\mathbf{k}}\big)d\varphi'$.

The x, y, and z components of $\vec{\mathbf{B}}$ at position $\overrightarrow{\mathbf{r}_p}$ are given by

$$\mathbf{B}_x = \frac{\mu_o IR}{4\pi}\int_0^{2\pi} \frac{zcos(\varphi')\,d\varphi'}{((-Rcos(\varphi'))^2 + \big(y - Rsin(\varphi')\big)^2 + z^2)^{\frac{3}{2}}}$$

To Table of Contents

$$\mathbf{B}_y = \frac{\mu_o IR}{4\pi}\int_0^{2\pi} \frac{z\sin(\varphi')\, d\varphi'}{((-R\cos(\varphi'))^2 + \left(y - R\sin(\varphi')\right)^2 + z^2)^{\frac{3}{2}}}$$

$$\mathbf{B}_z = \frac{\mu_o IR}{4\pi}\int_0^{2\pi} \frac{R - y\sin(\varphi')\ d\varphi'}{((-R\cos(\varphi'))^2 + \left(y - R\sin(\varphi')\right)^2 + z^2)^{\frac{3}{2}}}$$

The magnetic field in the *x* direction is determined to be zero as we have chosen field points in the *yz*-plane and the loop is symmetrical about the *x* and *y* axes. We then computed the magnitude of the magnetic field in the *yz*-plane in terms of *y* and *z* coordinates. Using our FORTRAN computer program, we computed these integrals given by Biot-Savart by summing the magnetic field over small portions of the loop. Figure 1.14 shows the lines of magnetic force for a single loop, interpolated from the magnetic field data given by our program. The values for the variables were chosen for graphical convenience.

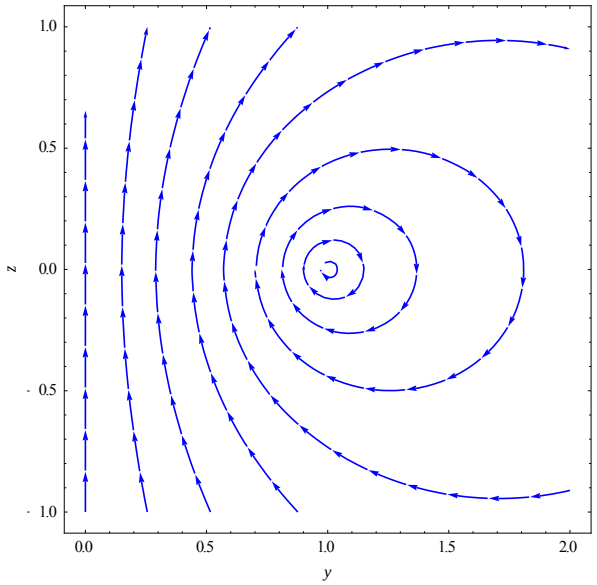

Figure 1.14 Lines of magnetic force in the *yz*-plane, for a current carrying loop of radius 1.0 and current 1.0 A.

To obtain magnetic field data for a disk in the *xy*-plane with surface current, a simple addition to our original program was made. We now summed our original integration for many rings in between the inner and outer radius of the disk. Once again for graphical purposes, we have assumed the disk to have a constant current of 1.0 A, an inner radius of 1.0, and an outer radius

of 2.0. Figure 1.15 illustrates the lines of magnetic force for this disk. We noticed that the magnetic field gets much larger near the disk and at positions above the disk the magnetic field is primarily in the *y* direction. For an accretion disk in active galactic nuclei, the current varies as $\frac{1}{\sqrt{R}}$. The magnetic field lines due to an accretion disk are shown in Figure 1.16. The spacing of the lines is inversely proportional to their magnitude of magnetic field.

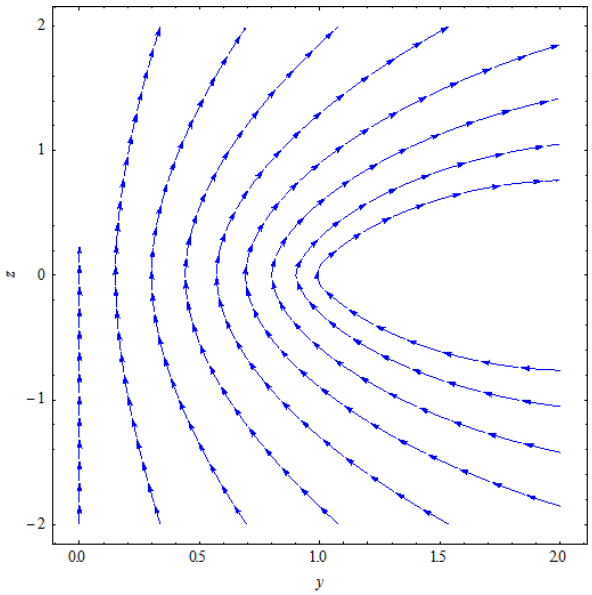

Figure 1.15 Lines of magnetic force for a disk in the *yz*-plane with inner radius 1.0 and outer radius 2.0 and constant current.

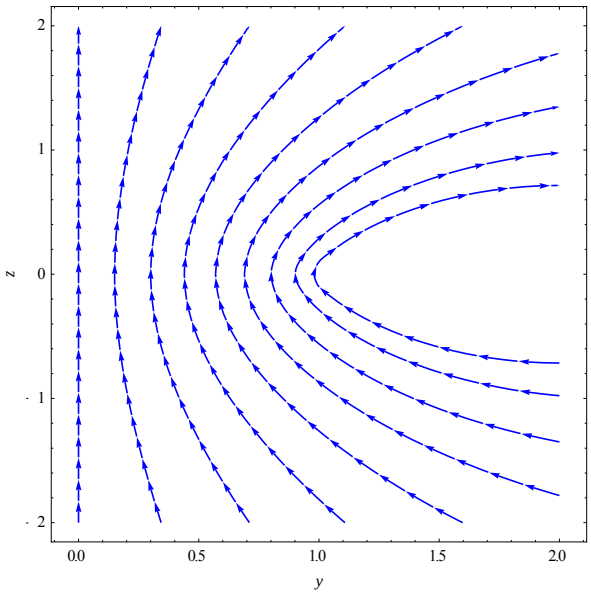

Figure 1.16 Lines of magnetic force for a disk in the *yz*-plane with inner radius 1.0 and outer radius 2.0 and current varying as $\frac{1}{\sqrt{R}}$.

The magnetic fields are plotted in 2D, but can easily be thought of as a representation for the 3D image as the loop or disk has rotational symmetry about the *z*-axis.

Formation of Relativistic Jets

Some accretion disks produce twin jets of highly collimated and fast outflows that emerge from opposite sides of the disk.[2] These jets are called relativistic jets. The direction of the jet ejection

To Table of Contents

is determined by the spin axis of the black hole. Around the black hole, there is a mathematically defined surface called the event horizon. The event horizon is a boundary in spacetime where events inside cannot affect an outside observer. It is the boundary at which the gravitational pull becomes so great that no matter or radiation can escape. The radius of the black hole is defined by the event horizon. For a non-rotating black hole, the radius is proportional to the mass of the black hole. A rotating, uncharged, spherically-symmetric black hole is known as a Kerr metric. The Kerr-Newman metric is a charged, rotating black hole. We assumed a Kerr metric.

The current model states that relativistic jets are likely formed by the twisting of the magnetic field lines from the accretion disk causing matter to collimate along the rotation axis of the central object. Magnetic field lines are likely twisted by the spin of the black hole twisting space.[1] If a particle is able to move in the vertical direction and we include the twisting of the magnetic field, this may be an accurate model for how relativistic jets form. In our model, we showed that a particle near the accretion disk is able to get out of its circular motion and take off in a vertical trajectory.

Motion of Particles

A particle's motion in the magnetic field due to an accretion disk is simulated to see that particles are redirected from their circular orbit into a vertical trajectory. The force on the particle due to electromagnetic fields is the Lorentz force 1.17. The Lorentz force equation was used along with Newton's second law 1.18 to describe the velocity of the particle at a certain point in time.

$$F = q\left(\vec{v} \times \vec{B}\right) \tag{1.17}$$

$$F = \frac{d\vec{p}}{dt} \tag{1.18}$$

$$\frac{d\vec{p}}{dt} = q(\vec{v} \times \vec{B})$$

$$\begin{pmatrix} \Delta v_x/\Delta t \\ \Delta v_y/\Delta t \\ \Delta v_z/\Delta t \end{pmatrix} = \frac{q}{m}\begin{pmatrix} v_x \\ v_y \\ v_z \end{pmatrix} \times \begin{pmatrix} B_x \\ B_y \\ B_z \end{pmatrix} = \frac{q}{m}\begin{pmatrix} v_y B_z - v_z B_y \\ v_z B_x - v_x B_z \\ v_x B_y - v_y B_x \end{pmatrix}$$

For a sufficiently small Δt, the change in velocity remains constant over that period of time. The motion of the particle is thus tracked using the change in velocity found by the equations:

$$\begin{cases} \Delta v_x = \frac{q}{m}(v_y B_z - v_z B_y)\Delta t \\ \Delta v_y = \frac{q}{m}(v_z B_x - v_x B_z)\Delta t \\ \Delta v_z = \frac{q}{m}(v_x B_y - v_y B_x)\Delta t \end{cases} \quad (1.19)$$

Constants and initial conditions are defined so that the motion of a particle can be observed over one hundred steps of Δt.

$$\Delta t = 5 \times 10^{-10}\ s$$

$$q/m = 1.76 \times 10^{11}\ C.kg^{-1}$$

$$x_0 = 0.0$$

$$y_0 = 1.1 \rightarrow 1.5$$

$$z_0 = 0.2$$

$$\vec{v} = 10^8 \hat{\imath}\ m/s$$

$$I = \frac{20.0}{\sqrt{R}}\ A$$

To Table of Contents

First the initial conditions and position are read into our computer program. For this position, the magnetic field in each direction is computed. Then using equations (1.19), the change in velocity is found. The particle's velocity is now given by $\overrightarrow{v_f} = \overrightarrow{v_i} + \Delta\vec{v}$. The particle's new position $\overrightarrow{R_f}$ is thus given by $\overrightarrow{R_f} = \overrightarrow{R_i} + \vec{v} \times \Delta t$. This process is repeated for one hundred steps of Δt. Random steps were checked by hand calculations in which the magnetic field and change in position were both verified.

The position vector was recorded at each step and plotted in Mathematica to obtain a visual representation of the particles motion in this magnetic field. Particles with initial positions from $y_0 = 1.1 \rightarrow 1.5$ are plotted.

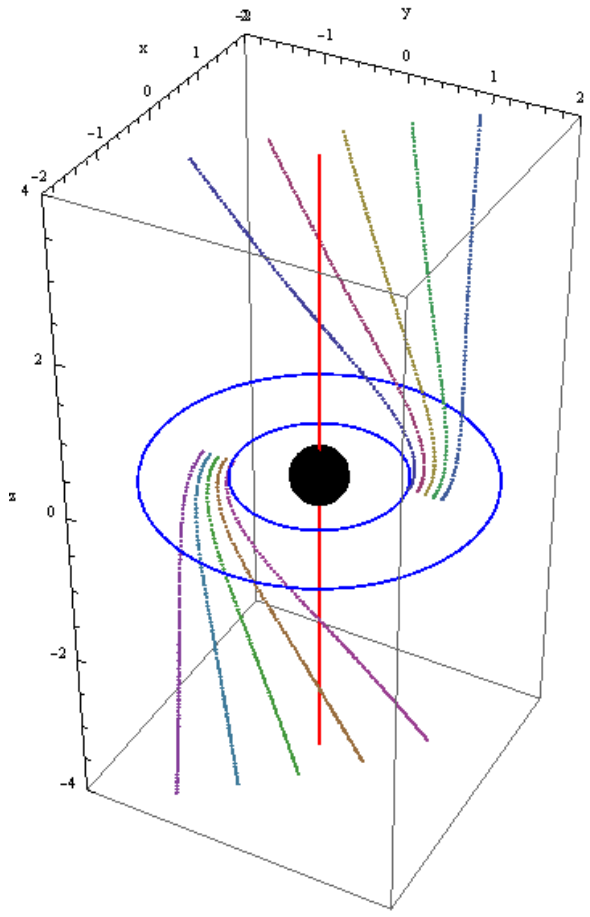

Figure 1.20 Three-dimensional image of a particles motion in the magnetic field produced by an accretion disk. The inner and outer radius of the accretion disk is shown by the blue rings. The axis of rotation is given by the red line.

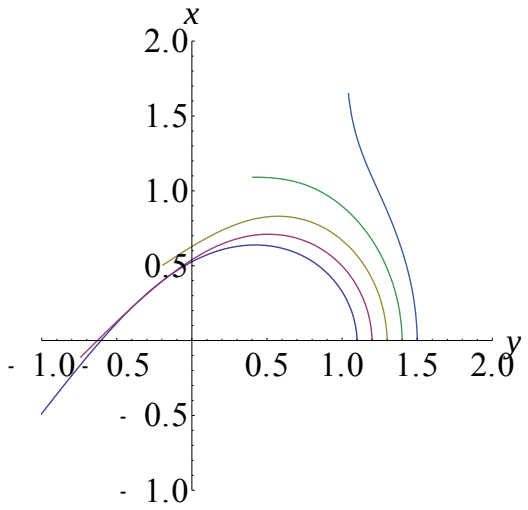

Figure 1.21 Trajectory of particles in the *xy*-plane.

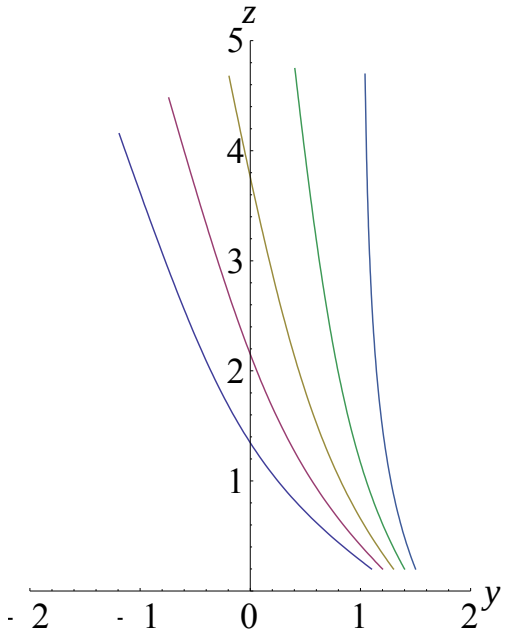

Figure 1.22 Trajectory of particles in the *yz*-plane.

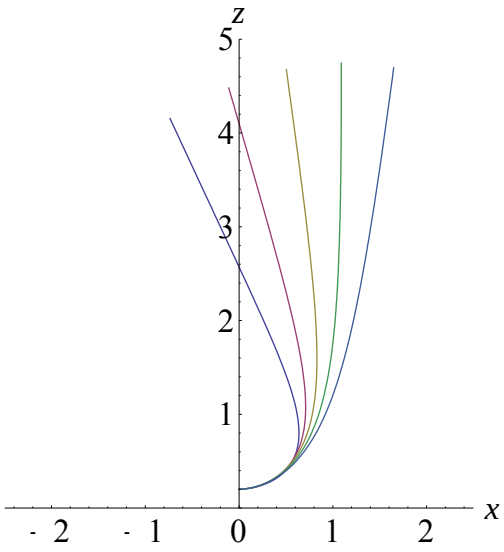

Figure 1.23 Trajectory of particles in the *xz*-plane.

We can see that particles that start near the accretion disk quickly leave their circular motion and move in the z direction.

Conclusion

The formation of relativistic jets has two key components. The first component being that the particles are able to move upwards along the axis of rotation without continuing in a circular motion. The second being the twisting of the magnetic field lines due to the spin of the black hole. We have successfully constructed a model that shows a particle's ability to move vertically in the same direction as the relativistic jets.

Acknowledgments

This work was supported by the National Science Foundation and conducted at the University of Notre Dame. Thanks to Thomas Catanach of Cal Tech, Mark Caprio of the University of Notre Dame, and Michael Sostarecz of Monmouth College for their assistance in using Mathematica. Also a special thanks to my advisor Dr. John Poirier for his advice and guidance throughout the summer on this project.

Works Cited

1. Blandford, R. D., & Znajek, R. L. 1977, MNRAS, 179, 433

2. Ferrari, Attilio. "MODELING EXTRAGALACTIC JETS." Cal Tech, 03 Mar. 1998. Web. 01 Aug. 2013.

3. "Sources of Magnetic Fields." *Chapter 9*. MIT, n.d. Web. 1 Aug. 2013.

4. Urry, C. Megan. "Evidence for Ultra-Energetic Particles in Jet from Black Hole." *YaleNews*. Yale University, 20 June 2006. Web. 01 Aug. 2013.

Simulating Stellar Spectra

Edward Kielb

2013 NSF/REU Program

Physics Department, University of Notre Dame

Advisor:

Professor Justin Crepp

Abstract:

iLocater is a precision near-infrared Doppler spectrometer currently being designed and constructed for the Large Binocular Telescope. In order to ensure the accuracy of the radial velocity extraction method of the instrument, I had to simulate a reliable stellar survey of stars to test the method on. Apart from laying out spectra on our detector and simulating a variety of potential perturbations ranging from faulty pixels to photon noise, the efficiency of the simulations were essential in order to be capable of simulating large surveys in a reasonable amount of computer time.

Introduction:

The iLocater (or infrared Large Binocular Telescope Exoplanet Recovery) project involves designing, coding, and constructing a near-infrared (NIR) Doppler spectrometer built to interface with the Large Binocular Telescope (LBT) in Arizona. It is a spectrometer designed for an adaptive optics system (one that corrects for the turbulence in the Earth's atmosphere) in order to obtain a radial velocity (RV) measurement for nearby stars in the near infrared range (NIR) that is unprecedentedly accurate (within 1 m/s).

The iLocater project was first inspired by the results of NASA's *Kepler* space mission, which showed that the frequency of planets similar to the mass of the earth is significantly higher around stars with lower mass, in particular M-Dwarf stars (stars which are smaller than the Sun) (See Figure 1 on the next page). There are a

number of reasons why M-Dwarfs are the best place to look for Earth-like planets, among them:

1. M-Dwarfs represent the most abundant type of star in the universe
2. M-Dwarfs have the highest planet density (Figure 1)
3. M-Dwarfs are incredibly stable, and will not explode as our sun will for a much longer period of time
4. Smaller stars have larger Doppler shifts than larger stars do, which makes it easier to detect planets in the habitable zone.

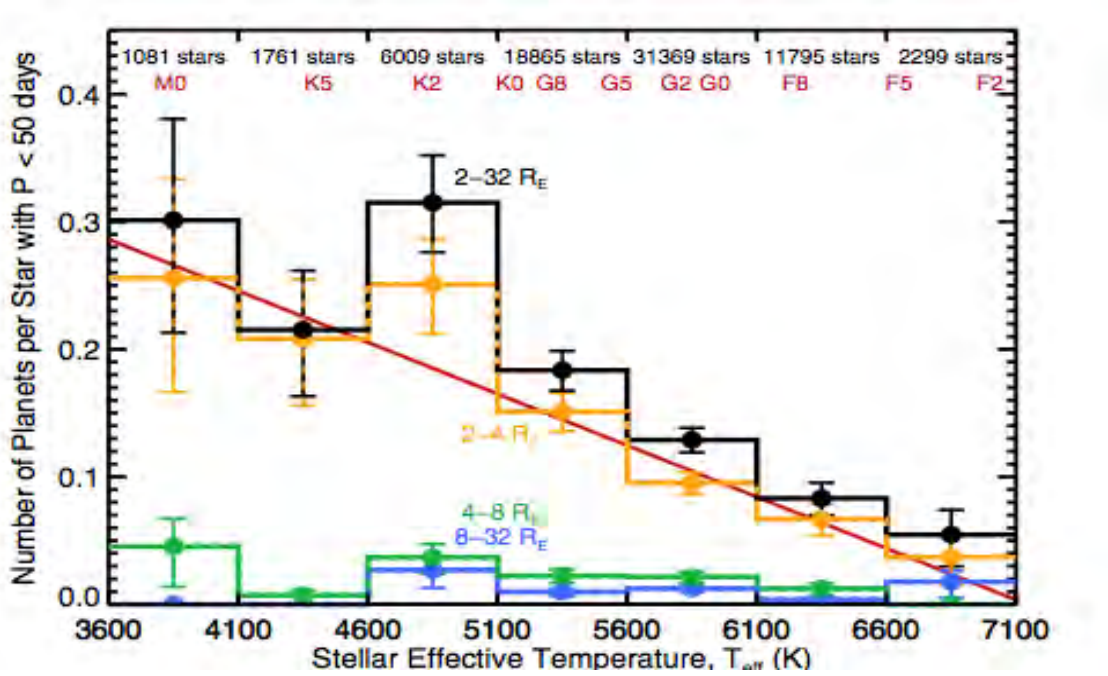

Fig. 1*: The Kepler Mission demonstrated that the frequency of planets around lower mass stars with low orbital periods is higher than around high mass stars. This means that iLocater will be searching among the most fruitful group of stars (Howard et all)*

To Table of Contents

A major part of this project is creating the radial velocity extraction method whereby the instrument will extract a radial velocity/time graph from the light absorption lines present on the detector. In order to ensure the accuracy of this method, I was tasked with creating a method of accurately simulating stellar spectra with specific parameters to test the radial extraction method on. In addition to laying out simulated spectra on our detector, I had to create sub-functions for the simulation program that dealt with various potential pitfalls that iLocater will have to deal with, including faulty pixels, photon noise, dispersion truncation, and dark current. Finally, the simulation program had to run at a certain efficiency in order that it could create the thousand or more images required for a typical survey in a reasonable amount of time (at most around a day).

Laying out a sample spectra

The first step towards my final goal was simply to create one "order" of light absorption onto a dark detector. The different orders of a stellar spectra arise as a result of the incoming light travelling through a prism and the resulting cross dispersion; in the case of our detector, the final product would have thirteen such "orders", one on top of the other. The first step towards creating even one of these orders, however, was determining how light realistically would appear on the sample detector, which could simply be taken as a matrix with dimensions equal to the pixel dimensions of our final detector. The easier determination to make was that each order roughly ran across the detector in such a way as to be able to be approximated by a second order polynomial, or some f(x)=A+Bx+Cx^2. The more difficult determination, however, was how to model the intensity of those orders at

each pixel surrounding an order's curve. This is because that intensity follows roughly a Gaussian distribution around each peak (with the peak value governed by the aforementioned second-order polynomial), or in other words roughly could be approximated by the equation $I = c * e^{-\alpha*(\Delta z)}$, where c is the detector's spectral resolution defined as $\frac{\lambda}{\Delta\lambda}$ at a wavelength of one micron (or 10^{-6} meters), where Δz is the distance between the point at which the intensity is being calculated and the nearest point on the order polynomial it belongs to, and where α is a measure of the full width half max of the Gaussian function. The calculation of Δz turns out to be no trivial task, but after some geometric derivation a very good approximation can be made as: $\Delta z \approx (\mathrm{f(x)} - \mathrm{y}) * \cos(tan^{-1}\left(\frac{df}{dx}\right))$, where f(x) is the polynomial governing the shape of the order being laid out on the detector, and x and y are axes referencing the dimensions of the detector pixels. The result of doing this twice (for the two telescopes in the LBT) can be seen below:

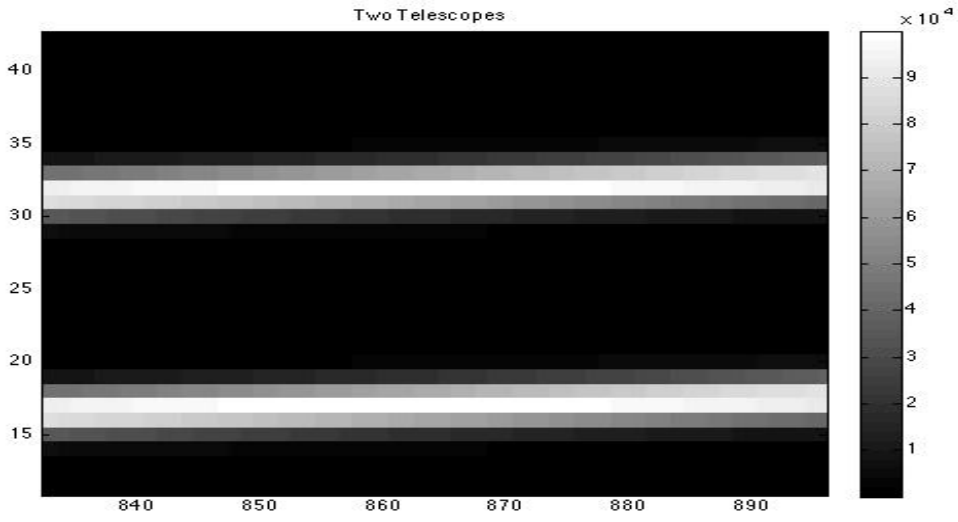

Figure 1: A single order of a stellar spectra, simulated for two telescopes; the bar along the right indicates intensity, while the axes indicate pixel values on the detector

Finishing the Spectra

The leap from one order to thirteen is not as great as that from none to one; however, there were some difficulties in determining the distance between each order (a result of the cross dispersion of the incoming light through the prism in our optics). Firstly, the distance increases as wavelength increases, meaning higher orders (orders laid out closer to the top of the detector) ought to be farther apart than lower orders. Secondly, the orders could not run onto one another; the separation on the detector had to be enough so that the two separate curves of each telescope did not blur into the other telescope's concurrent order. Lastly, the light from the highest orders could not run off the detector, and if it did there had to be some safeguard in place that would let us know that that had happened. The final result can be seen below:

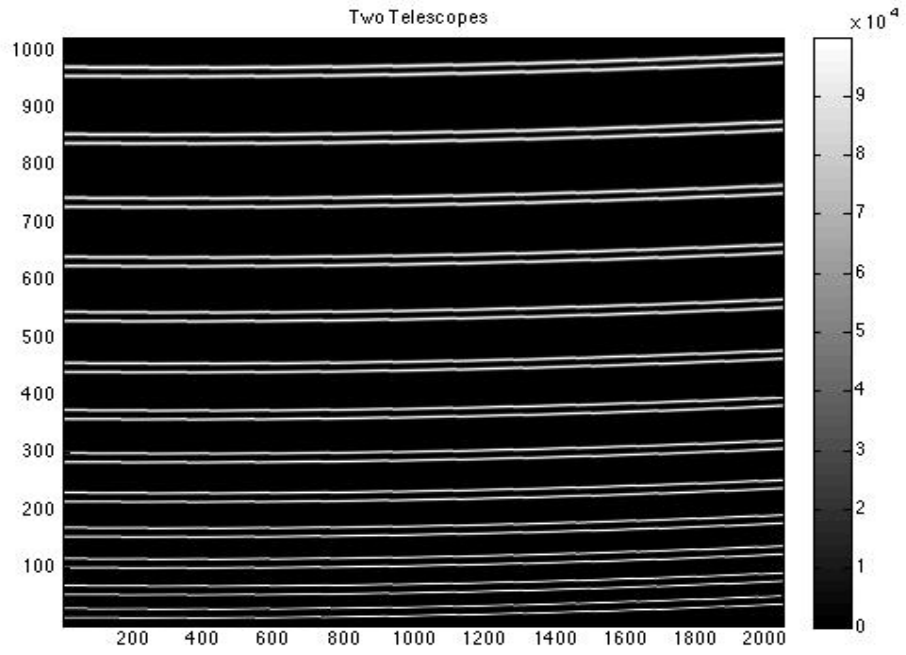

Figure 2: An entire spectrum, with all thirteen simulated orders laid out on the detector. The bar on the right and axes correspond to their counterparts in figure 1

Rotation, Truncation, and Faulty Pixels

With the basic stellar spectra finished, I set out to simulate the various perturbations that the incoming light might undergo, in order that we might test each one individually or any permutation of perturbations against our radial extraction method.

The first and easiest of these perturbations was simply a rotation of the orders; almost all rotations would be slight and a result of the optics system of iLocater. The second minor perturbation is actually an extension of the entire reason there are thirteen orders rather than simply one: cross dispersion through a prism. The light travelling through our detector gets dispersed via a prism, and apart from getting separated vertically it also ends up truncated as a result of the differing wavelengths of the incoming light. As such, the orders get truncated in the horizontal axes in a predictable upside down "v" shape, with precise parameters dependent on the optics of the instrument.

Finally, the detector will inevitably have pixels that are faulty in one direction or the other; pixels that always register a very low intensity are known as "dead" pixels, while pixels that always register a very high intensity are known as "hot" pixels. These are randomly dispersed throughout the detector, and it is essential that our extraction method be able to distinguish these from normal pixels. The result of these perturbations can be seen in the figure below:

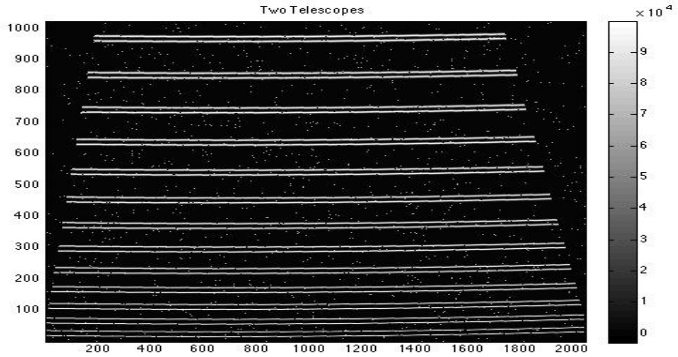

Figure 3: Spectral Orders with Slight Rotation, Truncation, and Faulty Pixels

Gaussian Photon Noise

Though there is always more error checking to be done, the Gaussian Photon Noise spread across the detector was the last major perturbation to be added to the simulation. The majority of noise is simply unavoidable known flux of photons in the collection process, and is spread across the detector pseudo randomly according to various distribution functions dependent upon the source of the noise. A Gaussian distribution (one generated by a Gaussian function, the same function used to determine light intensity within and around an order curve) can be seen below:

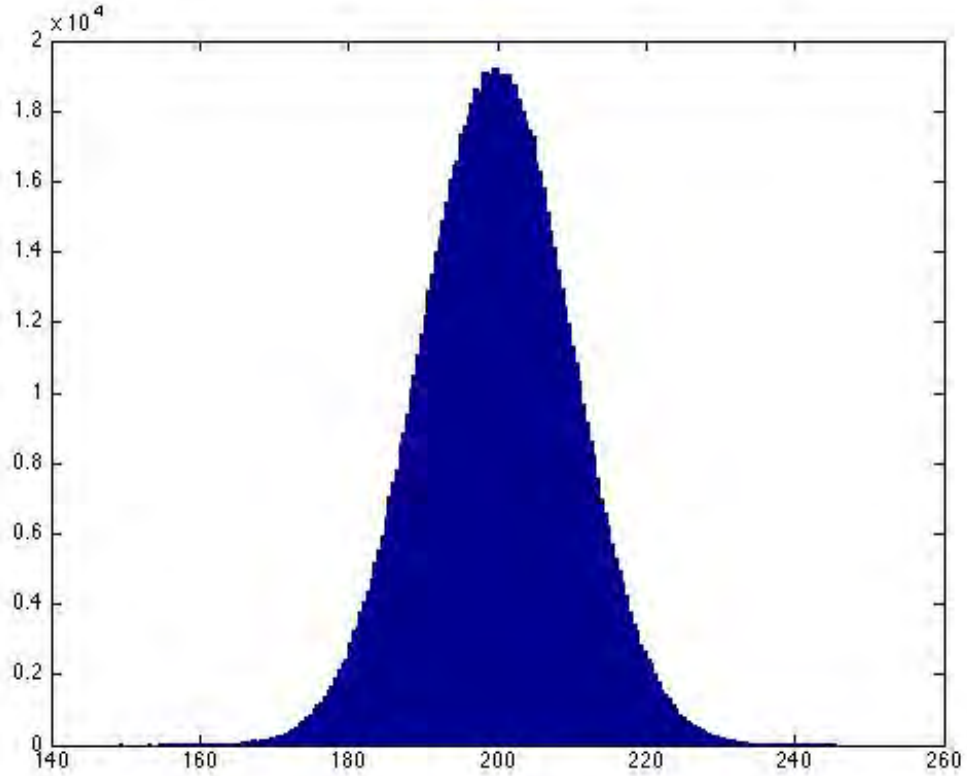

Figure 4: A Gaussian Distribution centered around 200, with full width half max of 20

In other words, as a result of two different perturbations known as "Photon Noise" and "Dark Current", each with Gaussian distributions, every pixel on the detector is affected with some additional intensity that must be taken into account for any simulation. When amalgamated, the figure below demonstrates the final

result:

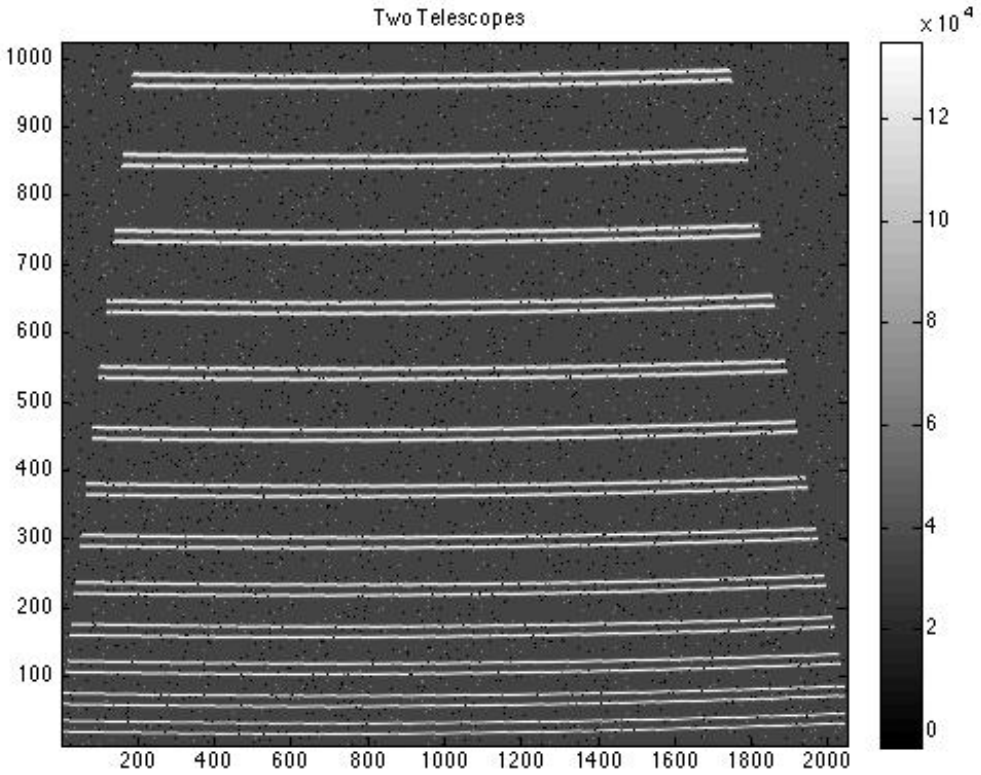

Figure 5: With Photon Noise and Dark Current Included

Coding Efficiency

In order to simulate an entire survey, the program that creates the above figure (Figure 5) has to be run about a thousand times. This means that, if the code works inefficiently and takes too long to compile, the run time will make it useless in a practical sense. This is why, rather than coding each image pixel by pixel, the code I have written instead utilizes Matlab's standardization of treating all objects as matrices to instead treat each image as a series of rows having operations done on each one in entirety, and then stacking them on top of one another. The result of this is that rather than having to run nested loops that require millions of calls, the program instead simply has to run down the vertical axis once, thus decreasing the order of magnitude of the number of calls required from the computer from the

millions to the thousands. This enables the code to run in as little as ninety seconds on a native computer or far less on a supercomputer, meaning that the longest required period of time to run the code would be just over a day, rather than perhaps months. Without this technique, though interesting for individual cases, it is unlikely that these simulations would serve much of a practical use.

Acknowledgements:

I would like to thank Professor Justin Crepp for his mentorship and guidance throughout this previous year and going forward. If you were not so understanding, patient, and knowledgeable I know that I never could have accomplished what I have. I would also like to thank the Notre Dame REU program run by Professor Garg for a wonderful experience being a member of the Contingency Group this summer. Finally, I would like to thank the Glynn Family Honors Program for helping make this project a reality.

References:

1. *Planet Occurrence Within 0.25 AU of Solar-Type Stars from Kepler*, Andrew Howard, *The Astrophysical Journal Supplement Series, 201:15 (20pp), 2012 August.*

2. http://kepler.nasa.gov/.

3. *iLocater Proposal*, Justin Crepp, 1-9.

Mathematical Modeling of Dynamic Instability in Microtubules

Christine Lucille Kuryla

2013 NSF/REU Program

Department of Physics, University of Notre Dame

Advisors: Mark Alber, Dept. of Applied and Computational Mathematics and Statistics

Holly Goodson, Dept. of Chemistry and Biochemistry

Abstract

Microtubules are biological polymers that have many functions in cells, such as support and structure in the cytoskeleton, providing avenues and mechanisms for intracellular transportation, and separating chromatids during cell division. Microtubule dynamic instability is an integral part of cell functioning, enabling microtubules to rapidly find and change spatial arrangements and interact with necessary biological components. Due to dynamic instability, microtubule ends switch randomly between phases of growth and depolymerization (subunits are being constantly added and removed from the ends of the various microtubules). The mechanisms of dynamic instability are not well understood, partially due to the complexity of microtubule structure. Experiments have shown that microtubules do not exhibit behavior consistent with the classical model of equilibrium polymer dynamics. Mathematical and computational models have been created to explore and better understand the phenomenon of dynamic instability. A coarse-grained stochastic model of a system of microtubules from Gregoretti et al. (JCS 2006) had previously been extended to simulate free microtubules in solution. To improve the model and make it more biologically realistic, a Monte Carlo algorithm was implemented that allows new microtubules to spontaneously form (nucleate) from the free subunits in the solution. Additional statistical output and analysis was also added to facilitate the investigation of the microtubule behavior. This enables the exploration of the effect of the ease of nucleation on the behavior of the system. The simulations will be compared with experimental results to attempt to better understand dynamic instability. The refinement of the understanding of dynamic instability has implications for the development of cancer treatments and the study of self-organized systems.

Introduction

To reduce the complexity of studying biological systems in vivo, it is helpful to breakdown the system into smaller pieces, study the smaller pieces, and then put them back together to understand the big picture. In vitro methods are used in order to have controlled environments that remove many external confounding variables and allow the investigation of the pieces of the system or biological processes. Theoretical or mathematical models of biological processes are used in silico to perform simulation "experiments" to gain deeper conceptual and quantitative (even predictable) understandings about processes. In silico simulations can also enable the study of experiments that are impossible or very difficult to perform in a lab, and they can bridge the gap between in vivo and in vitro. Here, microtubules and dynamic instability will be explored using methods in silico to complement those in vitro, and eventually in vivo.

Microtubules are non-covalent biological polymers found inside cells and are essential for many cellular processes. A polymer is a large molecule made up of repeated subunits; microtubules are composed of tubulin hetero-dimer subunits. Microtubules are part of the dynamic cytoskeleton (along with actin and intermediate filaments) which provides structure to the cell as a whole and a framework to keep organelles in place, establishes and maintains cell polarity, and forms structures such as flagella and cilia (Alberts et al. 2002). They are also involved in intracellular transportation, moving organelles and secretory vesicles that require active transport and functioning as "railroad tracks" for motor proteins such as dyneins and kinesins to facilitate the intracellular transport of substances. Microtubules are also involved in cell division, particularly in separating chromatids during mitosis and meiosis. The microtubule network is commonly referred to as the "microtubule cytoskeleton." The microtubule cytoskeleton is not a static network; it is highly dynamic and constantly changing. This allows for rapid rearrangement and response to changing stimuli.

Due to dynamic instability, microtubule ends switch randomly between phases of growth and

shortening (subunits are being constantly added and removed from the ends of the various microtubules). Polymerization is when subunits (tubulin) are added to the polymer (microtubule) causing it to grow or lengthen, and depolymerization is when subunits are removed causing the polymer to shrink or shorten. The change from microtubule growth to shortening is called catastrophe, and the complementary change from depolymerization to polymerization is called rescue (Alberts et al. 2002). Microtubule dynamic instability is an integral part of cell functioning, with the stochastic nature of the cycles switching from polymerization to catastrophe to depolymerization to rescue enabling microtubules to explore the space around them and rapidly find and change spatial arrangements and interact with necessary biological components. Due to dynamic instability, microtubules can quickly react to stimuli and change the shape or structure of the cell, and they can also find, reach, and actively transport cellular components such as organelles and chromosomes when needed (Desai et al. 1997).

Exploring Dynamic Instability

The mechanisms of dynamic instability are not well understood, partially due to the complexity of microtubule structure. The stochastic alternation between polymerization and depolymerization (dynamic instability) has been seen in microtubules both in vivo and in vitro. Experiments have shown that microtubules do not exhibit behavior consistent with the classical model of equilibrium polymer dynamics. This is because microtubules and actin are steady-state polymers since energy is used in the polymerization process. Textbooks either ignore this or oversimplify it. This gap in knowledge motivates the attempt to understand dynamic instability with mathematical models and computational techniques.

Mathematical and computational models have been created to explore and better understand the phenomenon of dynamic instability. A coarse-grained stochastic model of a system of microtubules from Gregoretti et al. (JCS 2006) was developed as a mesoscopic model of microtubules. In reality,

microtubules are hollow cylinders made up of linear protofilaments (polymers of alpha-beta tubulin hetero-dimers). For the purposes of this model, the microtubule is treated as a linear polymer (like a pearl necklace) with subunits of "tubulin." The subunits (tubulin) can be free in solution or part of a polymer (microtubule). They can be in a GDP state (unstable, more likely to depolymerize the end) or a GTP state (stabilizes the microtubule end). In this model, the microtubule polymers compete for the free tubulin subunits in solution, and several dynamic instability properties and parameters emerge on their own as properties of the active system.

In the Gregoretti model, the microtubules are fixed on one end. While this is often the case in vivo, it does not completely describe the entirety of microtubules and dynamic instability. The situation in vivo is very complex, and it is much harder to perform experiments in this manner, so it is helpful to simulate a simplified version that could exist in vitro. In order to begin to better understand the mechanisms of dynamic instability, the model was recently modified by a Notre Dame graduate student, Chunlei Li. In the modified version, the microtubules are able to polymerize and depolymerize on both ends, and the polymerization occurs at different rates for the different ends. This is observed in free microtubules in vivo and in vitro. Sometimes this leads to a behavior known as tread-milling, which is when one end grows and the other one shrinks. This can be seen as an in silico description of an in vitro situation to potentially make it easier to compare to experiment. This modification can simulate an in vitro situation; it is like separating out the microtubules and putting them in a test tube. Although in vivo microtubules are usually stable at one end, tread-milling and free microtubules do exist in cells. The simulation also makes frames of the microtubule system so that the behavior of the system can be visualized in a movie. One of this model's purposes was to examine dynamic instability and microtubule behavior in a simplified environment to eventually compare it to in vitro experiments.

Model Limitations and Subsequent Improvements

In Li's modified version of the model, microtubules could depolymerize to the point where they would just disappear. However, there was no possibility for the spontaneous formation of new microtubules from the free tubulin subunits in the solution (nucleation). The microtubules would eventually depolymerize (particularly in situations with low tubulin concentration) and monotonically decrease in number since they couldn't nucleate. In situations with high tubulin concentration, the fixed number of microtubules would just grow in length, but not in number. Eventually in both cases, due to the stochastic nature of the simulation, some microtubules would completely depolymerize and disappear, no matter how improbable. Omitting nucleation is an over simplification that compromises the biological accuracy of the model. This is particularly unrealistic because if a microtubule completely depolymerizes, it causes tubulin subunits to be released into the solution, which in turn increases the free tubulin subunit concentration. This elevated free tubulin concentration should increase the likelihood of nucleation, in this model's case, however, it just increased the chance of growth for the other microtubules.

The possibility for new microtubules to nucleate was added into the model, which enabled a fluctuation of the number of microtubules instead of a monotonically decreasing number of microtubules. The fluctuation is more realistic, and in reality, microtubules have been seen to nucleate, so the addition of nucleation caused the model to make more physical sense. No one has yet studied the effect of nucleation on the behavior of this system, so this was a good addition. A particular interest is to explore is the effect of the ease of nucleation on the critical concentration dynamics (basically the concentration where subunits start to polymerize into microtubules).

The nucleation was implemented using variation of a Monte Carlo algorithm to make it more biologically realistic and reflect the randomness observed in vivo and in vitro. The nucleation is governed by a known mathematical biochemical relationship that relates the frequency of nucleation to

the concentration of free tubulin subunits in the solution.

Nucleation frequency = $\lambda = A * [\text{free tubulin}]^b$

Where A and b are constants that are user adjustable parameters and [free tubulin] is the concentration of the free tubulin subunits in the solution. The frequency is then incorporated using a Poisson process (Markov Chain Monte Carlo characterized by a Poisson distribution) to calculate the probability of nucleation for each time step in the Markov Chain and determine whether or not to nucleate.

Probability of a nucleation event (at time t) = $F(t) = 1 - e^{-\lambda t}$

F(t) is the exponential cumulative probability function and t is time. Markov Chain Monte Carlo (MCMC) is often used in biological modeling and simulations and is memoryless and stochastic. Memoryless means that future states of the system are only dependent on the present state so are independent of all other past states, so that the state at time t_{i+1} is only dependent on the state at time t_i (so if a nucleation event occurred recently, it doesn't affect the probability of a nucleation event occurring again). MCMC is useful because of the stochastic nature, which agrees with the nondeterministic and somewhat random behavior of biological systems. A Markov Process usually models long times as successive small discrete time steps and is memoryless. A Markov Chain is the collection of these time steps. The probability of nucleation F(t) at each time step is calculated with λ at each time step (which is calculated with [free tubulin] at each time step). The resulting probability is incorporated at each time step to determine whether a nucleation event occurs to form new microtubules.

Additional statistical output was also added to the simulation to investigate different aspects of microtubule system behavior under different conditions. This will help to further analyze the data and gather more insight from the simulations (and possibly discover phenomena or patterns that were not thought of or observed before). It also makes it easier to compare the simulation results to experiments and to design experiments. The output per time step included [free tubulin] (the concentration of free

tubulin in solution), [polymer] (the amount of tubulin that is part of a microtubule), the total number of microtubules in the system, the mean (average) microtubule length, the median microtubule length, and the standard deviation from the mean microtubule length. There are now many aspects to analyze. So far, the number of microtubules and median microtubule length have been particularly helpful in examining whether or not the simulations are biologically realistic, and what they mean.

The possibility of spatial constraints was also created, but is not currently being used in the present simulations because the current goal is to work with phenomena in vitro. However, this additional condition will be valuable later.

Future Work and Implications

The current model additions will enable the exploration of the effect of the ease of nucleation on the behavior of the system. Since microtubules do not behave like equilibrium polymers, the classic theory of microtubule behavior in solution as far as critical concentration goes does not agree with experiment. To look into an explanation, the parameter space of the simulation, particularly those governing the ease of nucleation, is currently being explored. The parameters will be varied and their effects on the behavior of the system will be analyzed, which may gain insight into the behavior of microtubules displaying dynamic instability and their behavior in regards to critical concentration, persistent growth, complete depolymerization, dynamic instability and the steady-state. The simulations will be compared with experimental results to attempt to better understand dynamic instability.

Refining the understanding of dynamic instability has implications for the study of self-organized systems as well as adding to the general biochemical body of knowledge. Additionally, understanding dynamic instability in microtubules could help with the development of cancer treatments.

Acknowledgements

Thank you very much to my advisors Holly Goodson and Mark Alber for their help, support, and guidance. I would also like to acknowledge Chunlei Li for his implementation and modification of the Gregoretti model to include polymerization and depolymerization at both ends of the microtubules, and thank him for his appreciated nonobligatory Skype sessions all the way from China with a stranger. I would also like to thank Shant Mahserejian and Amy Buchmann for their guidance and support. I would like to thank the University of Notre Dame REU programs, and the NSF for their funding.

References

Alberts B, Johnson A, Lewis J, Raff M, Roberts K, Walter P (2002). *Molecular Biology of the Cell*, 4th ed., New York: Garland Science.

Desai A, Mitchison TJ (1997). *Microtubule polymerization dynamics.* Annu Rev Cell Dev Biol 13, 83–117.

Gregoretti IV, Margolin G, Alber MS, Goodson HV (2006). *Insights into cytoskeletal behavior from computational modeling of dynamic microtubules in a cell-like environment.* J Cell Sci 119, 4781–4788.

Gregoretti IV (2007). *Modeling Microtubule Dynamic Instability*. PhD dissertation, University of Notre Dame. Ann Arbor: ProQuest/UMI. (Publication No. UMI 3299147.)

Goodson HV, Gregoretti IV (2010). *Using computational modeling to understand microtubule dynamics: A primer for cell biologists.* Methods Cell Biol. 95:175-88.

Lam, P. *MCMC Methods: Gibbs Sampling and the Metropolis-Hastings Algorithm* [PowerPoint slides]. Retrieved from http://www.people.fas.harvard.edu/~plam/teaching/methods/mcmc/mcmc_print.pdf

Umrigar, C. (2010). *Monte Carlo Methods* [PowerPoint slides]. Retrieved from http://pages.physics.cornell.edu/~sethna/teaching/ComputationalPhysics/LectureScans/CyrusMonteCarlo.pdf

Exploring the Growth Mechanisms of GaAs Nanowires Grown by MBE

Kevin Lee

2013 NSF/REU Program
Physics Department, University of Notre Dame

Advisor(s):
Rich Pimpinella
Prof. Jacek Furdyna
Prof. Margaret Dobrowolska
Prof. Xinyu Liu

Abstract

We have successfully grown GaAs nanowires by Molecular Beam Epitaxy. In this work, we investigate the principal growth mechanisms underlying nanowire growth by measuring the morphology of the nanowires and comparing them to a simple growth model. From this, we are able to make several conclusions. The results of the data show that Adatom Diffusion contributes more to the overall growth rate than Direct Impingement. We also discover that Adatom Diffusion causes a large variance in the lengths of nanowires with the same diameter. From this research, it is evident that in order to gain control of the growth of semiconducting nanowires, more research is required to study the effects of growth conditions on Adatom Diffusion.

I.Introduction

Research dedicated to understanding and controlling the growth of semiconducting nanowires has grown in interest for their potential to advance technology for application in next generation computing [1], ballistic photonic waveguides [2], and for interconnecting molecules for molecular computing [3]. To realize this potential, we have to be able to control their growth. In order for us to be able to that, understanding the growth mechanisms associated with nanowire growth is necessary.

II. Experimental Methods

In this study, GaAs nanowires are grown by using Molecular Beam Epitaxy (MBE) [4]. A GaAs substrate is loaded on the holder present inside the MBE chamber. The chamber itself is kept at high vacuum and surrounded by a shroud that is cooled by liquid nitrogen, which helps improve the vacuum. An effusion cell then deposits a layer of Au film on top of the substrate, which is then rotated and heated. As the sample is heated, the Au film absorbs Ga from the substrate and melts, forming eutectic Au-Ga droplets on top of the substrate. More effusion cells

fire beams containing Ga and As onto the substrate, causing a pillar of GaAs to grow underneath the droplet, which acts as a catalyst. This is done for a certain amount of time, which we refer to as the growth time. In this study, we looked at four GaAs nanowire samples that were grown using this procedure with different growth conditions (A table containing the specific growth conditions for each sample can be seen later in Table 2).

We proceeded to take images of our samples so that we measure the length and the diameter of the nanowires. We used a Scanning Electron Microscope (SEM) to take several images of our samples. From all the images, we chose a few for each sample that had nanowires that were easy to measure. This would allow us to obtain four sets of data containing the lengths and diameters of each nanowire in the image, which we could then proceed to analyze.

III. A Simple Growth Model

In order to analyze our data, we sought to derive a growth model to fit our data with. The two growth mechanisms that contribute to the growth of a nanowire are Direct Impingement and Adatom diffusion [5]. Direct Impingement refers to the material that arrives directly from the beam while Adatom diffusion refers to the material that arrives from the substrate by diffusing up the surface. Figure 1 gives a visual representation of a nanowire with length dL and a radius of R and how the two mechanisms contribute to its growth.

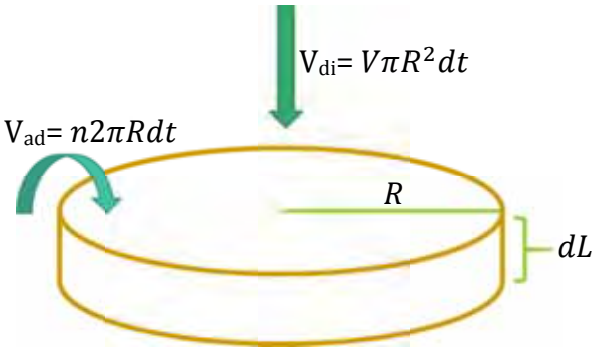

FIG. 1: Visual representation of the two mechanisms. Material from Direct Impingement comes directly from the beam while material from Adatom Diffusion diffuses upwards to the top of the nanowire.

The total volume of a given nanowire could then be seen as the sum of the amount of material that arrived from Direct Impingement and the amount of material that arrived from Adatom Diffusion. This allows us to set up Equation 1, the volume of a nanowire at a given time:

$$\pi R^2 dL = V\pi R^2 dt + n2\pi R dt \quad (1)$$

where $\pi R^2 dL$ is the volume of a nanowire with length dL and a radius of R, $V\pi R^2 dt$ is the amount of material that arrives from Direct Impingement, and $n2\pi R dt$ is the amount of material that arrives from Adatom Diffusion. V is defined as the rate of the material arriving from the beam. Since the beam hits the whole cross-sectional area of the nanowire, V is multiplied by the cross-sectional area. n is defined as the rate of diffusion up along the nanowire. Here, we assume that the material diffuses straight up along the surface without spiraling around the nanowire and arrives at the top. Since this is occurring from around the whole surface, we subsequently multiply n by the circumference of the cross-section.

We see that we can divide all terms in Equation 1 by πR^2, which gives us Equation 2:

$$dL = Vdt + \frac{2n}{R} dt \quad (2)$$

Dividing all terms by dt gives us Equation 3, which now shows the rate of change of the length of a nanowire, defined by the rate of Direct Impingement and the rate of Adatom Diffusion.

$$\frac{dL}{dt} = V + \frac{2n}{R} \quad (3)$$

We continue to integrate with respect to t, which leads us to Equation 4:

$$L = Vt + \frac{2}{R}\int_0^t n(t)dt \quad (4)$$

where L is the length of a nanowire and t is the growth time. Here, we assume that n varies with time, so we leave it as $\int_0^t n(t)dt$ because we do not know exactly what kind of function n is. That assumption is not necessary for V because the design of the MBE ensures a uniform distribution of the beam across the cross-sectional area and a constant rate. If we divide all terms by t, we can define an equation for the average growth rate of a nanowire, seen in Equation 5:

$$\mathcal{L} = V + \frac{2}{R}\left[\frac{1}{t}\int_0^t n(t)dt\right] \tag{5}$$

where $\mathcal{L}$ is the average growth rate. We can see that $\left[\frac{1}{t}\int_0^t n(t)dt\right]$ is now just the average value of n, allowing us to bypass the uncertainty of what kind function n is, in respect to time. At this point, we also decide to define $\mathcal{L}$ in terms of the diameter, D, rather than radius, R, because we realized that we can make more accurate measurements of the diameter than the radius when we look at the images of the sample. Making all the necessary adjustments, we finally arrive at Equation 6, our growth model:

$$\mathcal{L} = V + \frac{4\bar{n}}{D} \tag{6}$$

where $\bar{n}$ is simply the time averaged value of n. V is the contribution from Direct Impingement (which we refer to as V_{di} later) to the average growth rate while $\frac{4\bar{n}}{D}$ is the contribution from Adatom Diffusion to the average growth rate (referred to as V_{ad} later). We aim to use this growth model to fit experimental data so as to gain insight into the two growth mechanisms.

III. Results

We tested our growth model with our four nanowire samples. Figure 2 shows SEM images of the four samples. We obtained our data by measuring the length and diameter of each

nanowire (whenever it was possible) by looking at the SEM image and using the scale bar present at the lower right corner of each image.

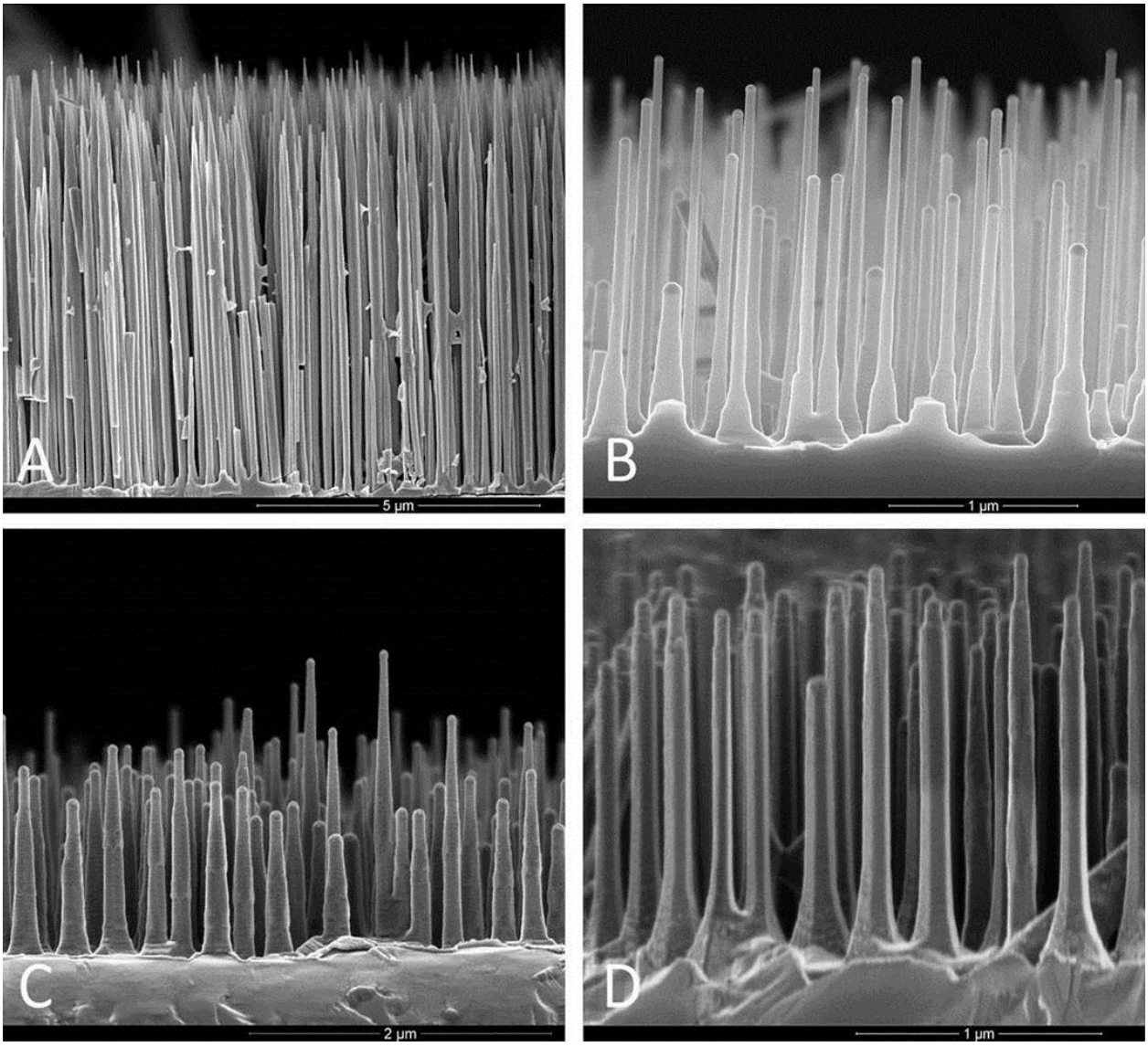

FIG. 2: SEM images of the four samples that we analyzed. A scale bar present at the lower right hand corner allows us to obtain accurate measurements of the nanowires.

Initially, when we plotted our data, we discovered that there was a huge variance in the length for nanowires that had the same diameter. In order to overcome this variance, we decided to group nanowires with the same diameter and average their lengths to obtain one data point. We fit our data with our growth model and calculated r-squared values to see how well our

model fitted the data. Figure 3 shows the data for all four samples and the fit for that data of our growth model. The r-squared values show that for all four samples, our growth model is in good agreement with the data. This allows us to establish a general rule that thinner nanowires tend to be taller while thicker nanowires tend to be shorter. As mentioned before, since the design of the MBE beam allows a uniform flux across the whole sample at a constant rate, we can conclude that the error between our actual data and the fit comes from a varying rate of Adatom Diffusion, which supports our assumption from earlier that n, the rate of material that arrives by diffusion from the substrate, varies with time.

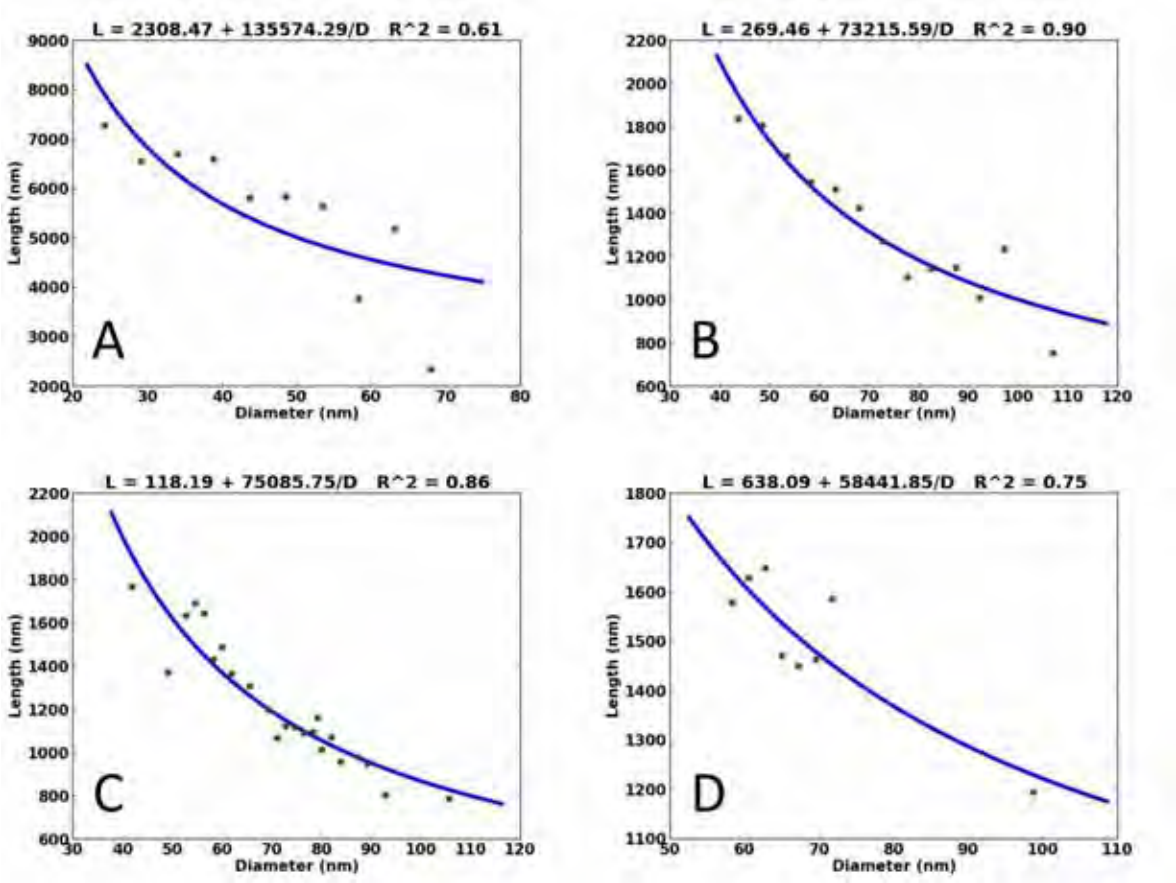

FIG. 3: Each graph corresponds to the SEM image in Figure 2 by letter. Each point on the graph is an average length for a group of nanowires with the same diameter.

From our fits, we were able to calculate V_{di} and V_{ad}. Table 1 shows these values for each sample along with its corresponding r-squared value and its average growth rate ($\mathcal{L}$). For all of

our samples, we can see that Adatom Diffusion (V_{ad}) contributes more to the average growth rate than Direct Impingement (V_{di}). We can also see that an increase in the beam flux, which increases V_{di}, does not change the fact Adatom Diffusion still makes the bigger contribution.

Sample	R^2	V_{di} (nm/min)	V_{ad} (nm/min)	calc. $\mathcal{L}$ (nm/min)	mean $\mathcal{L}$ (nm/min)
A	0.61	9.62	13.58	23.20	23.20
B	0.90	1.11	4.41	5.52	5.52
C	0.86	0.49	4.60	5.09	5.09
D	0.75	2.66	3.60	6.26	6.26

Table 1: V_{di} and V_{ad} calculated for the four samples

Although we can say with certainty that Adatom Diffusion makes a bigger contribution, there are still questions that remain. Table 2 shows the growth conditions for the four samples. We can see that the growth conditions for Sample A were noticeably different, so it makes sense that Sample A had a noticeably different V_{di} and V_{ad}. The table also shows that Samples B, C, and D had similargrowth conditions (Samples C and D even had identical conditions). However, there was a significant difference in V_{di} and V_{ad} between the three samples. This indicates that there are other factors that play a role in growth. One such factor that we suspect contributes to the growth rate is the spatial distribution of the nanowires.

Sample	T (Substrate) (ºC)	T (Ga) (ºC)	T (As) (ºC)	Growth Time (min)
A	570	940	375/1000 V=1.6	240
B	590	860	375/1000 V=2.0	243
C	600	870	375/1000 V=2.0	240
D	600	870	375/1000 V=2.0	240

Table 2: Growth conditions of the four samples

These questions that still remain about the growth mechanisms are evident in this fifth sample we looked at. Figure 4 shows us an SEM image of Sample E. Here, we notice a few interesting things about the image. For example, in each of the circled areas, which show two neighboring nanowires, the thicker nanowire is a lot taller than the thinner wire, seemingly breaking the general rule we were able to establish earlier. This feature can be observed across the whole image (the reason the circled areas were specified was to allow for a direct side-to-side comparison). We believe that the reason that some of these nanowires didn't follow the general rule was that they were stealing material from each other due to their relative closeness to each other through the Adatom Diffusion mechanism. This would also explain why there was a huge variance in length among nanowires with the same diameter.

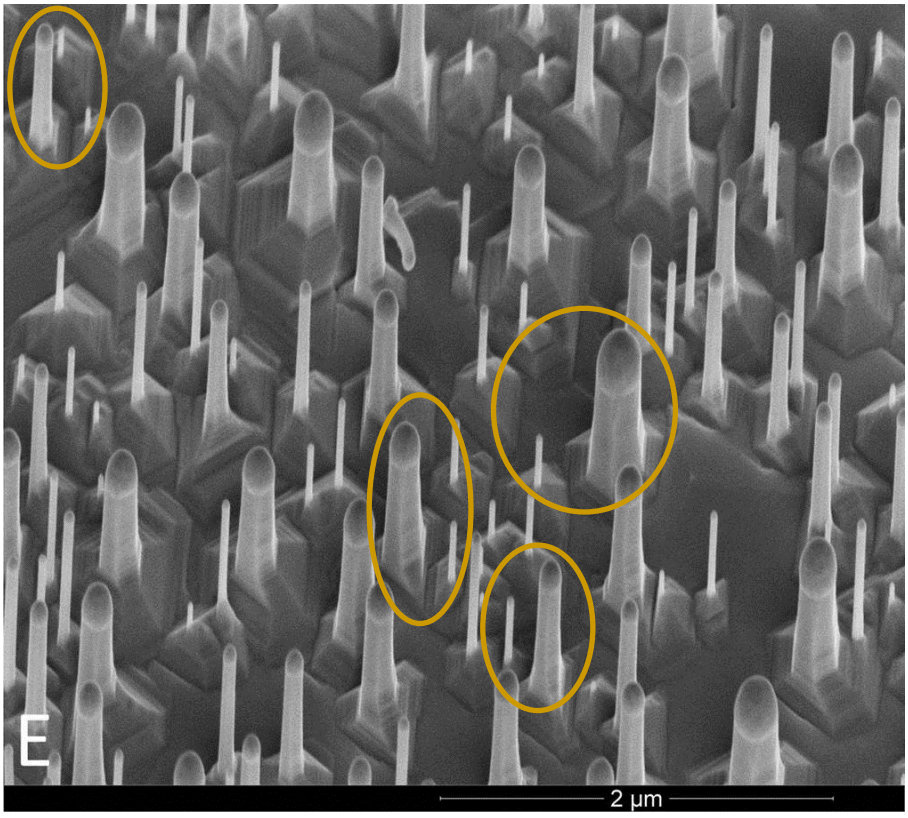

FIG. 4: SEM image of Sample E. Notice that in the circled areas, the thicker nanowire is taller than the thinner nanowire.

IV. Conclusion

Through this study, we have discovered that Adatom Diffusion contributes more to the growth rate of a nanowire than Direct Impingement. We have also found that there is a large variance in the diffusion rates between nanowires caused by variations in spatial distribution. The variance in spatial distribution leads to variance in Adatom Diffusion rates, ultimately causing a huge variance in lengths among nanowires with the same diameter. This tells us that in order to have control over the growth of nanowires, we need to have control over Adatom Diffusion. Based on our observations, in future studies we would like to investigate the effects of spatial distribution on the Adatom Diffusion rate.

Acknowledgements

I would like to thank the National Science Foundation and the University of Notre Dame Department of Physics for providing funding for the REU program. I would also like to thank Dr. Umesh Garg for coordinating the REU program and providing me the opportunity to participate in it this summer. Thank you to my advisors, Dr. Jacek Furdyna, Dr. Margaret Dobrowolska, and Dr. Xinyu Liu, for providing me the opportunity to join their research group. Many thanks to my grad student advisor, Rich Pimpinella, for working with me for the whole duration of the REU program and teaching me the things I needed to know to be able to do this research.

References

[1] M. H. Huang, S. Mao, H. Feick, H. Yan, Y. Wu, H. Kind, E. Weber, R. Russo, and P. Yang, Science**292**, 1897, (2001).

[2]W.H.P. Pernice1,C. Schuck1, O. Minaeva, M. Li, G.N. Goltsman, A.V. Sergienko, and H.X. Tang, Nat. Commun. **3**, 1325, (2012).

[3] H. Yan, S. H. Park, G. Finkelstein, J. H. Reif, T. H. LaBean, Science 301, 1882 (2003).

[4] M. T. Bjork, B. J. Ohlsson, T. Sass, A. I. Persson, C. Thelander, M. H. Magnusson, K. Deppert,L. R. Wallenberg, and L. Samuelson, Appl. Phys. Lett. **80**, 1058 (2002).

[5] V. G. Dubrovskii, N. V. Sibirev, G. E. Cirlin, J. C. Harmand, and V. M. Ustinov, Phys. Rev. E **73**, 021603 (2006).

Electronic Properties of Lead Telluride Quantum Wells

Liza Mulder
Smith College

2013 NSF/REU Program
Physics Department, University of Notre Dame

Advisors: Profs. Jacek Furdyna, Malgorzata Dobrowolska, and Xinyu Liu
Thanks also to: Rich Pimpinella, Joseph Hagmann, and Xiang Li

Abstract

My research this summer has focused on measuring the electronic properties of quantum wells that combine two families of semiconductors, specifically Cadmium Telluride and Lead Telluride (CdTe/PbTe/CdTe), whose interfaces hold promise of Topological Crystalline Insulator (TCI) surface states. The samples used in my study are grown by Molecular Beam Epitaxy, and measured using Magneto Transport experiments. I have found that samples grown on higher temperature substrates have higher charge carrier mobilities and lower carrier concentrations, while the resistivity shows no significant change. These results will be used as a guide toward designing future structures for observing and characterizing TCI surface states.

Introduction

Semiconductors have many applications in electronic devices, and as these devices become smaller and smaller, so do their components. Hence the importance of understanding the complex surface states of semiconductors. Some of these surfaces are also possible examples of Topological Insulators (TIs) or Topological Crystalline Insulators (TCIs). By studying semiconductors in the form of thin films, quantum wells, nanowires, and quantum dots, researchers hope to better understand semiconductors in this form, to measure the electronic and magnetic properties of their surface states, and to discover new examples of TIs and TCIs. This summer I studied the electronic properties of Cadmium Telluride - Lead Telluride (CdTe/PbTe:Bi/CdTe) quantum well structures. The samples are grown by Molecular Beam Epitaxy, and measured using Magneto Transport. This paper focuses on the effects of differences in substrate temperature during growth on the resistivity, mobility, and carrier concentration of the quantum wells. Higher substrate temperature results in higher mobility, lower carrier concentration, and no significant change in resistivity.

Theoretical Background

Properties of Lead Telluride (PbTe)

Lead Telluride (PbTe) is a compound of the elements lead and tellurium. It forms in a rock-salt face-centered cubic crystal structure with ionic bonds. PbTe is a IV-VI narrow-gap semiconductor in the bulk.[7] This research compares the electrical properties of PbTe quantum wells (doped with Bi and sandwiched between CdTe layers) obtained with different growth conditions, and specifically using different substrate temperatures.

Topological Insulators and Topological Crystalline Insulators

Topological Insulators were predicted in 2005 and first confirmed experimentally in 2007.[6] The name refers to insulators which have a conducting surface state. TI band structure will show an energy gap between the valence and conduction bands, but will also have a thin surface or pathway connecting the two at certain points (this is the conducting surface state). On a 3-dimensional model of the band structure, the conducting surface looks like two cones in momentum space joined at their apices. The cones are called Dirac cones, and the point where they meet is the Dirac point. This contact/crossing of the valence and conduction bands is a consequence of the interface between a semiconductor and vacuum, or between two semiconductors. The theory is complex, but most basically, the different topologies on either side of the interface require some sort of crossing or contact to switch between them. For a TCI, the crystal structure of certain faces contributes to this state, and it exists on some faces but not others.[2, 4-6]

Electrons flow along the conducting surfaces via the Quantum Spin Hall Effect (QSHE). The charges split up according to their spin, and move only in the direction perpendicular to that spin. They thus form four "traffic lanes," one for each direction on two edges of the surface. When the electrons are flowing in their "lanes," their motion is locked to their spin. Therefore, even if they hit an impurity, they cannot change direction, and so they go around it. This greatly reduces scattering in the material, which means conduction on TIs and TCIs is significantly more efficient.[2, 4-6]

Because of the inherent dependence of these effects on spin, TIs and TCIs have potential applications in spintronics, and especially for quantum computing.[5]

Fabrication of PbTe

Molecular Beam Epitaxy

We fabricate our samples using a Molecular Beam Epitaxy (MBE) machine. The MBE allows us to grow very specific compounds with certain ratios of elements, one atomic layer at a time. The sample grows on a substrate, which is inside an ultra-high vacuum chamber. The vacuum keeps the space inside the chamber free of stray atoms which could contaminate the growth. Heaters in the MBE machine heat elemental sources until the elements are in gaseous form. The elements are then released into the chamber by opening and closing shutters in appropriate amounts, as needed. The beams of particles are all aimed at the substrate target. A Reflection High-Energy Electron Diffraction (RHEED) gun allows an observer to monitor the growth of the sample by checking the flatness of the surface being grown.

For the present growth of the (CdTe/PbTe:Bi/CdTe) quantum well structures, the growth times and temperatures of all the elements were the same for each sample, with only the substrate temperature varying. If the substrate temperature is too low, the crystal will form an imperfect structure, with surface imperfections which change the electronic structure and impede conduction. If the substrate temperature is too high, the layers will diffuse into each other, blurring the boundaries which keep the electrons inside the quantum well. Theoretically, the samples yield the best data (with better conduction and lower background noise) at some temperature between these two extremes.

Growing PbTe on CdTe

As shown in figure 1, the samples consist of a Lead Telluride (PbTe) quantum well doped with Bi, between two thicker layers of Cadmium Telluride (CdTe), all on a substrate of Gallium Arsenide (GaAs). PbTe and CdTe have similar lattice constants (less than 1% mismatch) and similar structures (they are both face centered cubic), so they can form covalent bonds at the interface. The PbTe and CdTe crystals both have polar and nonpolar faces. Of the five ways they can bond, one bonds between

the two non-polar surfaces, two between a polar and a nonpolar surface, and two bond between two polar surfaces.[3, 7]

Crystallographic Structure Diagram

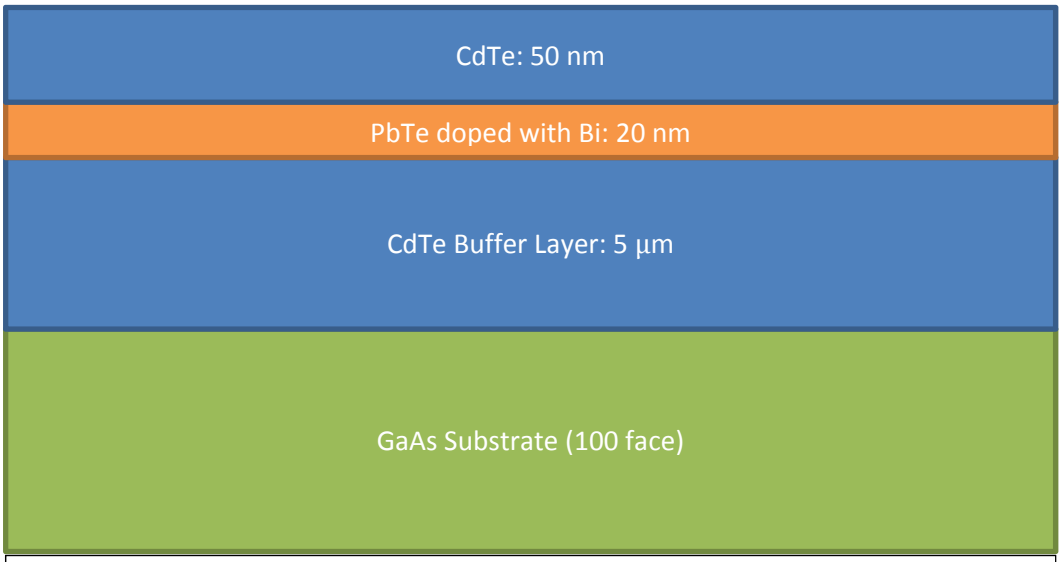

Figure 1: Diagram of sample structure. All samples were grown on a Gallium Arsenide wafer (100 face), followed by a Cadmium Telluride buffer layer 5 microns thick, then the Lead Telluride quantum well doped with Bismuth (20 nm), and finally a 50 nm layer of Cadmium Telluride.

Magneto-Transport

Method

Magneto-Transport measures the sheet resistance and hall resistance of the sample at varying magnetic field strengths and different temperatures from 300K to 16K. From the sheet resistance we can calculate the resistivity of the samples at different temperatures. From the hall resistance data, we can calculate carrier concentration and mobility, using the following equations. Charge Carrier Concentration $n = \frac{BI}{V_h de}$, where $\frac{BI}{V_h}$ is the inverse slope of the Hall Resistance versus Field plot, d is the thickness of the quantum well, and e is the charge of an election. Resistivity $\rho = RS/l$, where R is the sheet resistance, S is the product of the sample width and thickness d, and l is the sample length. Charge Carrier Mobility $\mu = 1/\rho ne$. Charge Carrier Type is determined by the sign of the slope of the

Hall Resistance versus Field plot: a negative slope indicates electrons, and a positive slope indicates holes.

Results

Carrier Concentration

Figure 2 shows the plot of carrier concentration versus substrate temperature during growth. We found a negative relationship between the substrate temperature during sample growth and the carrier concentration of the sample. Samples grown on a higher temperature substrate had lower carrier concentrations when measured at 30K (in blue), 20K (in green), and 16K (in orange). These data for all three temperatures agree very well, and show the same relationship.

The carrier type data was the same for nearly all the samples. The samples grown at the lowest temperature, 250C, sometimes produce positive charge carriers, and at other times negative charge carriers. All samples at higher temperatures, however, consistently had negative charge carriers.

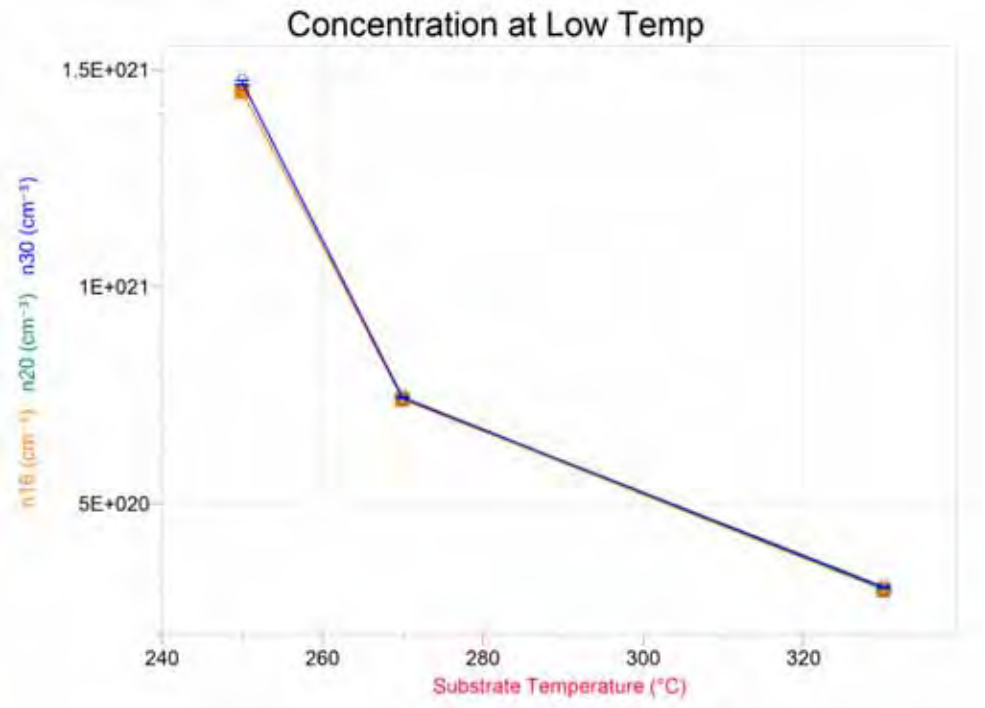

Figure 2: Plot of Carrier Concentration versus Substrate Temperature. Data taken at 30K (in blue), 20K (in green) and 16K (in orange).

Resistivity

Figure 3 shows the plot of sample resistivity versus substrate temperature. The data showed no significant difference in resistivity between samples grown at different substrate temperatures. The resistivities of the samples grown at different temperatures are all comparable to each other; the differences between the values are well within the error limits for each measurement.

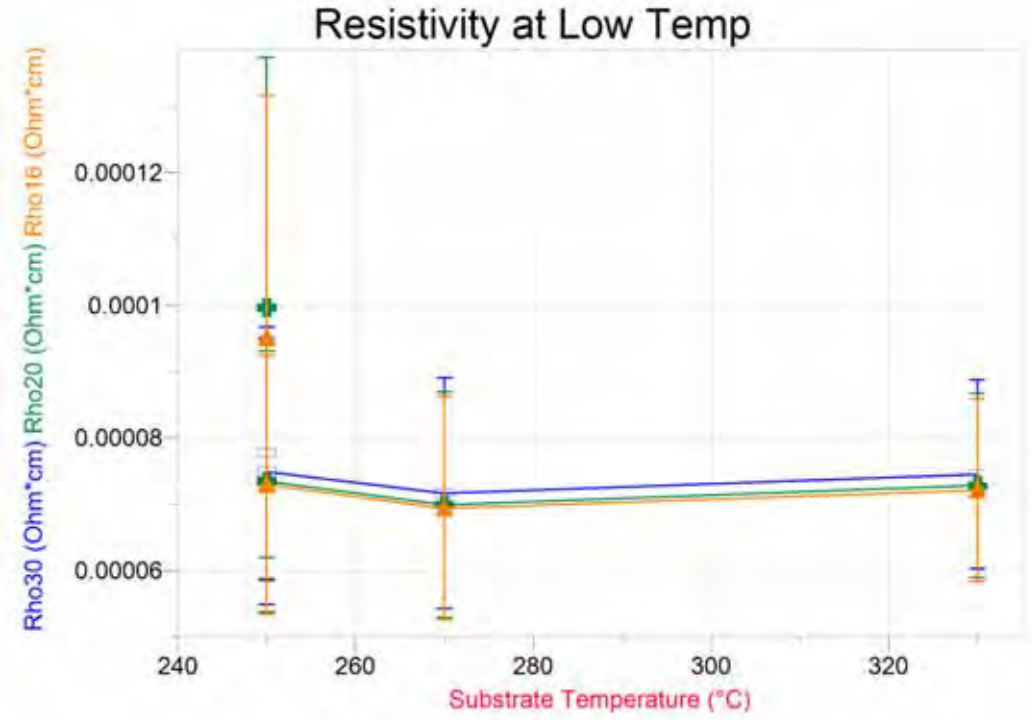

Figure 3: Plot of Resistivity versus Substrate Temperature. Data taken at 30K (in blue), 20K (in green) and 16K (in orange).

Charge Carrier Mobility

Figure 4 shows the plot of carrier mobility versus substrate temperature. We found a positive relationship between substrate temperature during sample growth and charge carrier mobility in the sample. The samples grown at higher substrate temperatures had higher charge carrier mobilities when measured at low temperature. The data taken at different temperatures agree well with each other, all showing the same trend.

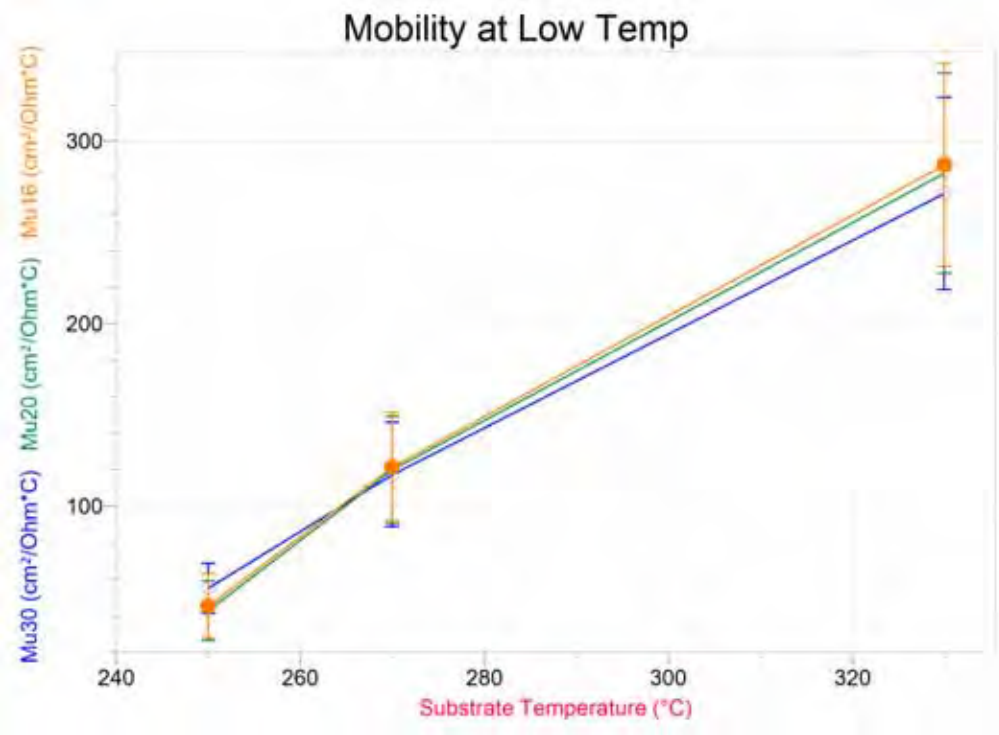

Figure 4: Plot of Carrier Mobility versus Substrate Temperature. Data taken at 30K (in blue), 20K (in green) and 16K (in orange).

Since the resistivity of all samples showed no significant differences, we suspect that the different substrate temperatures did not cause significant structural changes in the material which would impede conduction. Rather, it is likely that the higher carrier concentrations in the lower temperature samples led to the lower carrier mobility in those same samples. Carrier mobility is a measure of the mean free path of a carrier, namely, how far the carrier can travel before hitting an impurity or another carrier. When the density of charge carriers is higher, the mean free path is decreased because they bump into each other more often. In the same way, the higher temperature sample had a higher mobility because of its lower carrier concentration.

Conclusions

This research focused on determining the effects of differences in substrate temperature during growth on the properties of lead telluride quantum wells. The samples grown by molecular beam epitaxy consisted of lead telluride doped with bismuth, between two layers of cadmium telluride, all on

a substrate of gallium arsenide. From the Magneto-Transport study, we concluded that higher substrate temperatures result in lower charge carrier concentration, higher charge carrier mobility, and no significant difference in resistivity. The inverse relationship between carrier concentration (determined by substrate temperature) and carrier mobility indicates that lowering the carrier concentration increases the mean free path of the charge carriers, and thus their mobility.

This research revealed an important connection between substrate temperature, carrier concentration, and carrier mobility. Furthermore, the fact that the product of these values remains the same in all measurements, i.e., higher carrier concentrations lead to higher scattering rates, strongly suggests the scattering is dominated by carrier-carrier interaction; or, alternatively, that it is dominated by the scattering of the carriers on impurities responsible for generating carriers in PbTe. Since for every carrier there is a dopant or defect that produces it, the more carriers you have, the more ionized dopants they leave behind, and carriers can scatter on those. From this we can conclude that increasing the number of carriers alone is not sufficient for achieving lower resistivities.

This conclusion is an important insight into the properties of PbTe-base quantum structures, and provides more information about the optimal growth conditions for these structures. Continuing to fabricate better lead telluride quantum wells, and then using those quantum wells to look for topological insulator characteristics, is the next step for the research.

References

1. Bailey, David; van Driel, Henry; Harlow, Jason; Pitre, John; Yoon, Taek-Soon. University of Toronto (2011). Web. 11 July 2013.
2. Fu, Liang. *Physical Review Letters 106* (2011): 106802-1. Web. 13 June 2013.
3. Leitsmann, R; Ramos, L.E; Bechstedt, F. *Physical Review B 74* (2006): 5. Web. 4 June 2013.
4. Moore, Joel E. *Nature Vol. 464* (2010): 194-196. Web. 13 June 2013.
5. Moore, Joel E. *IEEE Spectrum.* 21 June 2011. Web. 13 June 2013.
6. Witze, Alexandra. *Science News: Physics on the Edge vol. 177 no. 11* (2010). Web. 13 June 2013.
7. M. Szot, L. Kowalczyk, E. Smajek, V. Domukhovski, J. DomagaÃla, E. ÃLusakowska, B. Taliashvili, P. Dziawa, W. Knoff, M. Wiater, T. Wojtowicz and T. Story. *Acta Physica Polonica A Vol. 114 No. 5* (2008). Web. 4 June 2013.

A Parametric Model of Galaxy Feedback Processes

María Jesús Muñoz López

2013 NURF/REU Program

Physics Department, University of Notre Dame

Advisor: Prof. Lara Arielle Phillips

Abstract

Filamentary structures forming the cosmic web have much higher density than the cosmic mean, and provide a continuous flow of matter into galaxies. In this cosmic web, inflow and outflow have been studied both observationally and through simulations to help explain galaxy evolution and metal enrichment in the filamentary environment. Parametric models have been used in the past to help account for the outflow from galaxies in large-scale simulations, but they do not take galaxy orientation, or differing feedback processes into account. In this new model, an attempt is made at identifying not only the amounts of matter and energy feedback from a galaxy but also the direction it takes and thus where it flows over time. This will eventually lead to a better understanding of the distribution of enriched materials in the filamentary cosmic web.

Introduction

The current model used in large-scale simulations assumes a spherical inflow and outflow around a galaxy. However, observations and higher resolution simulations show that this is not the case. In fact, though the outflow mechanism governs which part of the galaxy the material is ejected from, feedback processes occur mostly in a direction perpendicular to the disk. This work looks at improving the

current model, to make it conform with our current understanding of the outflow picture. The parametric model we describe can be used in large scale simulations instead of the spherical outflow model.

Background

We first consider the different feedback mechanisms. Inside the cosmic web, halo density is about 10-14 times greater than the cosmic mean. Filaments are thicker and denser, and have higher temperature at clusters. In haloes with average growth rate of halo mass greater than the shock mass, a narrow dense dark matter filament feeds the halo, and the enhanced density makes flow unstoppable, as it cools down before getting enough pressure to be shock-heated [1]. Viscosity in the intracluster medium (ICM) is suggested to be around ν=0.07 [2], whereas in the galactic disc it is around ν=0.3 with maximum around 0.6 in marginally stable self-gravitating discs [3].

Inflow from galactic filaments to the galaxy is mainly via cold-mode accretion of gas from the IGM. Except for halo masses $M_{halo} << 10^{11} M_{\odot}$, it is relatively insensitive to feedback processes. As redshift decreases, the hot halo builds up, but cold accretion persists. Hot accretion increases in lower redshifts and higher mass haloes ($M_{halo} >> 10^{12} M_{\odot}$) depending on radiative cooling and outflows driven by supernovae (SNe) and active galactic nuclei (AGN) [4]. As the hot

halo condenses via thermal stability, high velocity clouds (HVC) are formed and move towards the disk. However, only the larger HVCs actually make it to the disk, whereas the rest become part of the warm ionized galactic medium [5].

The halo, from filamentary cold-mode accretion of gas that was never heated to shock temperature, contributes to the angular momentum of the disk. The low angular momentum gas is rapidly accreted and expelled early. Later accreted material has higher angular momentum and forms the disk. The angular momentum in the disk is higher outside the star-forming region. It then releases a wind that increases the halo mass. Cool clouds are also ejected from the disk onto the halo. In the star-forming disk, metal is ejected, thus enriching the halo, which then returns (sometimes more) gas to the disk [5]. The star-forming region has been observed to convert the input gas rapidly. The common cases show star formation rates of 100-200 $M\ yr^{-1}$ [6]. For both hot and cold accretion, inflow occurs at an angle of approximately 30-50 degrees at virial radius due to the high angular momentum of in-falling material [7].

Outflow from the galaxy is roughly perpendicular to it, and occurs in two different ways. In the lower mass end, outflow is predominantly SN driven. In higher masses, outflow is mainly driven by AGN winds [8]. At $10^{11-13}M$ there are virtually no escaping winds, since the two processes tend to suppress each other. The two processes are often seen to coeval, as SNe and AGN control how

much gas can condense into star forming galaxies and redistribute gas in a complex, non-linear way [9]. Outflow velocity increases as gas surface density increases, and decreases with increasing gas scale height. Feedback from SNe and AGN is thought to suppress star formation, lowering the baryon fraction in the galaxies. SN feed back is also thought to be responsible for metal enrichment of the intergalactic medium (IGM) [10].

In the case where the mass is very low and SNe outflows dominate, winds are ejected at v_{wind} less than about 1000kms^{-1} [8]. In case scenarios both like this and with AGN present, we distinguish between type II and type Ia supernovae. SNIa have masses of 3-16 M ([11]) and occur at a rate of 5.3±1.1x10^{-4} per year per unit stellar mass or 3.9±0.7x10^{-4} per M yr^{-1} of star formation [12], to match observations, 0.5 explosions per century would be required [13], with mass rate 2.3±0.6x10^{-3}yr^{-1}M $^{-1}$ [14]; for SNII, which occur about 4Myr after the star formed, we consider masses of 8-40 M . Winds coming from SNII carry a mass of approximately 10 M , at about 3000kms^{-1}, with some 10^{51} erg of energy [11], [15]. SN in great molecular clouds (GMC) with M_{GMC}=10$^{5-6}$ M , $t_{life,GMC}$=10-30Myr, and gas dispersion velocity of about 5-10kms^{-1}, release bubbles with radius of escape r=1.1-2 at an angle of 2arcos(1/r) [16]. SN events generate a hot gas cavity of radius <200pc and masses of around 10^{6} M , around them and eject metals which, depending on the number of events in the area, are transported as hot gas to the IGM or feed

star formation gas. 1000 SN events after an instantaneous burst of star formation suffice to almost entirely blow away the gas in the system, whereas 100 SN explosions would trigger the collapse of the protogalactic cloud, causing the formation of a cold, dense clump disk with metallicity $Z=4x10^{-4}Z$ [17]. As fountain gas loses angular momentum relative to the disk, if SN driven, it entrains hot halo material that it returns to the disk to feed star formation [5]. The limiting star density in the starburst is found empirically to be of order 10^{11} M kpc^2 [18].

AGN generate different kinds of outflow. With more than 40% incidence, ultra fast outflows (UFOs) are generated. These have a power of 10^{12-45}ergs^{-1} at 100-10^4gravitational radii from the source and eject 0.01-1 M yr^{-1} at velocities of 0.01c-0.1c (10^{3-4}kms^{-1}) [19]. AGN also produce jets at small solid angles of less than 1.0 sterad [20]; according to [21] these form at 10-100 GM/c^2, and [22] suggest that it happens at no more than 100 gravitational radii, forming at about 10^{15}cm and propagating to 10^{24}cm; jets carry 10^{43-46} ergs^{-1}, with Eddington ratio greater than 10^{-4}. Winds are also ejected at large, solid angles of more than 5.0 sterad with asymptotic velocity [20], and are powerful once the SMBH reaches M$_\bullet$>10^{7-8} M [23]. SMBH accretion occurs in quasar mode with Eddington rate of about 0.1-1 releasing energy either by radiation or radiative winds, and in the form of advection dominated accretion flow (ADAF) in the

thick region of the bulge ejecting mainly mechanical energy and momentum ant an angle of roughly ±0.6 rad [20].

Another form of outflow comes from winds generated by young stars. Such stars, with mass >5 M generate stellar winds that reach terminal velocity of 1000-3000 kms^{-1} immediately after they form [11]. In the case of lower mass stars radiative winds are ejected at a rate of 10^{-7} M yr^{-1} with terminal velocity of 100-400 kms^{-1} [24].

Young stellar object (YSO) also generate molecular outflows of maximum size 0.4-4 pc at dynamical ages 10^{3}-$2x10^{5}$ yr. This outflow has H_2 densities $\approx 10^{5}$ cm^{-3} and total momentum 0.1-1000 M kms^{-1} with average velocities in the range of 10-30 kms^{-1}, although higher velocity outflows have been detected. Molecular outflows are poorly collimated. In low velocity outflow, clumps of Extremely High Velocity gas (EHV) can be found, carrying a small portion of the mass, around 10^{-4}-10^{-2} M [25].

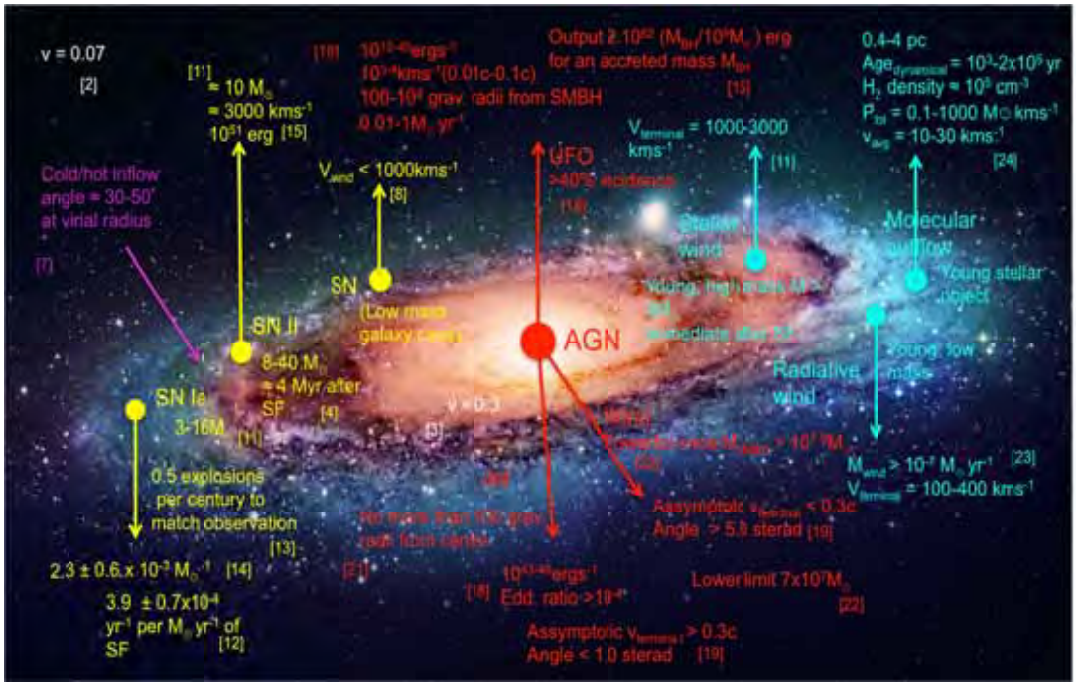

To Table of Contents

Fig. 1.: Outflow sources and related data.

The spin of the halo depends on its mass. High mass haloes are aligned perpendicularly. There exists a transition mass, depending on the scale of the filament and the distance of the halo from the cluster, where the alignment becomes parallel at lower masses, which are also redshift dependent, changing from perpendicular to parallel at z ~ 1. The alignment distance increases with increasing mass [26].

Parametric analysis

Considering a galaxy as a two-dimensional object, we may derive equations that would allow us to determine the position of material outflowing the galaxy over time.

The total force decelerating the outflow can be taken to be the gravitational force from the centre of the galaxy plus the drag force due to the viscosity of the medium:

$$F_{tot} = F_{grav}(d) + F_{drag}(v)$$

where the gravitational force is a function of distance from the centre of the galaxy and the drag force is a function of the outflow velocity.

The position after time t of the material can then be described by the following equations:

$$d_x(v(F), \theta, t) = x_o + v_x(F)t$$

$$d_y(v(F), \theta, t) = y_o + v_y(F)t$$

where the x and y components of the velocity can be obtained using the angle θ, and v is a function of F. In the case where outflow is perpendicular, the x component will not be necessary.

Outflow considered in this manner would cover a quadrant of the two-dimensional axis, but conservation of momentum requires outflow in both directions along each line of outflow, so it can be extrapolated.

The mass and energy outflow rates can be given as:

$M_{rate} = \Sigma\ (AGN, SNe, YSO)_{outflow}/t$

$E_{rate} = \Sigma\ (AGN, SNe, YSO)_{outflow}/t$

That is, the sum of mass and energy from each source in a given period of time t.

The data used for this model can be found in this table:

Source	Mass rate	Location/angle	Era	Velocity/ energy rate
SNII (8-40 $M_\odot$)	≈ 10 $M_\odot$	Disk	≈ 4 Myr after star formation	≈ 3000 kms^{-1} 10^{51} ergs
SNIa (3-16 $M_\odot$)	2.3±0.6x10^{-3} $M_\odot$ yr^{-1}	Disk	0.5 events per year	
Ultra Fast Outflow (UFO)	0.01-1 $M_\odot$ yr^{-1}	100-10^4 grav. radii from SMBH		10^{3-4} kms^{-1} 10^{12-45} $ergs^{-1}$
Jet		>100 grav. radii <1.0 sterad		$10^{45-46}ergs^{-1}$ > 0.3c
AGN winds	< 7x10^7 $M_\odot$	>5.0 sterad		< 0.3c
Stellar winds (>5$M_\odot$)		Star Formation Region (SFR)	Immediate after star forms	1000-3000kms^{-1}
Radiative winds (low mass star)	> 10^{-7} $M_\odot$ yr^{-1}	SFR		100-400 kms^{-1}
Molecular ouflows		SFR Max. Size 0.4-4pc	Dynamical age 10^3-2x10^5 yr	10-30 kms^{-1} 0.1-1000 $M_\odot$ kms^{-1}

Fig. 2.: Table of data

Conclusion

This work gives some equations that could be used to improve current large scale simulations and models by considering outflow in a way more closely matches observations. Future work might include equations relating the mass of the system that goes is a specific direction and including this work into larger simulations.

References

[1]. Dolag et al. MNRAS 370, 656-672 (2006).
[2]. Ruszkowski et al. MNRAS accepted (2006).
[3]. Schanne et al. ESA SP-622 (2006).
[4]. van de Voort et al. MNRAS 414, 2458-2478 (2011).
[5]. Freeman, May 2012 symposium. https://webcast.stsci.edu/webcast/detail.xhtml?talkid=3067&parent=1 .
[6]. Dekel et al. Nature, Vol 457, 451-454 (2009).
[7]. Stewart et al. ApJ 769, 74 (2013).
[8]. Sharma and Nath. ApJ (2012).
[9]. Booth et al. Nature (2013).
[10]. Del P. Lagos et al. MNRAS 000, 1-27 (2012).
[11]. Agertz et al. Submitted to ApJ (2012).
[12]. Sullivan et al. ApJ 648 (2006).
[13]. Schanne et al. ESA SP-622 (2006).
[14]. Toonen. ASP Conference Series (2013).
[15]. Cavaliere et al. ApJ 581 (2002).
[16]. Lagos et al. MNRAS 000, 1-27 (2007).
[17]. Wada and Venkatesan. ApJ, v.591 (2003).
[18]. Wagner et al. ApJ (2012).
[19]. Silk. ApJ 772, 112 (2013).
[20]. Sadowski et al. MNRAS (2013).
[21]. Narayan and McClintock. MNRAS (2011).
[22]. Komissarov Mem.S.A.It. Vol. XX, 1 (2010).
[23]. Feruglio et al. Astronomy & Astrophysics (2010).
[24]. Rodríguez-González et al. ApJ (2008).
[25]. Micono et al. To appear in Astronomy & Astrophysics.
[26]. Aragón-Calvo. MNRAS 000, 1-?? (2002).

Double Folding Analysis of ^{6}Li Elastic and Inelastic Scattering to Low Lying States on ^{208}Pb

Benedict Piñeyro

NSF/REU Program – Summer 2013

Physics Department, University of Notre Dame

Advisor:
Umesh Garg, Ph.D.

Graduate Student Collaborators:
James Matta
Darshana Patel

Abstract

Elastic scattering of 360 MeV ^{6}Li ions from ^{208}Pb was measured from $2.9° \leq \theta_{Lab} \leq 33°$. The data were fitted with two different potentials, one with the real volume potential folded and one with both real and imaginary volume potentials folded, derived from the M3Y density dependent Nucleon-Nucleon interaction. Distorted Wave Born Approximation (DWBA) calculations were performed with the fitted parameters to calculate cross-sections for inelastic scattering to low lying 3^- states.

Introduction

Nuclear incompressibility is the energy needed to change the density of nuclear matter around equilibrium [1]. It is an important parameter of the equation of state (EOS) of nuclear matter and has a variety of applications mainly in the astrophysics field. The nuclear EOS is used to determine the radii of neutron stars [1], predict the dynamics of supernovas, and in simulation of heavy ion collisions [2]. In order to determine the incompressibility of a nucleus, the direct connection between the nuclear incompressibility and the energy of the Isoscalar Giant Monopole Resonance (ISGMR) is exploited [3]. Equation (1) shows the correlation between the energy of this compression mode and the nuclear incompressibility parameter [3]:

$$\bar{E}_{ISGMR} = \sqrt{\frac{\hbar^2 K_A}{m\langle r^2 \rangle}} \qquad (1)$$

Where $\bar{E}_{ISGMR}$ is the centroid energy of the compression mode, $(\hbar)$ is the reduced Planck's constant,(m) is the nucleon mass, K_A is the nuclear incompressibility, and $(\langle r^2 \rangle)$ is the ground-

To Table of Contents

state mean-square radius, with $\langle r^2 \rangle = \frac{4\pi \int_0^\infty \rho(r) r^2 \cdot r^2 dr}{4\pi \int_0^\infty \rho(r) r^2 dr}$. Where $\rho(r)$ is the nuclear matter density distribution with respect to radius.

To extract ISGMR energies, elastic and low-lying inelastic scattering data are used to find and confirm the nuclear potential parameters. These parameters are then used to calculate the differential cross-section of scattering to the various giant resonances. These are then used to perform a multipole decomposition analysis to extract the strength distribution of the ISGMR with respect to excitation energy which then yields the centroid energy of the ISGMR [4].

With Radioactive Ion Beam (RIB) facilities becoming more common we have the opportunity to measure ISGMR energies and strength distributions far from stability. Unfortunately, given the use of inverse kinematics necessitated by RIB facilities one must be careful in choosing the probe [5]. ^{6}Li is the most appropriate solid target probe because it can be made thin enough for recoils to escape, it has a small mass, and it has an isospin of T=0 [5]. Unfortunately little is known about using ^{6}Li as a probe of the ISGMR. As such an experiment to get elastic and inelastic scattering cross-sections was performed with ^{208}Pb using the Grand Raiden spectrometer at RCNP in the University of Osaka, Japan.

Procedure

The raw data was converted into n-tuples using an analyzer written by Dr. Masaru Yosoi of RCNP. Using ROOT [6], the n-tuples were then analyzed. First, a particle ID gate was set on ^{6}Li particles; next, background regions were defined using the vertical positioning of the particles. Finally, gated and background subtracted spectra of counts vs. scattering angle vs. focal plane x position were obtained. With these spectra the number of counts scattered into each angular

region were obtained giving angular distributions of the differential cross-section for elastic scattering and scattering to the first excited state of ^{208}Pb.

The unpublished code dfpd4 [7] was then used to compute folded real volume and coulomb potentials for elastic scattering and transition potentials to ^{208}Pb's 3^- excited state from the ^{6}Li and ^{208}Pb nuclear density distributions and the M3Y-Paris density [8] dependent nucleon-nucleon interaction. Using the DWBA/coupled channel code ECIS [9], fits were then performed on the normalization of the real volume potential and the depth, radius and diffusivity of the imaginary volume, real surface, and imaginary surface potentials. It is interesting to note that the breakup of ^{6}Li is accounted for with the normalization of the folded potential being ~0.65 (as opposed to 1.0). Once a good fit of calculated differential cross-sections to the elastic scattering data had been obtained the parameter set was tested by calculating the angular distribution of the first excited state using the known B(E3) [10] value and the potential parameters. If the calculated distribution was in good agreement with the excited state scattering data then the potential parameters were deemed good.

Additionally, the unpublished code dfpd5 [11] was used to calculate folded real volume, imaginary volume, and coulomb potentials for elastic scattering and transition to the ground state. Once again fits were performed using ECIS, fitting the normalization of the folded imaginary volume potential, and the depth, radius, and diffusivity of the real surface and imaginary surface potentials. At Dr. Khoa's suggestion, the real volume potential normalization was fixed at 1.0 and the real surface depth was allowed to go negative, producing a repulsive interaction which provided for the break-up for ^{6}Li. As before the parameters obtained were testing by using them and the known B(E3) value to calculate excited state distributions for comparison.

Results and Analysis

Hybrid Model 1

This model consisted of a folded real volume potential, a Woods-Saxon imaginary volume potential, and real and imaginary surface Woods-Saxon potentials. The parameters are shown in Table 1.

	Normalization	$Depth\ (MeV)$	$r_0\ (fm)$	$a_0\ (fm)$
$Real\ Volume$	0.7119181	–	–	–
$Imaginary\ Volume$	–	50.979485	0.814588	1.188500
$Real\ Surface\ Potential$	–	0.018280	1.141104	0.861466
$Imaginary\ Surface$	–	10.218913	1.132484	0.763733

Table 1: The potential parameters for the first hybrid model.

An initial set of parameters for the real and imaginary volume potentials were found via a brute force search of the parameter space. With those as initial values the full parameter set was fit using more traditional gradient descent χ^2 minimization techniques. The final χ^2 for the elastic scattering was 388. Shown in Figure 1 is a plot of the experimental elastic scattering cross-sections and the calculated differential cross-sections using the Optical Model Parameters (OMP) shown above. Additionally, as a test of their validity the OMP and the transition potentials obtained from them using the B(E3) were used to calculate the differential cross-section for scattering into the 3^- state as shown in Figure 2.

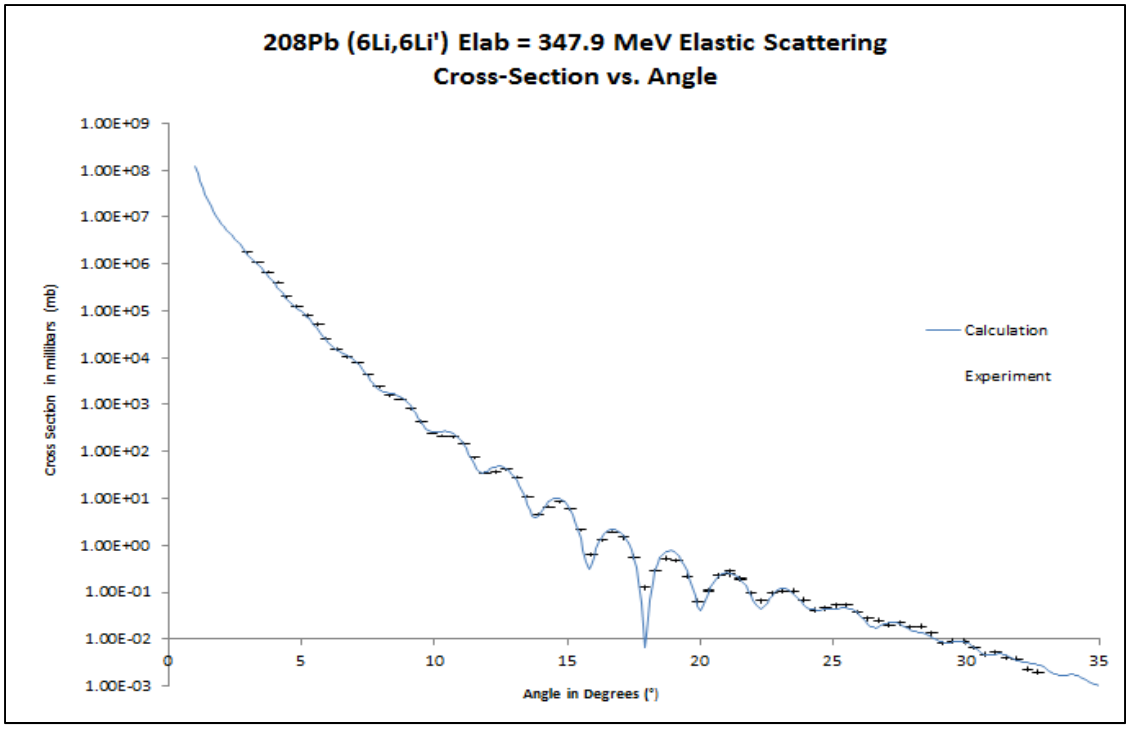

Figure 1: The optical model fit for the elastic scattering (0+ state) data with a hybrid double folding fit.

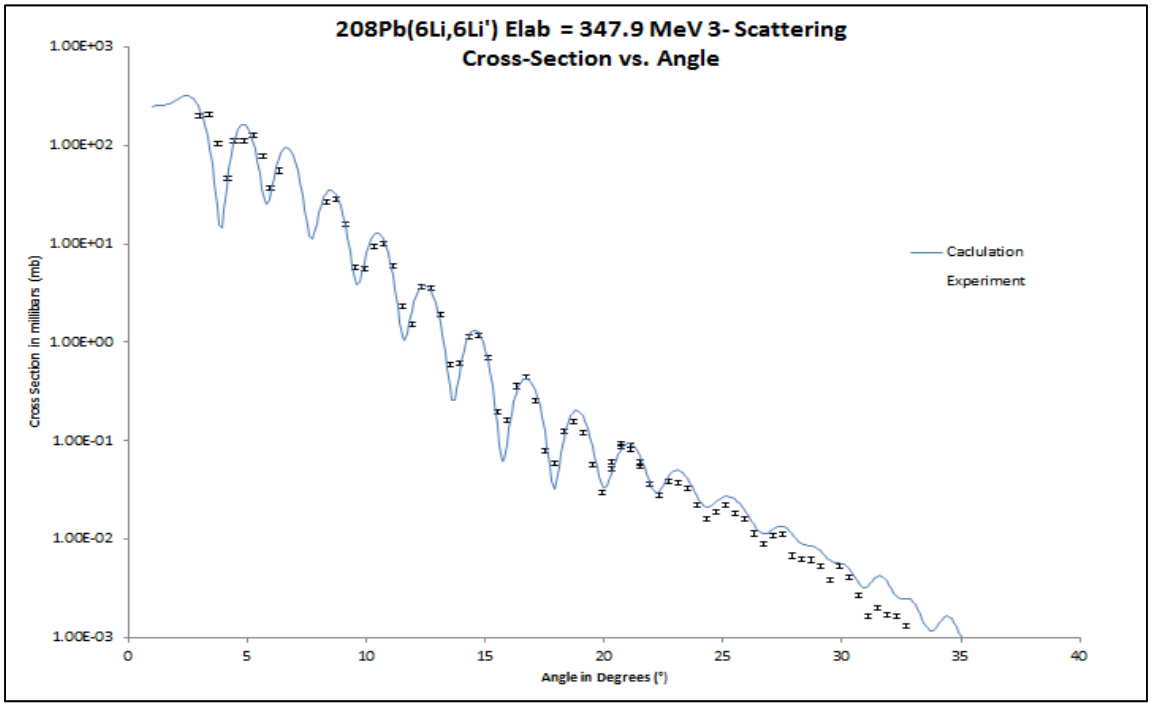

Figure 2: The same optical model with transition potentials for the 3- state taken into account to calculate the inelastic scattering of the data set. As can be seen the calculation does a good job up to ~25 degrees and so the parameters were accepted.

Hybrid Model 2

This model consisted of a folded real volume potential, a folded imaginary volume potential, and real and imaginary surface Woods-Saxon potentials. As stated earlier the real normalization was held at 1.0 and the real surface potential was allowed to become repulsive to provide for the breakup of ^{6}Li. The values obtained for the best fit are given in Table 2.

	Normalization	$Depth\ (MeV)$	$r_0\ (fm)$	$a_0\ (fm)$
$Real\ Volume$	1.0	–	–	–
Imaginary Volume	1.471305	–	–	–
$Real\ Surface$	–	−9.80969	1.150663	0680277
$Imaginary\ Surface$	–	5.2964890	1.083166	0.295855

Table 2: The potential parameters for the second hybrid model.

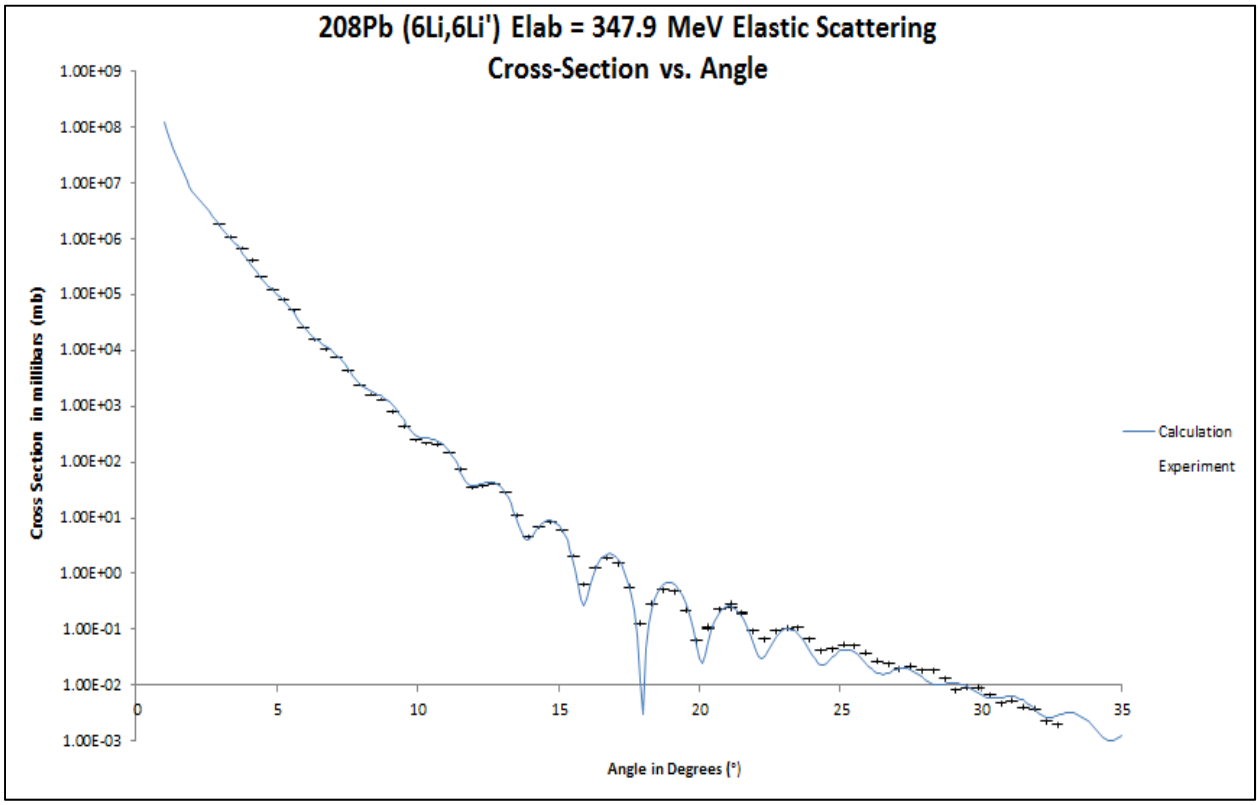

Figure 3: The optical model fit for the elastic scattering (0+ state) data with the second hybrid model.

As before transition potentials were obtained using the fitted OMP and the known B(E3) value. The results of this calculation are in Figure 4. As can be seen however poor agreement was found between the calculated cross-sections for 3^- scattering and the experimentally obtained cross-sections showing a need for further refinement of the OMP.

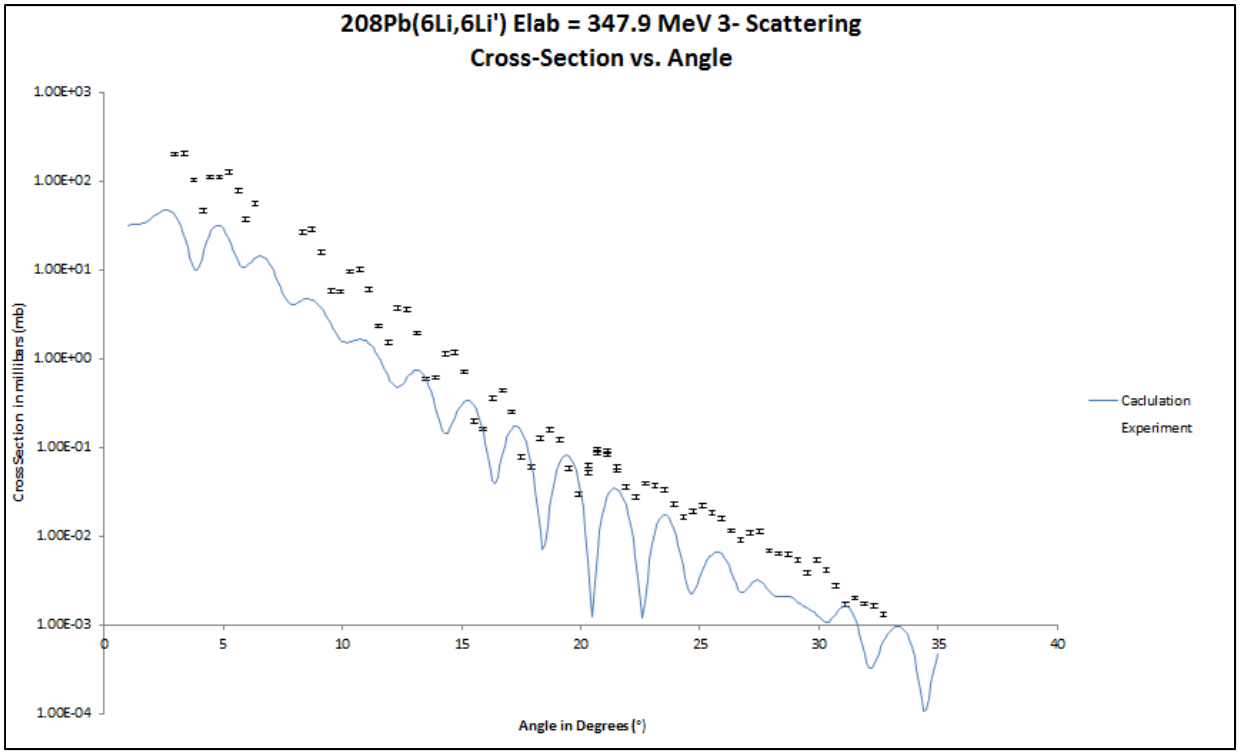

Figure 4: The optical model fit for the 3^- state scattering data with the second hybrid model.

Conclusion

The optical model parameters found fit the elastic scattering and inelastic scattering data well for the first hybrid double folding model. The optical model parameters for second hybrid double folding model need further refinement as Figure 4 shows.

Future Work

The parameters for the second hybrid model will be improved and once it produces a good match for the elastic and inelastic data, the parameters will be combined with inelastic scattering to find ISGMR energies and strength distributions.

References

[1] J. Lattimer, Annu. Rev. Nucl. Part. Sci. 62, 485 (2012)

[2] N. K. Glendenning, Physical Review C37, 2733 (1988)

[3] S. Stringari, Physics Letters B108, 232 (1982)

[4] S. Shlomo, V. Kolomietz and G. Colo, European Physical Journal A30, 26 (2006)

[5] A. Galindo-Uribarri, et al., Nucl. Instr. And Meth. B172, 647 (2000)

[6] R. Brun and F. Rademakers, Nucl. Instr. And Meth. A 389, 81 (1997)

[7] D. T. Khoa, computer program DFPD4, private communication

[8] T. Kibedi, and R. H. Spear, Atomic Data and Nuclear Data Tables 80, 35 (2002)

[9] J. Raynal, computer program ECIS97 (1998), - O.E.C.D.Nuclear Energy Agency, Paris, France

[10] D. T. Khoa, computer program DFPD5, private communication

[11] N. Anantaraman, H. Toki, and G. F. Bertsch, Nucl. Phys. A 398, 269 (1983)

Formation of Relativistic Jets around a Black Hole due to the Magnetic Field generated by an Accretion Disk

Adrien Saremi

2013 NSF/REU Program
Physics Department, University of Notre Dame
Project GRAND

Advisor: Professor John Poirier

Contributors: Jared Johnson
Aaron Sawyer

Abstract

Black holes are well known to attract anything that passes their surroundings due to their large mass, but some also have the ability to eject matter in two powerful jets along their axis of rotation called relativistic jets. The main explanation to their formation is the magnetic field produced by the accretion disk located in the equatorial plane of the black hole, but can also be attributed to the twisting of space-time around the compact mass. Our project consists in studying the magnetic field produced by the accretion disk and how a particle can, under the influence of this B-field, move from its circular motion to an upward direction along the z-axis (axis of rotation). To do so, we designed a program that computes and draws the magnetic field lines of the accretion disk. Once this was done, we then designed another code to compute the trajectory of a particle, starting from different positions in the accretion disk. Our work also consisted of verifying our program's calculation, by establishing mathematical formulas to calculate the B-field in specific cases.

Magnetic Field

In order to compute the magnetic field generated by the spinning and charged accretion disk, we first considered the disk as the summation of many single rings. Doing so, we do not deal with charged density, or angular velocity anymore, but with the current running each loop. Then, the Biot-Savart law allows us to compute the B-field produced by each loop:

$$\overrightarrow{dB} = \frac{\mu_0}{4\pi} \frac{I\overrightarrow{dl} \times \overrightarrow{r}}{r^3}$$

where μ_0 is the permittivity of the vacuum = $4\pi \times 10^7$ T.m.A^{-1}
I is the intensity running the loop (in Amperes)
dl is the infinitesimal element of length of the source
R is the radius of the loop
$\vec{r}$ is the vector from source to detector
$\vec{r} = \vec{r} - \overrightarrow{r'}$ where $\vec{r}$ is the detector position and $\overrightarrow{r'}$ is the source position

For the specific case of a loop in the (x,y) plane, we have:

$$\vec{r} = \begin{pmatrix} x \\ y \\ z \end{pmatrix} \quad \text{and} \quad \overrightarrow{r'} = R\begin{pmatrix} cos\varphi \\ sin\varphi \\ 0 \end{pmatrix} \quad \text{and} \quad \overrightarrow{dl} = R\begin{pmatrix} -sin\varphi \\ cos\varphi \\ 0 \end{pmatrix} d\varphi$$

$$r^2 = [(x - Rcos\varphi)^2 + (y - Rsin\varphi)^2 + z^2]^{1/2}$$

$$\overrightarrow{dl} \times \vec{r} = R\begin{pmatrix} z * cos\varphi \\ z * sin\varphi \\ R - ysin\varphi - xcos\varphi \end{pmatrix} d\varphi$$

Therefore:

$$B_x = \frac{\mu_o IR}{4\pi}\int_0^{2\pi} \frac{z\, cos\varphi\, d\varphi}{[(x - Rcos\varphi)^2 + (y - Rsin\varphi)^2 + z^2]^{3/2}}$$

$$B_y = \frac{\mu_o IR}{4\pi}\int_0^{2\pi} \frac{z\, sin\varphi\, d\varphi}{[(x - Rcos\varphi)^2 + (y - Rsin\varphi)^2 + z^2]^{3/2}}$$

$$B_z = \frac{\mu_o IR}{4\pi}\int_0^{2\pi} \frac{(R - ysin\varphi - xcos\varphi)\, d\varphi}{[(x - Rcos\varphi)^2 + (y - Rsin\varphi)^2 + z^2]^{3/2}}$$

Each of these quantities is difficult to integrate mathematically. Instead, we computed them by doing approximations: we computed each of the B-field component by summing the magnetic field over small portions of the loop, using an increment of $d\varphi = 1°$.

In order to have a more general representation of the magnetic field, we computed it in the (y,z) plane. Therefore $x = 0$, and the magnetic field in the x-direction is $B_x = 0$. Figure 1 shows the magnetic field lines in the (y,z) plane. The spacing between the lines represented is inversely proportional to their magnitude on the y-axis.

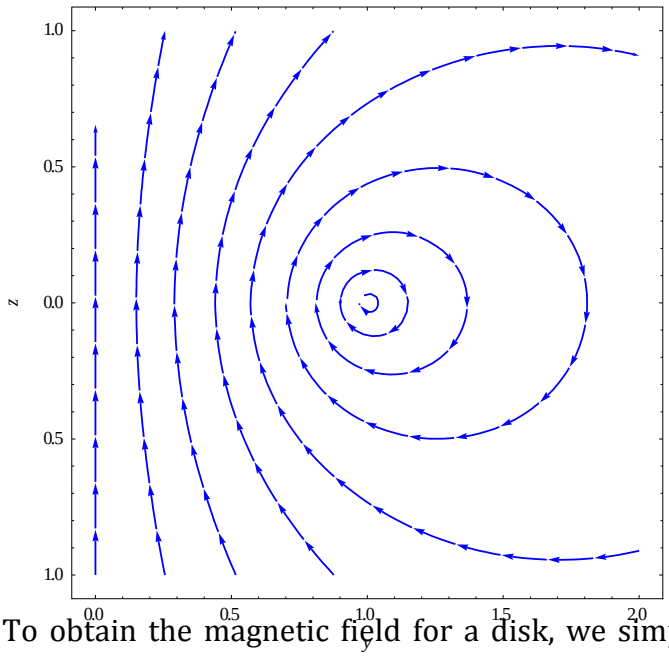

Figure 1. Lines of magnetic force in the (y,z) plane, for a loop of radius $R = 1.0\ m$ and run by a current $I = 1.0\ A$

To obtain the magnetic field for a disk, we simply add the previous results for a certain amount of rings, each of different radiuses. In our case, we decided to run the disk from 1.0 to 2.0 meters and to use 100 rings. Another characteristic specific to the accretion disk is that the current run in each loop is inversely proportional to the square root of the radius $I = \frac{1.0}{\sqrt{R}}$. The reason is that the speed of the particle on the accretion disk follows the same law (from Newton's second law):

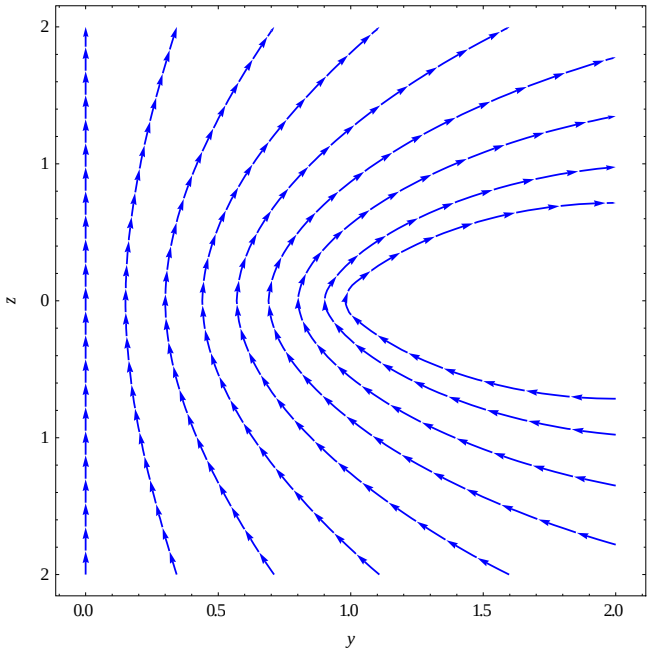

Figure 2. Lines of magnetic force for an accretion disk running from 1.0 to 2.0 m, and current $I = \frac{1.0}{\sqrt{R}}$.

Different Methods to compute the Magnetic Field

In order to make sure that our program is correct, we mathematically computed B for points on the z-axis and off the z-axis. Instead of reasoning on infinitesimal source of currents like in our program, we here deal with integral forms. The difficulty of this method lies on different levels, mostly on the position where we want to compute the field (the detector position).

Current loop – Detector on the z-axis: We use the Biot-Savart Law once again, but here $\vec{r} = \begin{pmatrix} 0 \\ 0 \\ z \end{pmatrix}$. Therefore, the integrations on the x and y-axis cancel, and only the B_z remains:

$$B_z = \frac{\mu_0 I}{4\pi} \int \frac{R^2 d\varphi}{(R^2 + z^2)^{3/2}} \vec{k} = \frac{\mu_0 \, I \, R^2}{2(R^2 + z^2)^{3/2}} \vec{k}$$

$$\boldsymbol{\vec{B} = \frac{\mu_0 \, I \, R^2}{2(R^2 + z^2)^{3/2}} \vec{k}}$$

Current Loop – Any point in space: The mathematics gets way more complicated at this point, since there's no evident simplification in the cross product under the integral. We use another method here, but we will not go over the full proof, just the most important steps. We use cylindrical coordinates: *P(r,0,z)*. The reason why we leave Φ = 0, the angle position, is because of the symmetry of the problem. Indeed the position of *P* is *Φ* -independent.

Before computing the magnetic field, we first compute the vector potential $\vec{A}$:

$$\boldsymbol{\vec{A} = \frac{\mu_0 \, I}{4\pi} \int \frac{\vec{dl}}{r}}$$

where r is the distance between the point source and the detector

- $r^2 = z^2 + r^2 + a^2 - 2racos\phi'$
- $\vec{dl} = a \begin{pmatrix} -sin\phi' \\ cos\phi' \\ 0 \end{pmatrix} d\phi'$ (in Cartesian) $= ad\phi' \vec{e_\theta}$ (in cylindrical)

where a is the radius of the ring and ϕ' is the angle from the axis to the source point.

Many steps later, we come with an expression of $\vec{A}$ expressed in polar coordinates.

$$\vec{A} = \frac{\mu_0 I \sqrt{a}}{2\pi}\left(2k^{-1}r^{-\frac{1}{2}}E_1(k) - 2k^{-1}r^{-\frac{1}{2}}E_2(k) - kr^{-\frac{1}{2}}E_1(k)\right)\overrightarrow{e_\theta}$$

where $k = \sqrt{\frac{4ra}{z^2+(a+r)^2}}$ and where $E_1(k)$ and $E_2(k)$ are respectively the elliptic integrals of the 1st and the 2nd kind, given by the following

$$E_1(k) = \int_0^{\pi/2} \frac{d\theta}{\sqrt{1-k^2 sin(\theta)^2}} \qquad E_2(k) = \int_0^{\pi/2} \sqrt{1-k^2 sin(\theta)^2}\, d\theta$$

As we can note, $\vec{A}$ only lies on $\overrightarrow{e_\theta}$ which implies that $\vec{B}$ only has radial and z components in polar coordinates. Coming back to the definition of $\vec{A}$ and $\vec{B}$:

$$\vec{B} = \nabla \times \vec{A} = \frac{1}{r}\begin{vmatrix} \overrightarrow{e_r} & r\overrightarrow{e_\Phi} & \overrightarrow{e_z} \\ \frac{\partial}{\partial r} & \frac{\partial}{\partial \Phi} & \frac{\partial}{\partial z} \\ A_r & rA_\Phi & A_z \end{vmatrix} = \frac{1}{r}\left(\frac{\partial(rA_\Phi)}{\partial r}\overrightarrow{e_z} - \frac{\partial(rA_\Phi)}{\partial z}\overrightarrow{e_r}\right) = B_r\overrightarrow{e_r} + B_z\overrightarrow{e_z}$$

If Φ is the angle running from the positive x-axis to the vector position, since there is no B_Φ:

$$B_x = B_r \cos(\Phi)$$
$$B_y = B_r \sin(\Phi)$$

Therefore:

$$\boldsymbol{B_x = \frac{\mu_0\, z\, I}{2\pi r\sqrt{z^2+(a+r)^2}}\left(\frac{a^2+z^2+r^2}{z^2+(a-r)^2}E_2(k) - E_1(k)\right)\cos(\Phi)}$$

$$\boldsymbol{B_y = \frac{\mu_0\, z\, I}{2\pi r\sqrt{z^2+(a+r)^2}}\left(\frac{a^2+z^2+r^2}{z^2+(a-r)^2}E_2(k) - E_1(k)\right)\sin(\Phi)}$$

$$\boldsymbol{B_z = \frac{\mu_0\, I}{2\pi\sqrt{z^2+(a+r)^2}}\left(\frac{a^2-z^2-r^2}{z^2+(a-r)^2}E_2(k) + E_1(k)\right)}$$

Particle Trajectory:

Our final model consists of a particle rotating in the accretion disk and then, under the influence of the magnetic field, rising up to reach the z-axis. The particle starts in the (y,z) plane at a small $z = \varepsilon$ and at a $y = y_0$ with an initial velocity directed in the x-direction $\vec{v} = v_0 \vec{\imath}$. The reason why we start the particle at a small $z = \varepsilon$ is simply because the field diverges as we position ourselves on the disk.

The Lorentz force acting on the particle is due to the magnetic field and satisfies the second law of Newton:

$$\frac{d\vec{p}}{dt} = q\left(\vec{v} \times \vec{B}\right)$$

$$\begin{pmatrix} \Delta v_x/\Delta t \\ \Delta v_y/\Delta t \\ \Delta v_z/\Delta t \end{pmatrix} = \frac{q}{m}\begin{pmatrix} v_x \\ v_y \\ v_z \end{pmatrix} \times \begin{pmatrix} B_x \\ B_y \\ B_z \end{pmatrix} = \frac{q}{m}\begin{pmatrix} v_y B_z - v_z B_y \\ v_z B_x - v_x B_z \\ v_x B_y - v_y B_x \end{pmatrix}$$

We're now going to consider Δt sufficiently small so that the variation in velocity remains constant over that amount of time:

$$\begin{cases} \boldsymbol{\Delta v_x = \frac{q}{m}\left(v_y B_z - v_z B_y\right)\Delta t} \\ \boldsymbol{\Delta v_y = \frac{q}{m}\left(v_z B_x - v_x B_z\right)\Delta t} \\ \boldsymbol{\Delta v_z = \frac{q}{m}\left(v_x B_y - v_y B_x\right)\Delta t} \end{cases}$$

For each step Δt, the program reads the position and the velocity of the previous step (the initial conditions). It then computes the magnetic field at this point in order to obtain $\Delta\vec{v}$, from which we get $\overrightarrow{v_f} = \overrightarrow{v} + \Delta\vec{v}$ and finally the new vector position: $\overrightarrow{R_f} = \overrightarrow{R} + \vec{v} \times \Delta t$. This operation is repeated over a certain amount of steps, and we can then obtain the trajectory of

the particle. In order to make sure that the particle's trajectory computation was correct, the change in velocity was checked by hand calculation for many steps.

We then computed the trajectory of particles starting at different positions on the y-axis. Meanwhile, the data used was:

- $\Delta t = 5 \times 10^{-10}\ s$
- ${}^{q}/_{m} = 1.76 \times 10^{11}\ C.kg^{-1}$
- $y_0 = 1.1; 1.2; 1.3; 1.4; 1.5$
- $z_0 = 0.2\ m$
- $v_0 = 10^8\ m/s$
- 100 steps

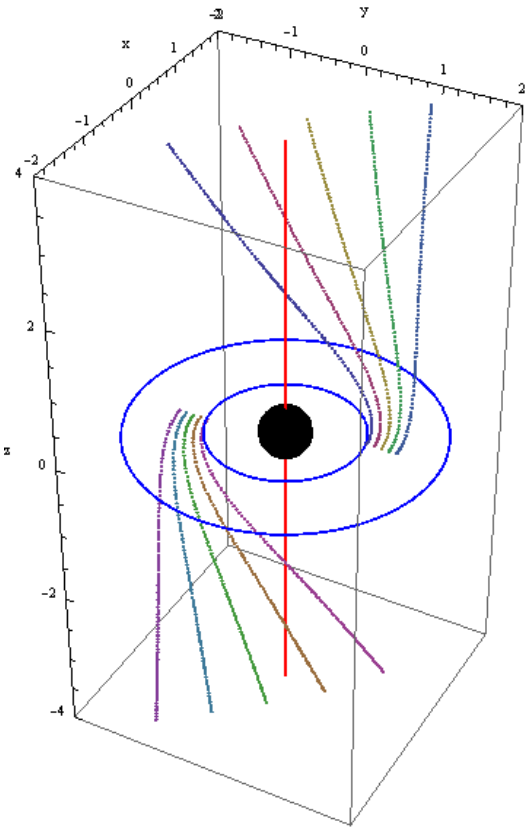

Figure 3. Three-dimensional image of the particle trajectory, due to the magnetic field of the accretion disk. In this case, the black hole, represented by its event horizon here (the limit of no return for any particle) is a Kerr Black Hole, which means it is spinning but it is not charged.

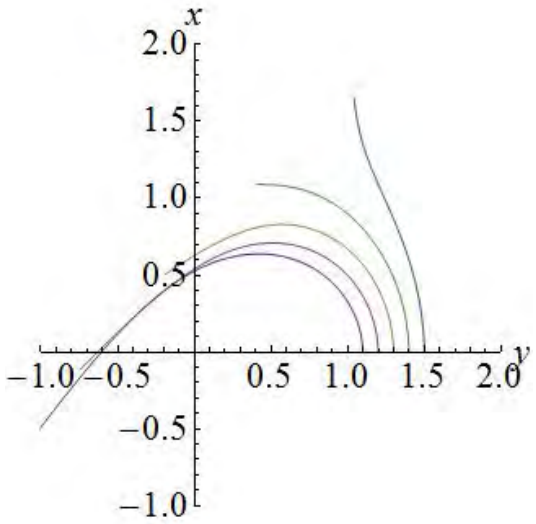

Figure 4. Particles' trajectory in the (x,y)

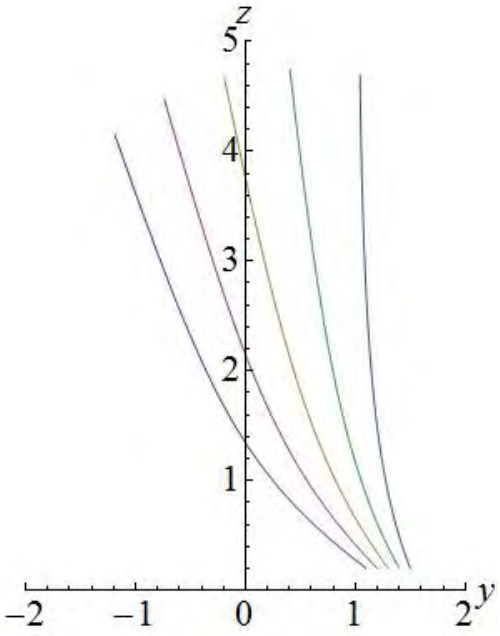

Figure 5. Particles' trajectory in the (y,z) plane

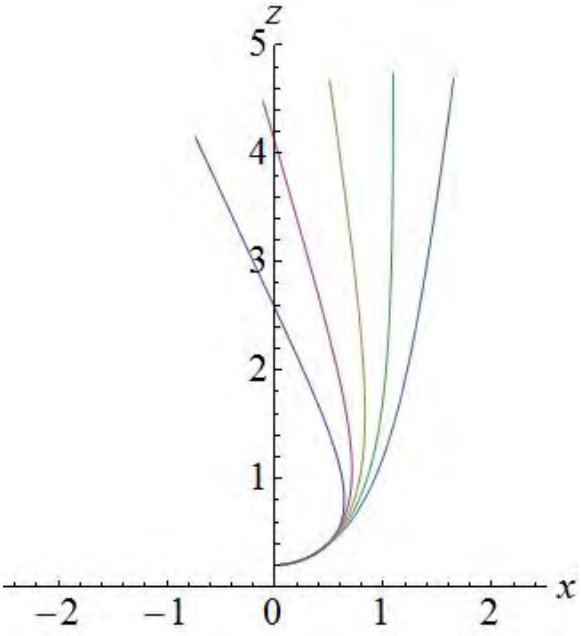

Figure 6. Particles' trajectory in the (x,z) plane

Formation of relativistic jets

As we can see, the particles leave the accretion disk and move in an upward/downward direction, to reach the axis of rotation of the black hole. Nevertheless (figure 5) the particles tend to move on a straight line when they get close to the z-axis, some passing the z-axis and even getting further from it. So how do the particles stay on the z-axis ? The

answer lays in general relativity theory. As we get close to the black hole, space and time get twisted due to the very large mass of the object. According to the current model established by Roger Blandford in his publication "Electromagnetic extraction of energy from Kerr black holes," the **magnetic field lines get also twisted** around the axis of rotation of the black hole, resulting in a collimation of the particles onto the z-axis. This also explains why the relativistic jets are huge in length: the twisting being very powerful close to the equatorial plane, it creates a strong pressure gradient along the axis which accelerates the flow of particle to become relativistic jets.

Acknowledgments: I would first like to thank Dr. John Poirier for his guidance throughout the summer and Dr. Umesh Garg for his involvement in the REU program. In addition, I would also like to thank my coworkers Jared Johnson and Aaron Sawyer for their contribution to our project. Finally, I would like to thank Dr. Mark Caprio of the University of Notre Dame, Dr. Thomas Catanach of Cal Tech, and Dr. Michael Sostarecz of Monmouth College for their support and their help in plotting our graphs in Mathematica.

Work Cited:

Blandford, R. D., & Znajek, R. L. 1977, MNRAS, 179, 433

Simonsen, Mike. "J-E-T-S, Jets, Jets, Jets!" *Universe Today.* Word Press Admin, 25 November 2010. Web. 1 August 2013.

"Deriving the expression for the off-axis magnetic field of a circular current loop." *Grant Trebbin.* Blogger, 11 April 2012. PDF File.

Marscher , A.P."Jets in Active Galactic Nuclei" Institute for Astrophysical Research, Boston, 14 September 2009. PDF File.

Non-Interceptive Beam Monitor Prototype

Trevor Satterfield

2013 NSF/REU Program Physics Department, University of Notre Dame

Advisor: Dr. Manoel Couder

Abstract

Nuclear astrophysicists study nuclear reactions to understand the energy production and nucleosynthesis in stars. Since Nuclear Astrophysicists cannot directly measure the cross section of nuclear reactions in stars, experiments involving particle accelerators have to be used. Nuclear reactions take place in stars at relatively low energies where the cross section is very small. In the laboratory, high intensity beam is preferred because it increases the reaction yield. As the high intensity beam interacts with materials it may melt the material. In this work we focus on a non-interceptive solution as an alternative to the standard slits in order to evaluate the size and profile of the beam. As the beam travels through vacuum, regardless of the quality of the vacuum, it interacts with the residual gas, mostly nitrogen. Through this interaction between the beam and the material, visible light will be generated which can be used as a diagnostic of the beam position and profile. Such a system is used in a setup developed by German physisists (F. Becker (2007) et al., Proc. DIPAC'07) at energies greater than 200 MeV/u with an intensity of approximately 10 nA. Also, another system is used by D. Seil (UU. 2005) with beam energy of 50 keV and a beam intensity of 30 mA. However, no one has attempted to use the residual vacuum fluorescence at energies and intensities between these ranges in the interest of nuclear astrophysics with stable beams. Therefore, research at these energies is of great importance to Notre Dame not only for the new Santa Ana (5U) accelerator which was recently installed (isnap.nd.edu), but for the future underground accelerator laboratory, DIANA which will be able to reach even higher intensities. . (Lemut A. (2011) 10.1103/PhysRevSTAB.14.100101) Results of a preliminary non-interceptive beam monitor prototype are presented.

Introduction

Astrophysicists focus on nuclear physics that happens in stars. These nuclear reactions play a crucial role in energy production and nucleosynthesis in stars. Nucleosyntheseis is the nuclear processes that form elements in stars. So, naturally they want to study the closest star, which is the sun. For centuries humanity struggled to understand the energy source of the sun. A few centuries ago we thought that the energy source was coal because at that time it was the newest technological fuel source. However, through energy calculations this idea was rejected. We now know that the fuel source in the sun is the nuclear fusion of four protons that result in a helium atom. Even though we understand the fuel source of the sun, we don't understand the sun completely, much less the other stars in the universe. This is why astrophysics has to turn to research methods that can be executed in a laboratory. One method is to measure the nuclear cross section, the probability that a nuclear reaction will occur, in particle accelerators.

Recently Notre Dame has received a new particle accelerator which is called 5U, cite. This accelerator will be able to reach energies up to 5 Mev with an intensity of approximately 200 μA. (isnap.nd.edu) Additionally, researchers of Notre Dame and five other institutions are preparing plans for an underground particle accelerator facility which is called Dual Ion Accelerator for Nuclear Astrophysics or DIANA for short. This new facility will be able to reach an intensity of 100 mA at energy of 50 keV. (Lemut A. (2011) 10.1103/PhysRevSTAB.14.100101) As you have noticed the intensity has increased but the energy has decreased with this new underground facility. The reason

why is because having a higher intensity allows you to study the cross section at lower energies.

This is very important to astrophysicists because as you increase the intensity the numbers of reactions increase as well which causes the experiments to be more efficient both in time and in money. The only down side to this idea is as you increase the intensity in the beam line the slits that you are using to measure and profile the beam can melt. The maximum power that the beam can dissipate can be calculated by:

$$Beam\ Energy\ (J)\ X\ Beam\ Intensity\ (particles/second) = Power\ (W)$$

$$100 * \ 10^{-3}\ A \sim 6.2e\ 17\ \ particles/sec$$

$$50\ keV = 8e - 18\ J$$

$$8ee - 18\ J\ \times\ 6.2e\ 17\ \frac{particles}{sec} = 5\ kW$$

As you can tell by using DIANA (Lemut A. (2011) 10.1103/PhysRevSTAB.14.100101) as an example there is a lot of power being dissipated in the slits if the full beam is stopped. A couple solutions exist to avoid melting the beam profiling slits.

One is you can cool the slits by using water to dissipate the energy delivered to the profiling slits, but can be expensive. Another solution is to remove the slits altogether and use a non-interceptive method to profile the beam. The idea is as the particle beam moves through the vacuum it will ionize the residual gas, which will produce a visible profile of the beam. Such a research system is already in use by German physicists (F. Becker (2007) et al., Proc. DIPAC'07). This group uses the system at energies greater than 200 MeV/u with an intensity of approximately 10 nA. There is another system used by D. Seil (UU. 2005) in which the beam energy is 50 keV with a beam intensity of 30

mA. However, no one has attempted to use the residual vacuum fluorescence at energies and intensities between these ranges in the interest of nuclear astrophysics with stable beams.

Prototype

Since using the particle accelerators at Notre Dame is costly both in time and in money a prototype that can demonstrate the feasibility of the concept in vacuum and at the similar intensities as the one provided by the 5U has been developed. The physics behind this prototype is similar to light bulbs neon lights. The process involved is known as glow discharge. A flow of electrons impacts trace amounts of gas which causes the gaseous atoms to become exited. These exited atoms then fall back down releasing a photon. The photon that is released using nitrogen or gases in light bulbs and neon lights is in the visible spectrum.

Figure 1 showing the exitation and de exitation of an atom.
www.infohow.org

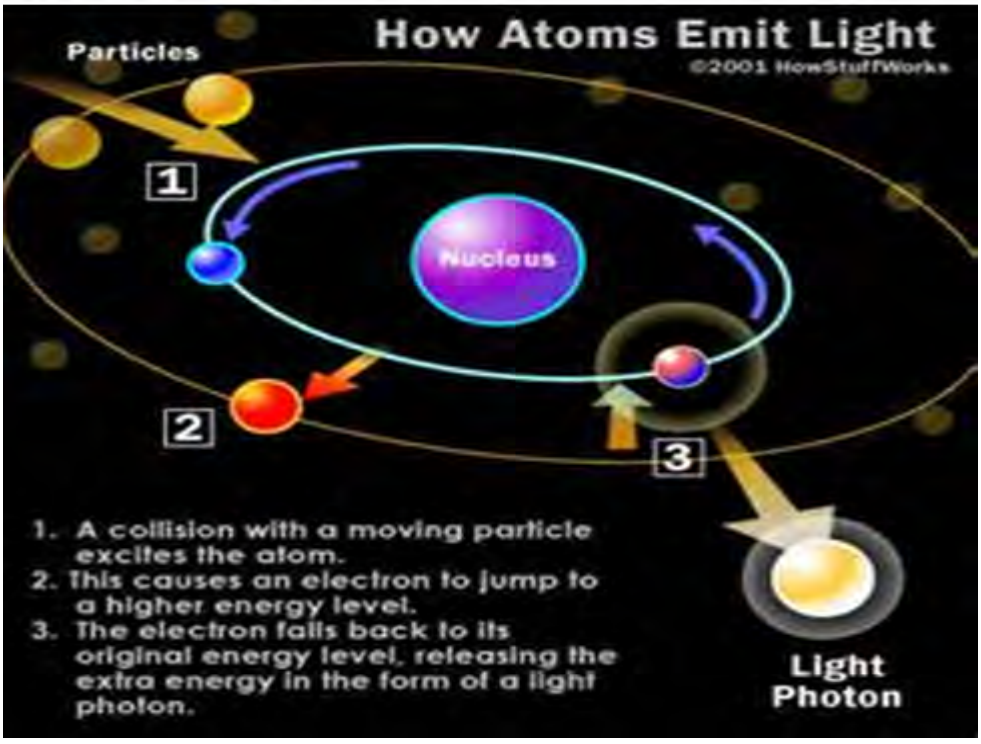

To Table of Contents

The prototype used consists of a t-pipe line attached to a cart that has a turbo pump and a fore pump. The t-pipe line has four sides. Attached to side A is a cathode ionization gauge to measure pressure. Attached to side B is a window to view the interaction with a camera or your naked eye. Attached to side C is an electrode system used to create the glow discharge. Connected to the electrode system is high voltage wires, which allows voltage to enter the chamber.

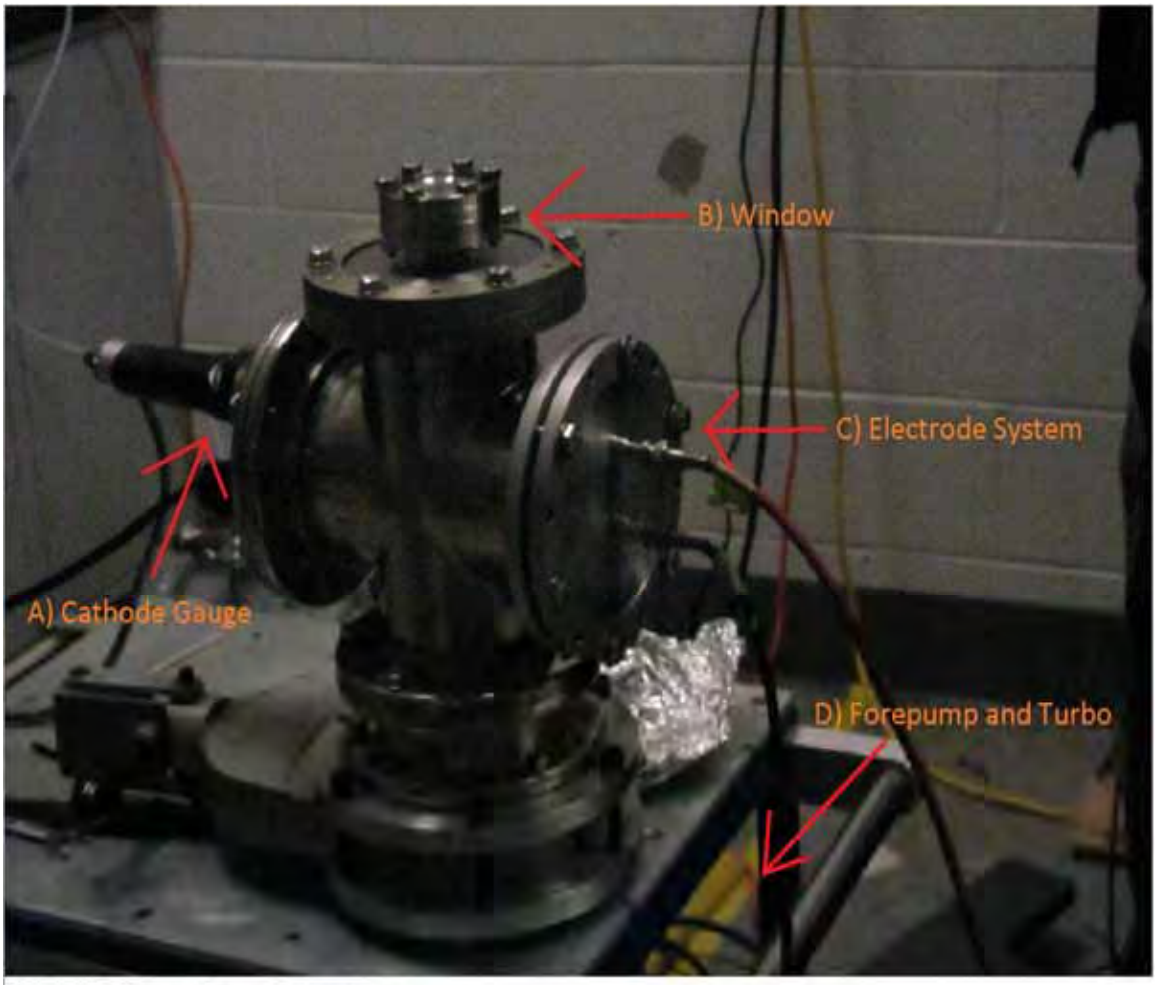

Figure 2 shows the prototype
A) shows the cathode gauge
B) shows the window
C) shows the electrode system with high voltage wires attached.
D) under the prototype is the forepump and turbo pump.

The electrode system is supported by a delron platform which also serves to absorb the reflection of the glow discharge light. Connecting the two electrodes are two insulated wires. Surrounding the connection of the wire and the SHV connectors is a polyethylene tube.

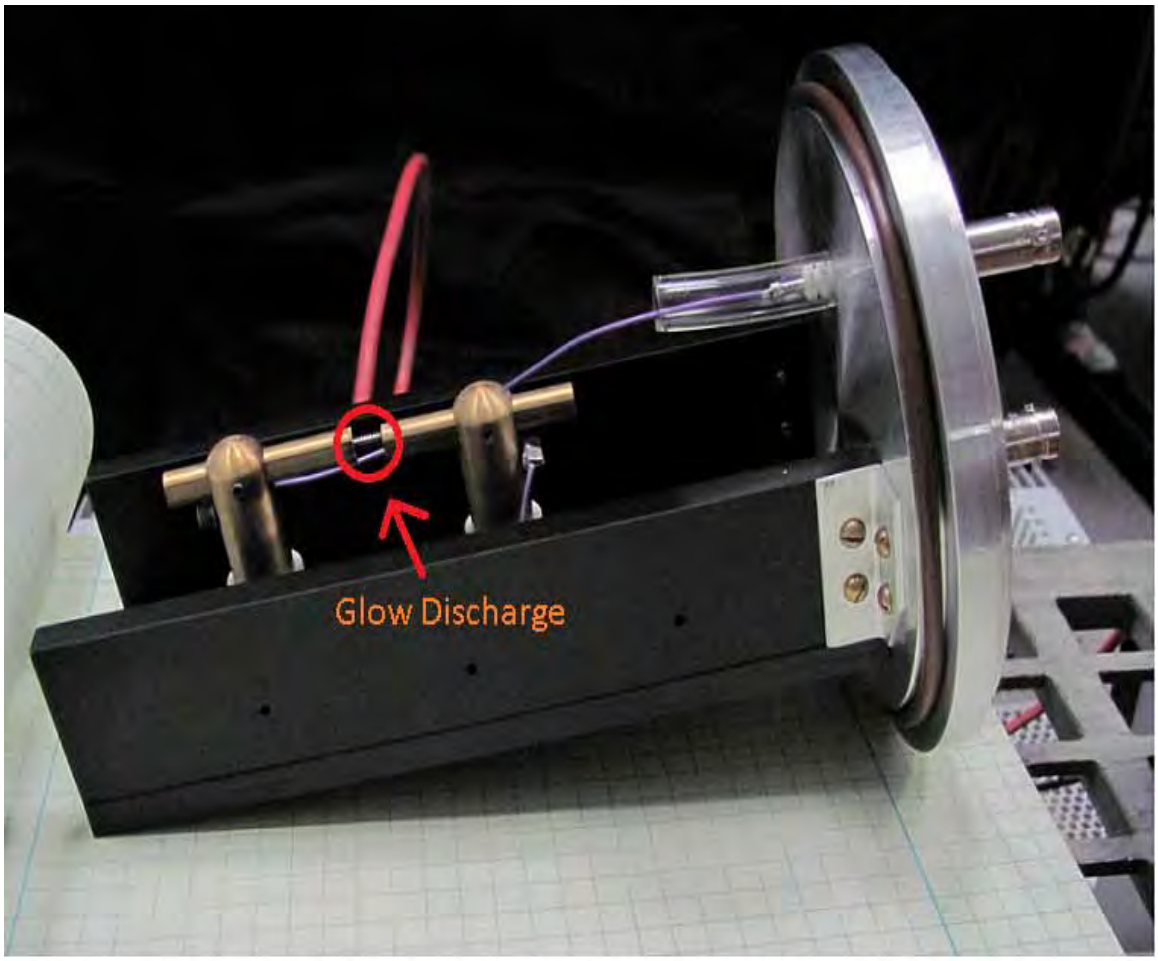

Figure 3 shows the electrode system. A) shows where the glow discharge takes place.

Also included in the set-up is a commercial camera, Canon Powershot SX120 IS.

The point of this prototype is to replicate conditions in a beam line. Tests were conducted to evaluate the lowest glow discharge current for which a visible signature can be detected with our camera. In order to decrease the current, the voltages on the electrodes were decreased at constant intervals.

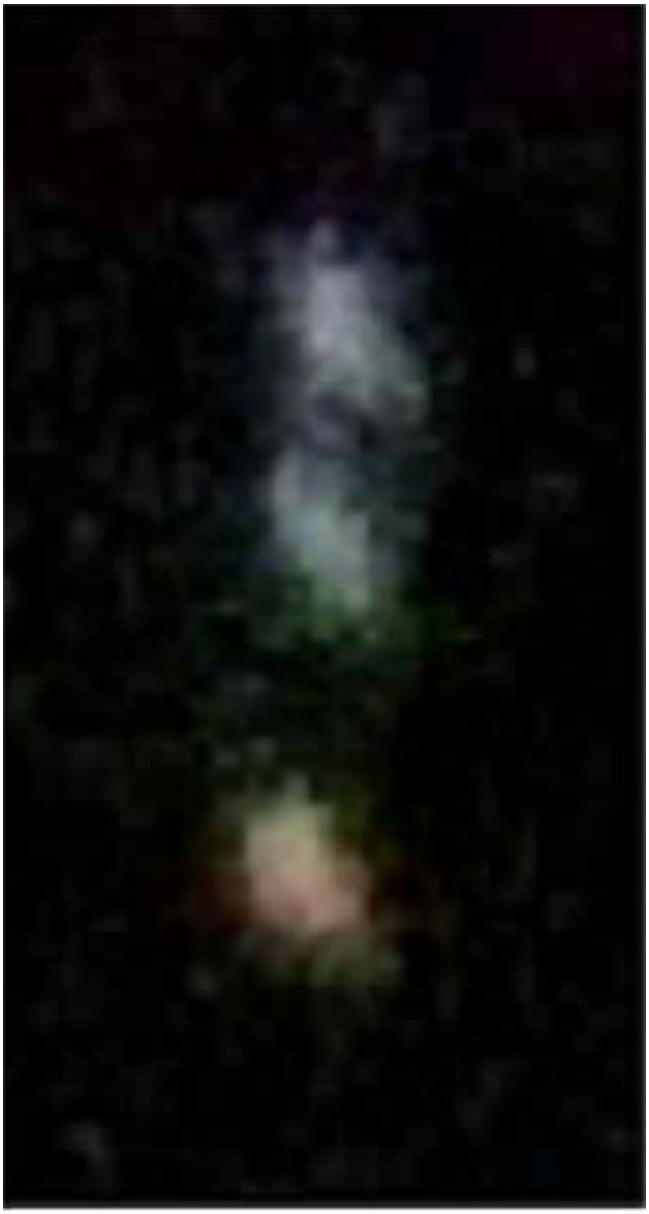

Figure 4 shows the glow discharge between 20 to 30 micro Amps.

Figure 5 shows the glow discharge at approximatly 130 micro Amps.

Results

The following tables show the minimum voltage and current for which the commercial camera was able to record the glow at two different shutter speeds.

July 17th 2013

Focus: 12 cm	shutter speed: 5 sec	Distance of electrodes: <0.006 in	Pressure: ≈ 2.4 e-5 Torr
Voltage (V) ± 10	Visable image (Y/n)	Current (μA)	iso: 1600
1000	y	27-30	
980	y	28 32	
960	y	32-34	
940	y	40 44	
920	y	28-32	
900	y (Very Faint)	20-24	
880	y	14-16	
860	y	12-14	
840	y	12-14	
820	n	9-11	
800	n	7-10	

Table 1 shows the minimum current reading at approximately 13 Amps that can still be viewed.

July 19th 2013

Focus: 12 cm	shutter speed: 4 sec	Distance of electrodes: <0.006 in	Pressure: ≈ 6.2 e-6 Torr
Voltage (V) ± 10	Visable image (Y/n)	Current (μA)	iso: 1600
1000	y	60-70	
990	y	45-55	
980	y	50-55	
970	y	30-40	
960	y	40-45	
950	y	30-35	
940	y	25-30	
930	y	25-35	
920	y	25-30	
910	y	25-30	
900	y	27-35	
890	y	12-22	
880	n	27-35	
870	n	20-25	
860	n	15-25	
850	n	10-15	
840	n	10-12	

Table 2 shows the minimum current falling between 12 to 22 Ampes.

Tests show that the sensitivity of a commercial camera is good enough to capture images of the glow discharge. This means that images of the glow can be viewed using a cheap camera. As a result the glow becomes fainter and fainter. However, most importantly tests show that the minimum current reading that is visible at approximately 13 micro Amps. This is very important and very good news because at Notre Dame the intensity of the 5U is 200 micro Amps. Since the 5U is able to reach over one order of magnitude higher than the minimum current reading, a non-interceptive beam monitoring at Notre Dame is a very good solution to the problem of melting profiling slits. Not only is it very important to current experiments at Notre Dame involving the 5U but with plans to construct DIANA. This result is even more important and beneficial when DIANA is completed because the highest intensity of 100 mA is four orders of magnitude higher than the test results.

Future Plans

Future plans are to test the prototype inside the beam line. Since the current reading is small compared to the intensity of the 5U a positive result will occur. Also, with the introduction of protons in the beam rather than electrons in the electrode system a visible interaction should occur. This is because the ionization power of the proton compared to the electron is greater. Further testing can be done using a more sensitive camera to see if the minimum current will decrease. If this can be verified then non-interceptive beam profiling will have a larger range of intensity in which it can be used.

CMS Upgrade Simulations

Edward Varty

2013 NSF/REU Program

Physics Department, University of Notre Dame

Advisors: Dr. Hildreth, Dr. Lannon

Abstract

Due to the planned upgrades to the luminosity of the Large Hadron Collider, the Compact Muon Solenoid is also planned to be upgraded. To account for the increased number of particles that will be produced, the Compact Muon Solenoid must have a more efficient method of filtering out uninteresting particles. This is done by the Level 1 Track Trigger, but the current trigger is not effective enough for the planned luminosity so a new method of separating particles is needed. Simulated particle tracks were analyzed by a trigger algorithm developed by previous REUs. The results of this algorithm were evaluated, and the algorithm was altered in order to increase the efficiency while decreasing the number of false particle tracks found. The current implementation of the algorithm is closer to what is required for the future hardware. There are still problems in the track finding. Some are inherent in the detector design, while a few are still problems with the algorithm itself, which will be studied in the future.

The Large Hadron Collider (LHC) is a high energy particle accelerator which seeks to probe new areas of particle physics by means of particle collisions. Protons are collided at an energy of several TeV. These collisions produce a wide variety of new particles which are analyzed to reconstruct the collision. In order to gather data, there are a variety of detectors at the LHC. My work is concerned with the Compact Muon Solenoid (CMS). During the planned LHC upgrades within the next decade, CMS will be improved, so that it can accurately take data from a much larger number of collisions which will take place after the LHC upgrades.

CMS is composed of four layers; three work to detect particles and one layer contains the magnetic field. The innermost part of the CMS detector is the tracker. It is constructed of concentric cylinders of silicon detectors with disks in the forward section. The tracker is positioned within a strong magnetic field which causes charged particles to curve, which is essential in analyzing particle tracks. In the geometry that I worked with, there are six layers of silicon detectors which are arranged in three

superlayers, each consisting of two layers of detectors. The geometry that I worked with is known as Long Barrel geometry and has no disks at the end. When a particle passes through one of these silicon layers, it interacts with the silicon, leaving a charge on the layer which creates an electrical signal, a "hit," which allows the position of the particle to be determined. The position of each hit is recorded in angle around the detector which is measured by phi, and distance along the length of the detector which is measured by z.

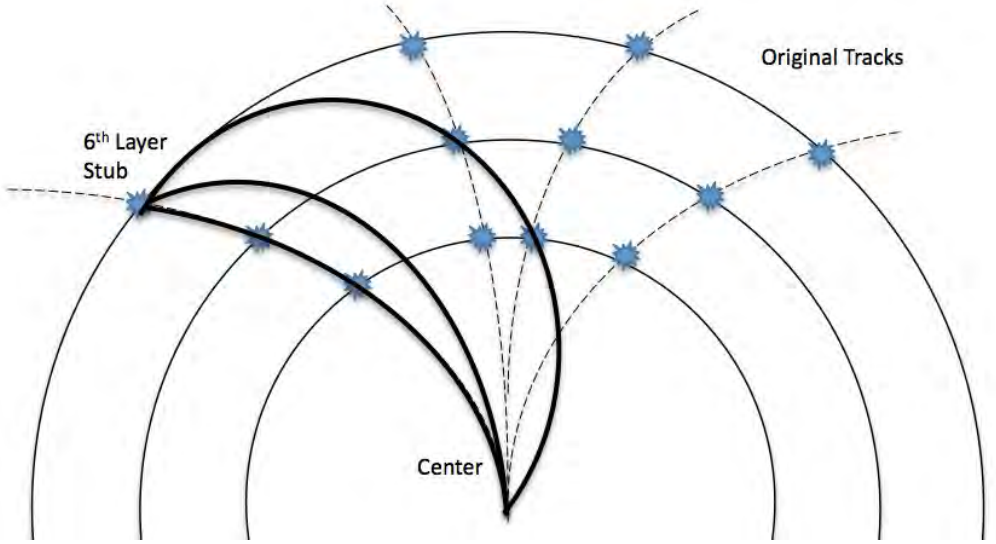

Figure 1: Cross section of barrel. This includes an illustration of the track finding function, including slop. Analysis of a Potential Tracking Algorithm for the SLHC Upgrade, Creager and Swift, 2012.

The Level 1 Track Trigger is designed to sort out uninteresting particles (low momentum) from interesting particles (high momentum), since significantly more data is produced than can be written. The trigger finds the momentum and position of particle tracks. Higher energy particle are considered more interesting, and their data is passed to secondary processing. The Level 1 Track Trigger must be capable of rapidly and effectively computing the momentum of particles due to the huge number of events.

The tracker does not directly measure the tracks of particles. It measures hits which are then built into tracks. Work has been done on an algorithm to accomplish this effectively. The goal of the algorithm is to find as many real particle tracks as possible.

To test the algorithm, simulated particle tracks are generated and pass through a simulated detector. These simulated events leave a trail of hits which exactly mimic the signal output of the tracker. The algorithm is then applied to these signals, and its performance can be analyzed. The algorithm is evaluated primarily by three statistics: efficiency, fake tracks, and multiple finds. The efficiency is the rate at which the algorithm locates real tracks and is defined as the ratio of tracks found to the number of generated tracks. A fake track is when the algorithm takes stubs from different tracks and determines that those stubs form a track which has no corresponding simulated track. Multiple findings are when the algorithm finds the same track more than once. An efficiency of 1 is ideal, and an efficiency of at least 0.9 is required. The algorithm would ideally find no fake tracks and find each track only once. In practice, efforts to raise the efficiency also tend to increase the number of fake tracks, so the algorithm must be analyzed to determine the best compromise between efficiency and fake tracks.

For the purposes of the algorithm, the possible momentum range, 0 - ∞ GeV, is divided into section called bins. The lower momentum (<50GeV) range is divided into bins with equal width in momentum while the higher range is divided into bins that are unequal in momentum but cover an equal width in curvature. The tracks are curved because there is a strong magnetic field present in the detector, as shown in Fig. 1. Curvature is essential in determining the momentum of a particle track because momentum, p, and curvature, K, are related by the equation:

$$p = \frac{Bq}{K}$$

where B is the magnetic field and q is the charge of the particle.

The algorithm begins by cycling through the sixth layer stubs. For each stub, the algorithm then cycles over the different bins. Every bin determines a range within which the other stubs must falls for the momentum to be in that range. All bins are tested, and bins that contain at least five stubs are considered tracks.

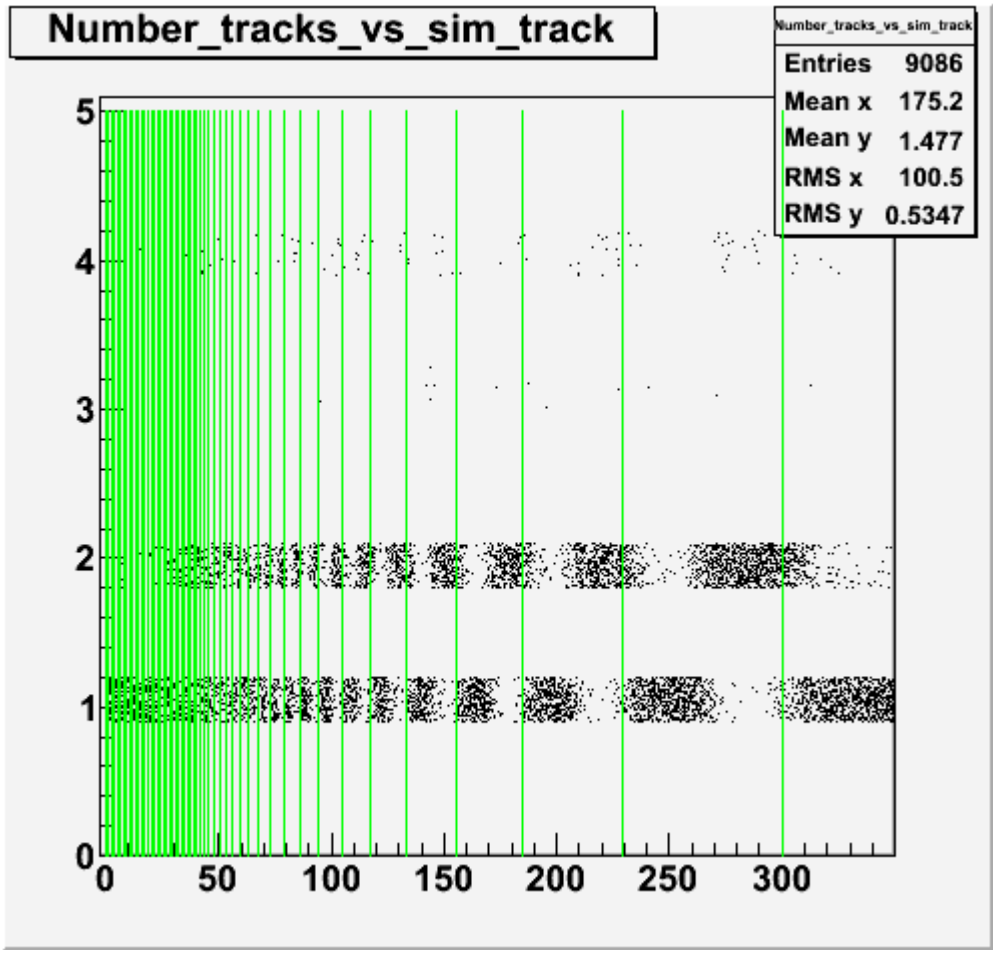

Figure 2: Green lines are bin boundaries. X-axis is GeV. Y-axis is number of tracks found.

This method works very well when the momentum of the simulated track is well within any bin. When the momentum is close to a bin edge, fluctuations in the particle path can lead to stubs being out of place slightly as the particle deviates from its ideal course due to interactions with the detector. This effect causes a decrease in efficiency at the bin boundaries, as neither bin has enough stubs to constitute a track.

In order to correct for this, the algorithm has “slop.” Slop is a slight extension of the range checked by the algorithm beyond what is expected without irregularities in particle paths, illustrated in Fig. 1. This allows the algorithm to catch stubs that might have been just outside of the appropriate bin. Slop is required to get up to the required efficiency, but too much slop leads to fake tracks. Thus, slop is aimed to be implemented in such a fashion that it increases efficiency without increasing fake tracks to an unacceptable level.

There are two methods by which slop has been implemented: in momentum and in phi. We implement the slop in momentum by simply altering the edges of the bins slightly to overlap each other.

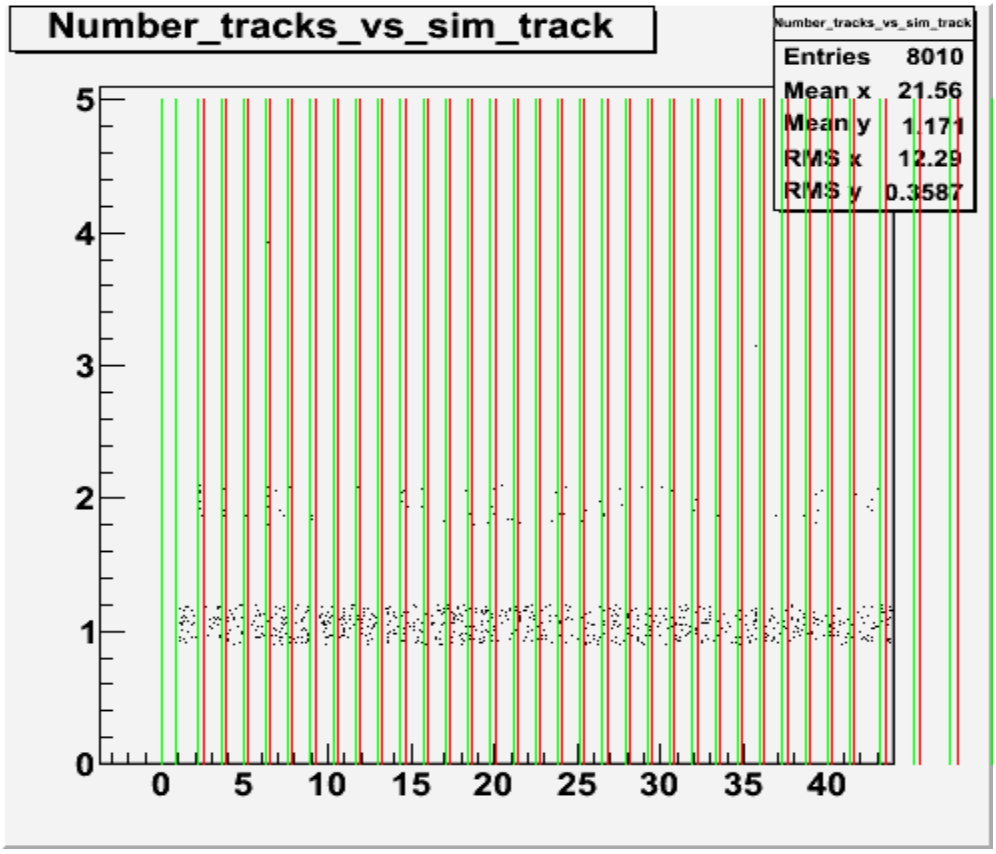

Figure 3: Red lines are upper bin edges, green are lower bin edges. Note the smaller space between the nearest red and green lines. This is the slop.

However, after debugging the previously developed slop method, it was found that momentum based slop always resulted in too many extra found tracks when compared with the achieved efficiency. The momentum slop is not favored, because, while it works well in code, it relies on a calculated quantity,momentum, which is not directly measured by the detector. The detector directly measures the angle, so that is the preferred implementation. Phi slop achieves the same efficiency as momentum slop but with fewer fake tracks and extra tracks.

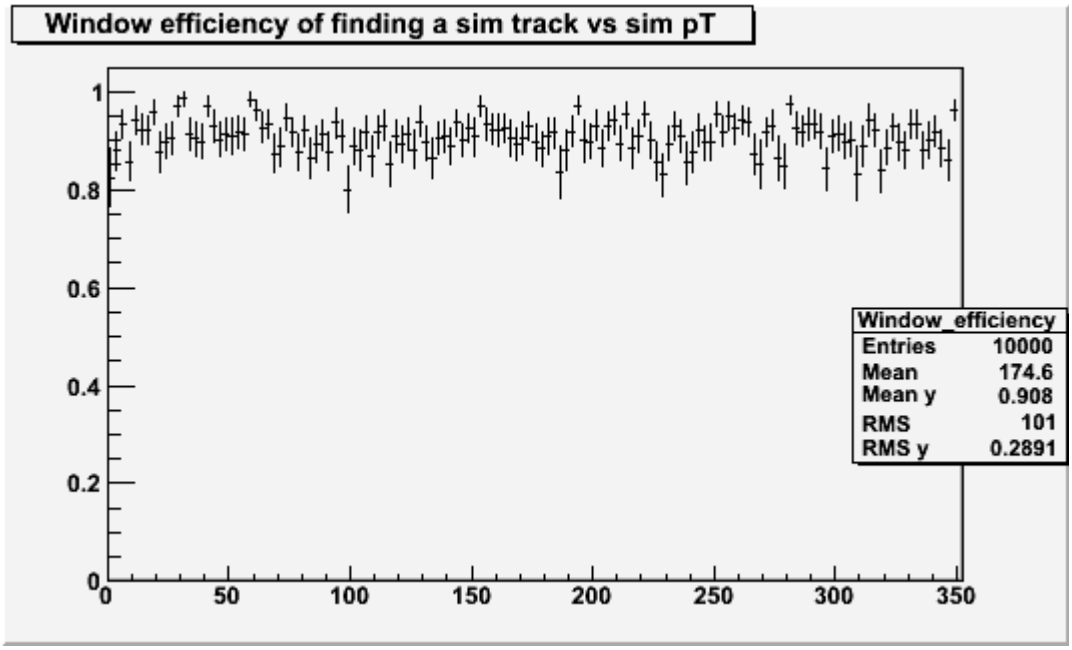

Figure 4: The efficiency of the old algorithm versus momentum.

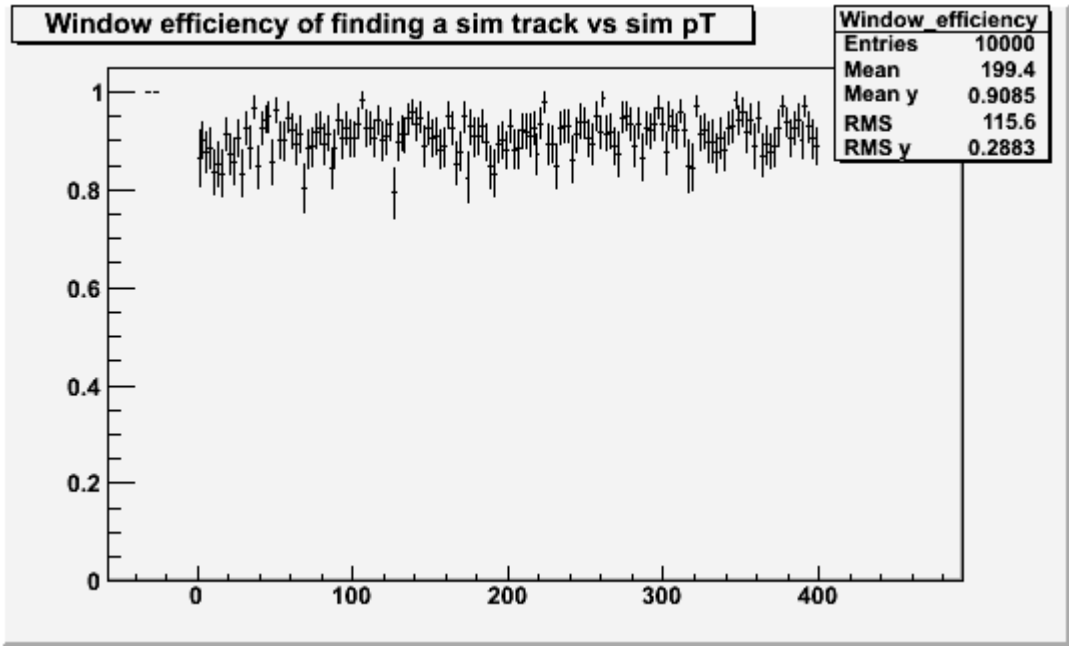

Figure 5: Efficiency of the new algorithm versus momentum. Note that it is about the same as the old algorithm.

The slop in phi is implemented by returning a slightly wider range of acceptable angles when the algorithm calculates the angle for a given momentum. This means that it is more resource intensive than the momentum slop which is a one time calculation (or a lookup table). The amount of phi slop should ideally be altered depending on the momentum of the bin being tested. Due to interactions with the detector, there is a spread in angle which depends on momentum. Many tracks were generated at

different momentum values, but the same phi value. These were then analyzed to determine the width of spread. The width decreases with momentum, as expected. There is roughly a factor of 10 between the width of stubs in 30GeV and 300GeV. Having the same phi slop size for all momentums does work, but efficiency should improve, if the spread width were to be taken into account. This is left for future students, but foundations have been laid that should allow for an easier analysis of this area. This approach to phi may be less feasible in the final detector, since calculations have to be performed for each stub and cannot be easily simplified. This may be alleviated simply by the inherent speed of FPGAs, but perhaps not. The current implementation of phi slop is not the only possible method, and other, faster, methods may be devised by future students.

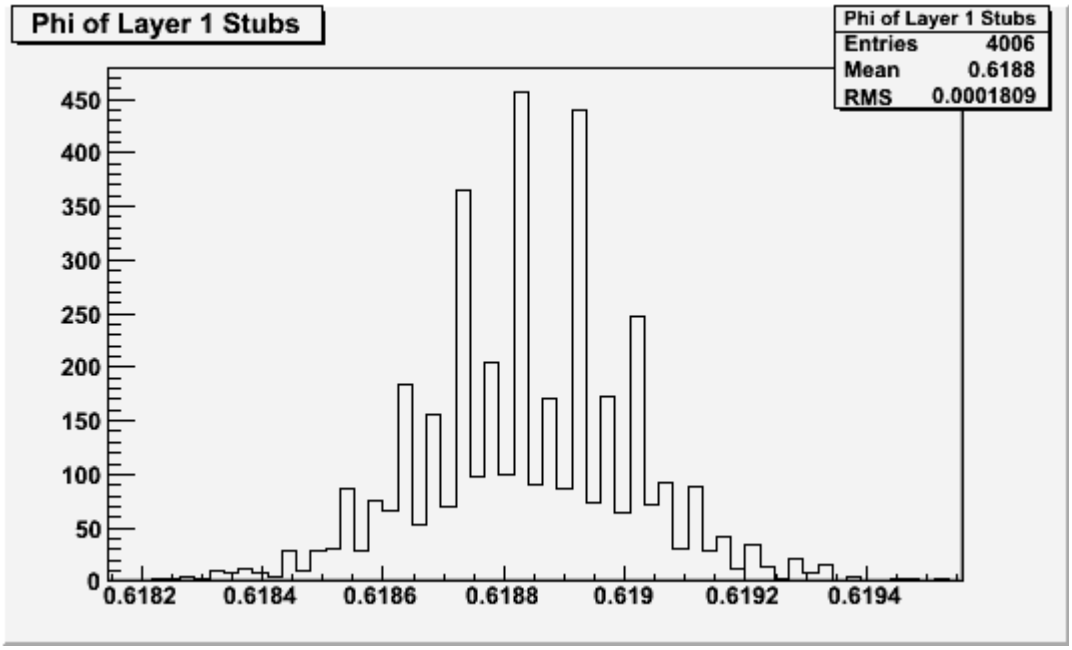

Figure 6: Spread of hits for 30GeV. X-axis is angle. Y-axis is number of hits.

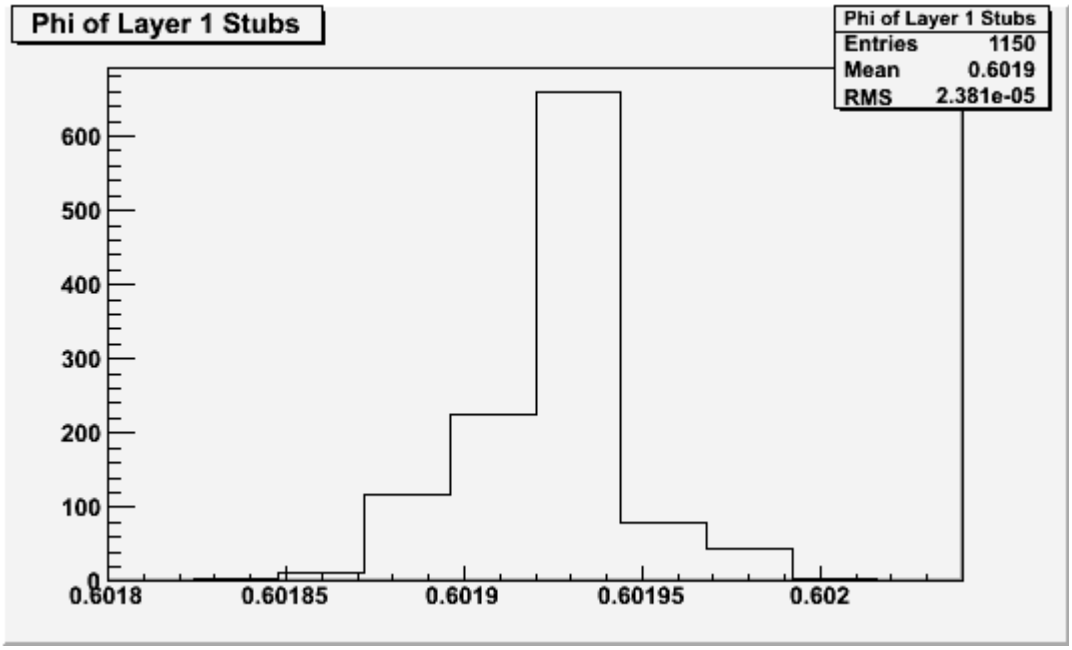

Figure 7: Spread of hits for 300GeV. X-axis is angle. Y-axis is number of hits.

The implementation of phi slop also produces a preferable distribution of extra tracks. Phi slop tends to produce only one track, except near bin boundaries where two and occasionally four tracks can be found. This is preferable to momentum slop, which could produce up to twenty found tracks near bin boundaries. These extra tracks are unavoidable for any version of slop, unless very computationally expensive methods are used.

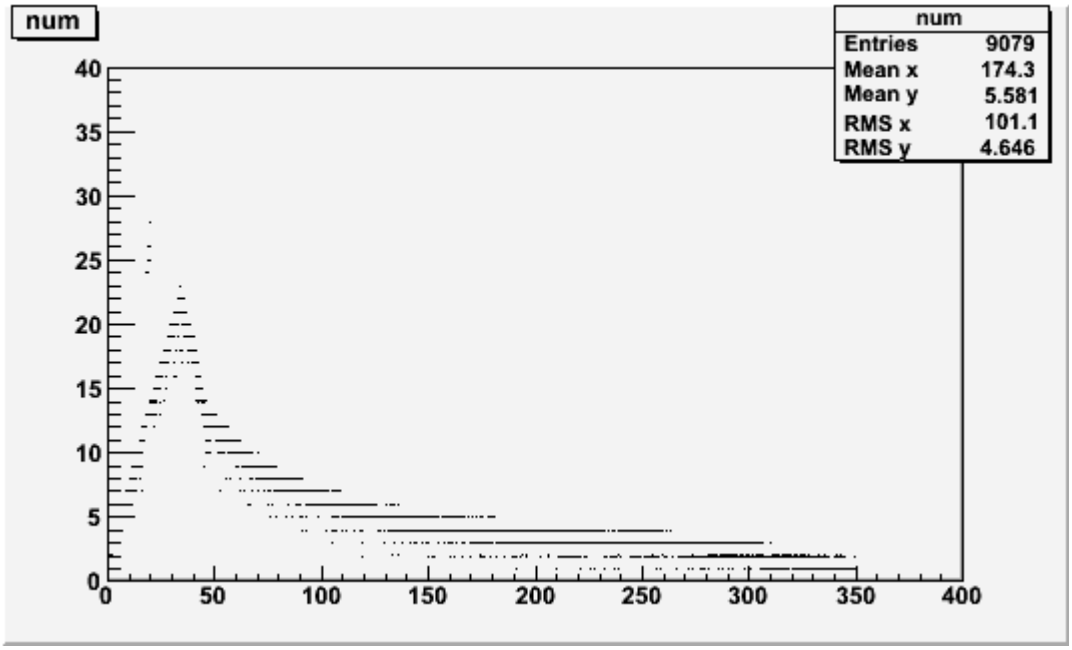

Figure 8: Number of tracks found versus momentum for old algorithm.

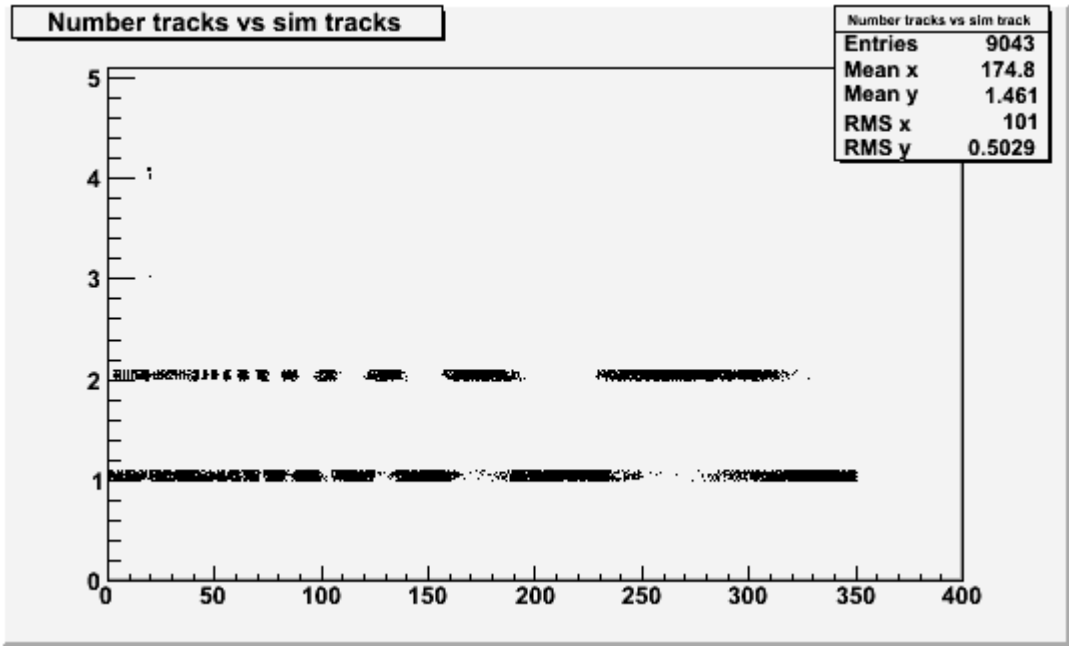

Figure 9: Number of tracks found versus track momentum for new algorithm. Note that the number of found tracks is consistently lower than the old algorithm.

Moving forward, the algorithm needs to be tested to find the ideal value of slop. An issue with the current implementation is that one particular value works very well, but deviation both above and below the current value severely reduce efficiency. The algorithm has also been tested almost exclusively with muons. Testing to ensure that it works for other particles is required. It is also possible that other particles would need a different slop value than muons. This would have to fixed were it to occur. Future work should give some thought to improving the speed of the algorithm or to implementing a version of slop that takes advantage of FPGA functionality.

Summary of CMS Minimum Bias Pythia 8 Tunes

Hanyi (Livia) Yi

2013 NSF/REU Program

Physics Department, University of Notre Dame

Advisors:

Dr. Steve Merenna, Fermilab

Professor Mike Hildreth, University of Notre Dame

Professor Kevin Lannon, University of Notre Dame

Abstract

Pythia 8 is a computer program designed to simulate the physics processes that occur during a high energy collision, such as collisions between protons or electrons. Upgraded from Pythia 6, however, the new version has not yet been enough tested and tuned for it to have reached the same level of reliability as the older one. Improving Pythia 8's performance in describing collider data involves two parts: first, adding new CMS analyses into Rivet, a toolkit for MC event generators and experimental data comparison, in order to expand the base of analyses to be compared to; second, running CMS analyses using Pythia 8 with different settings and compare the output data with real CMS data in order to get the most optimized global tune to describe collisions between protons. We use Professor-1.3.1 as a tuning instrument, and we come to the conclusion that the new tune provides a more accurate and reliable prediction for CMS collisions.

I Introduction

Event generators are software packages that generate simulated high-energy collision events. It is important to understand why they play such a critical role in high-energy physics. They share the same event reconstruction framework and subsequent physics analysis with the real machines such as LHC and Tevatron. Therefore, they help us gain knowledge of what may be going on in the real colliders by demonstrating to us how an original input is developed and distorted under relatively controlled physical conditions. Conversely, because of the fact that the event generators are programmed based on current knowledge of particle physics, the differences between the output data we get from them and the real LHC data shows to us the deficiencies of the current physics models and how we might improve them.

Pythia 8 is one of the major Monte Carlo event generators used for simulating LHC events. Monte Carlo methods rely on repeatedly generating random numbers running simulations numerous times in order to get statistically optimized outcomes to solve a problem. In Pythia, random numbers are used to make choices about what is going to happen next in order to reproduce the quantum mechanical probabilities for different results. The user interacts with Pythia in three stages: he first gives Pythia an initial setting where the tasks are to be performed; then Pythia runs by generating simulated events based on the specified conditions; after it finishes running, the final statistics are made available. (Torbj¨orn Sj¨ostrand, Stephen Mrenna and Peter Skands, October 2007)

To tune Pythia 8 means to refine Pythia 8 predictions of the particle physics

To Table of Contents

“truth”. Here, the "truth" is a list of particles produced from the proton-proton collision that will then propagate through the CMS detector. We use two major comparison tools to tune Pythia 8 – Rivet and Professor. Rivet is a validation system for MC generators. It produces plots from a piece of MC generator analysis code. In other words, one only needs to write the code once and the code can be used to validate and compare every generator that is able to simulate it. It makes sure that consistent comparisons are always done, which is important when trying to understand one generator compared to another one. It is useful for tuning because its analysis code and reference data can be used as an input.

We also use Professor as a major tuning instrument. Its advantage exists in its ability to interpolate the results of an analysis based on a generated grid of data. There are so many different settings that need to be tuned that without an automated program like Professor, one would need to generate an infinite number of MC samples to find the optimal settings. But once we run Pythia 8 with different settings and feed the output data to Professor, it is able to look for the optimization without automatically.

II Pythia 8 Tuning with regard to ALEPH Experiment

ALEPH was an experiment that ran at CERN before the LHC using the LEP collider. Although our main goal is to use data collected by the CMS experiment at the LHC, ALEPH experiment is a useful starting point because it has been used in tuning Pythia 6 for so long. We first reproduced analysis ALEPH_2004_S5765862 within the CMS framework, and tested Rivet comparison machinery and Professor tuning tools

by finding Pythia 8's optimized parameter set with respect to the variable pT(in).

The pT(in) spectrum is the projection of the transverse momentum of charged particles onto the so-called "thrust axis" of the event, which is the axis of maximum energy flow, and it can be demonstrated more clearly by the following graph:

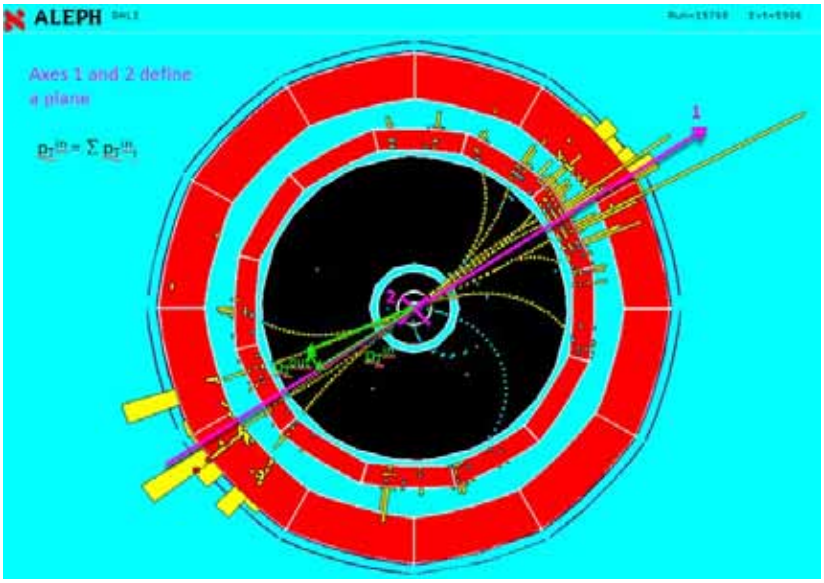

(Michael Hildreth, June 2013)

It is one of the variables that has always been hard to describe, so our goal is to produce a gradient map of pT(in) versus the Pythia 8 parameters. We did multiple runs, varying the parameters of the default tune one-at-a-time. In particular, we varied the following parameters each by 10% up and down, except for TimeShower:alphaSorder, which is either 1 or 2. We used Rivet to do statistical comparison between the real ALEPH data and MC data. The first piece of information we want is whether any of these settings improve the pT(in) description. The chi^2 map is produced for this purpose (the bolded ones are the default settings):

pT(in), E(CMS) = 189GeV

Chi^2/n	**TimeShower:**	TimeShower:

	alphaSorder = 1	alphaSorder = 2
StringPT:sigma = 0.30096	7.74	
StringPT:sigma = 0.304	**7.96**	
StringPT:sigma = 0.3344	6.88	
StringZ:aLund = 0.27	7.55	
StringZ:aLund = 0.33	8.65	
StringZ:bLund = 0.72	9.05	
StringZ:bLund = 0.88	6.73	
TimeShower:alphaSvalue = 0.12447	20.10	
TimeShower:alphaSvalue = 0.1383	**7.96**	
TimeShower:alphaSvalue = 0.15213	28.54	
TimeShower:alphaSvalue = 0.10620		63.77
TimeShower:alphaSvalue = 0.1180		22.93
TimeShower:alphaSvalue = 0.12980		10.95
TimeShower:pTmin = 0.36	7.19	20.73
TimeShower:pTmin = 0.40	**7.96**	
TimeShower:pTmin = 0.44	7.83	20.73
TimeShower:pTminChgQ = 0.36	7.97	
TimeShower:pTminChgQ = 0.40	**7.96**	
TimeShower:pTminChgQ = 0.44	8.20	

pT(in), E(CMS) = 189GeV, TimeShower:alphaSorder = 1

Chi^2/n		StringPT:enhancedFraction										
		0.0	**0.01**	0.1	0.13	0.15	0.2	0.25	0.3	0.4	0.5	1.0
StringPT	1.0			8.20	8.20	8.20	8.20	8.20	8.20	8.20	8.20	
:enhance	**2.0**	8.20	**7.96**	6.71	6.41	6.54	7.82	8.77	10.55	15.46	22.11	64.42
dWidth	3.0			7.23	8.42	9.68	14.68	20.56	28.84	45.87	66.84	
	4.0			8.99	12.41	15.61	25.25	37.89	51.99	83.26	117.90	
	5.0			11.46	17.56	22.84	37.24	53.56	74.78	119.37	165.05	
	6.0			14.31	23.07	29.42	49.78	73.47	98.56			
	7.0			17.23	26.93	35.73	60.38	88.37	119.11			
	8.0			19.81	32.41	42.04	70.25	101.31	136.23			
	9.0			21.92	36.58	47.33	79.59	113.94	153.90			
	10.0					52.72	86.72	125.96	167.57			

The two sensitive parameters we see are StringPT:enhancedFraction and StringPT:enhancedWidth. We increased the parameters in small steps of 0.1 to see the change in chi^2. It turns out that the chi^2 appears to be the smallest when StringPTenhancedFraction=0.13 and StringPT:enhancedWidth=2.0.

Furthermore, we also want to understand how the shape changes. For this we

check the ratio plots.

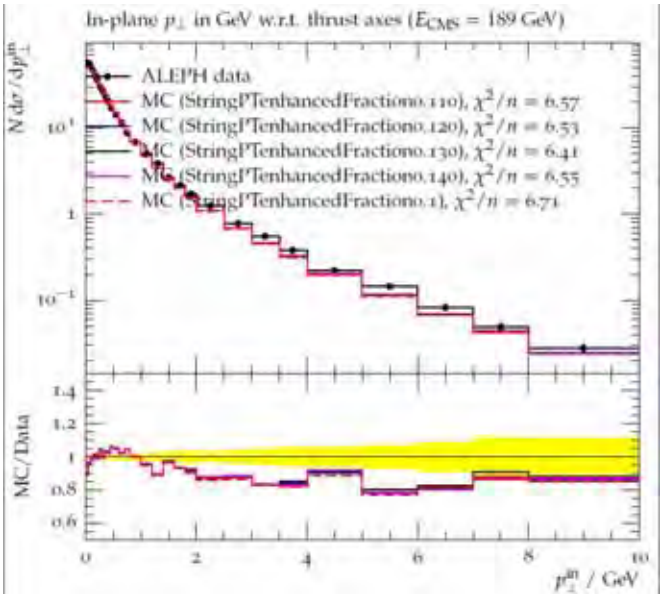

However, because Rivet requires us to manually change parameter settings and run events, there could certainly be promising parameter sets that we missed. That is where our second tool comes in – the Professor project. Professor is relatively automated and can be used to do both full-scale tuning and local tuning.

We ran a 2-D grid with the parameter StringPT:enhancedFraction from 0.00 to 0.16 and StringPT:enhancedWidth from 1 to 8. Professor's interpolation told us that if we fix Fraction at a very small value, the chi^2 decreases when I increase Width to a certain extent. The minimum professor found was F=-0.00136, W=6.86.

We then used Rivet to test if Professor gave the right interpolation. Since Fraction can't be negative, I fixed it at F=0.01 (which is its default value) and increased Width. The comparison plots can be found below. We did not go look for the exact minimum because tuning to the ALEPH data was not a priority, but we could see the trend.

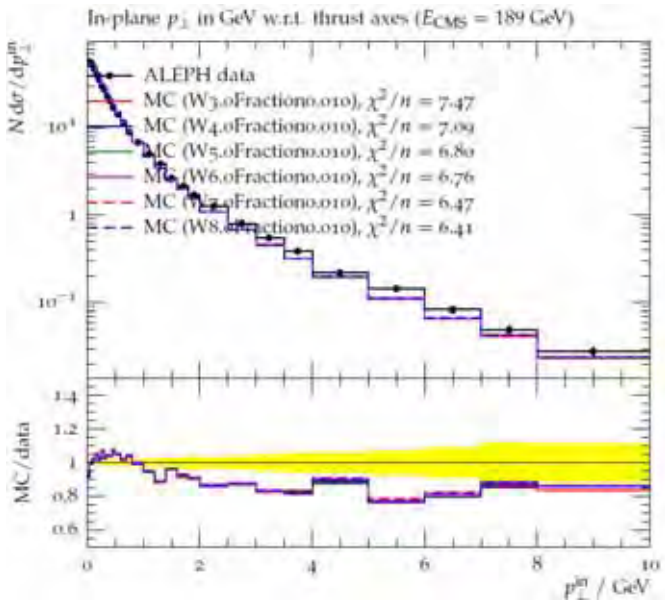

III Pythia 8 Tuning with regard to CMS Experiment

As I described earlier, we found a seemingly most-optimized parameter setting, and then Professor found us a new minimum, which we manually tested its validity using Rivet comparison tools. We consider Professor has proved its . We also took advice from *Summary of ATLAS Pythia 8 tunes*, in which the ATLAS Collaboration presented the latest ATLAS[1] Pythia 8 minimum bias and underlying event tunes.

We picked three analyses from CMS experiments database: CMS_QCD_10_006, CMS_QCD_10_010, and CMS_QCD_10_024. They are all CMS measurements of the underlying activities in the scattering processes in proton-proton collision. "Underlying" means the "soft" (e.g. low momentum") part of the collision that happens because the two protons are breaking up. Although the "hard" part of the collision depends on exactly what particles were produced, the soft, underlying piece is the same for all collisions (i.e. universal).

[1] Another detector at the LHC

Tune: pp 7 and Tune: pp 8 are both ATLAS Pythia 8 tunes. In fact, the ATLAS Collaboration did five tunes in total:

PDF	pT0Ref	ecomPow	a1	reconnectRange	Tune:pp
Minimum-bias tunes: A2					
CTEQ 6L1	2.18	0.22	0.06	1.55	7
MSTW2008 LO	1.90	0.30	0.03	2.28	8
Underlying event tunes: AU2					
CTEQ 6L1	2.13	0.21	0.00	2.21	9
NNPDF 2.1 LO	1.98	0.18	0.04	3.63	–
MSTW2008 LO	1.87	0.28	0.01	5.32	10
NNPDF 2.1 NLO	1.74	0.17	0.08	8.63	–
CTEQ 6.6	1.73	0.16	0.03	5.12	–
CT10	1.70	0.16	0.10	4.67	11
MSTW2008 NLO	1.51	0.19	0.28	5.79	–
MRST2007 LO*	2.39	0.24	0.01	1.76	–
MRST2007 LO**	2.57	0.23	0.01	1.47	–

Table 5: Tuned MPI parameters for the A2/AU2 Pythia 8 tunings.

We did a simple rivet comparison of the CMS measurements with the two ATLAS tunes, and Tune: pp 7 appears to behave better in general for CMS analysis. Therefore, we focused on tuning Tune: pp 7 for now.

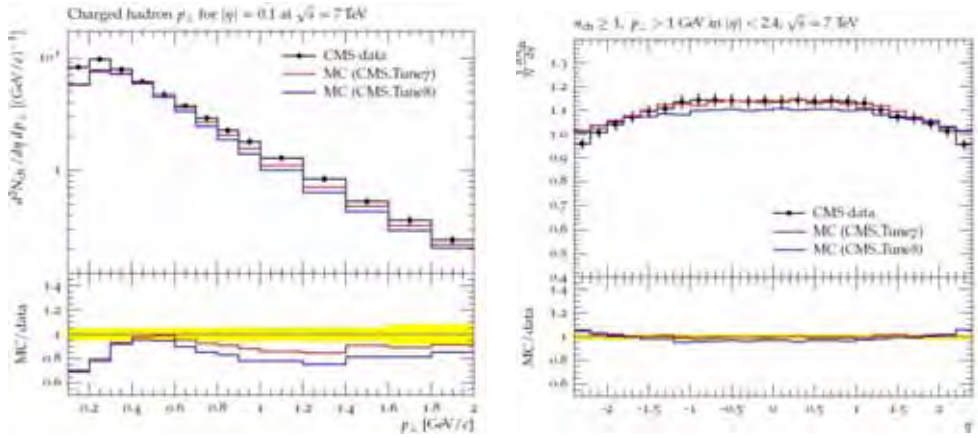

The parameters we tuned are MultipleInteractions:pT0Ref (subsequently referred to as pT0Ref), MultipleInteractions:ecmPow (subsequently referred to as ecmPow) and MultipleInteractions:a1 (subsequently referred to as a1). We ran a 5*6*5 grid and fed the output data to Professor, with pT0Ref varying through 2.16, 2.17, 2.18, 2.19

To Table of Contents

and 2.20, ecmPow varying through 0.19, 0.20, 0.21, 0.22, 0.23 and 0.24, and a1 varying through 0.04, 0.05, 0.06, 0.07 and 0.08.

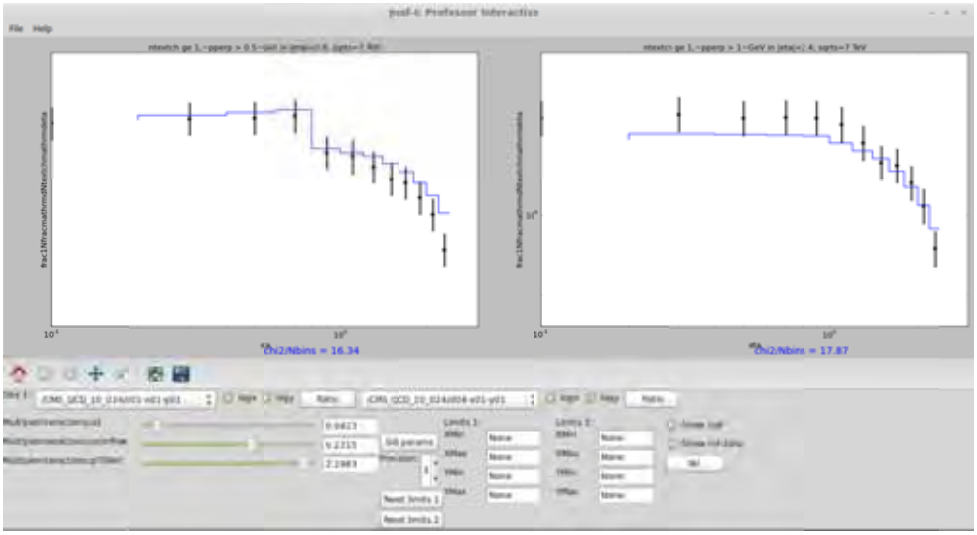

The optimization Professor found with the goodness of fit calculated turned out to be:

Parameter	Value
MultipleInteractions:pT0Ref	2.171734e+00
MultipleInteractions:ecmPow	2.045149e-01
MultipleInteractions:a1	4.024240e-02

Goodness of fit: 2.93e+04; Ndf: 602; Goodness of fit/Ndf: 4.87e+01

IV Summary

In this paper I have presented a new CMS tune of Pythia 8 event generators. The comparison between this new Pythia 8 tune and Tune: pp 7 can be found below:

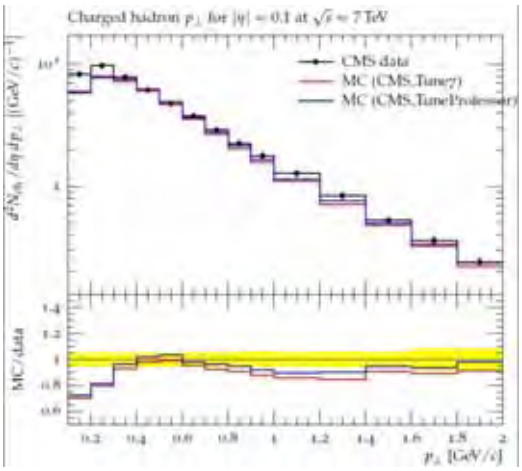

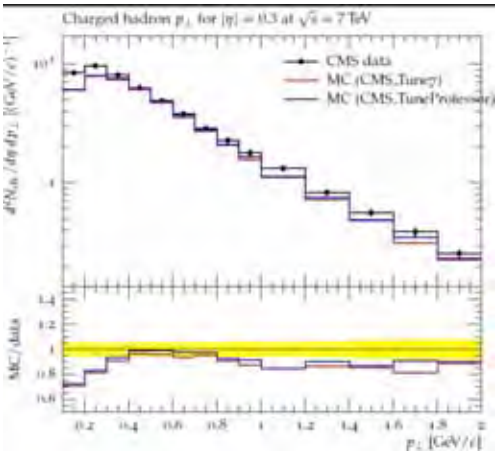

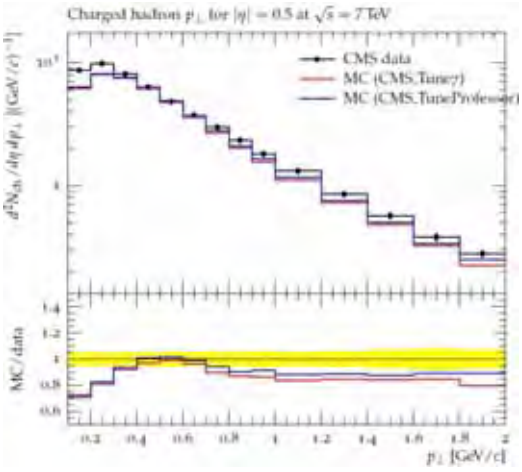

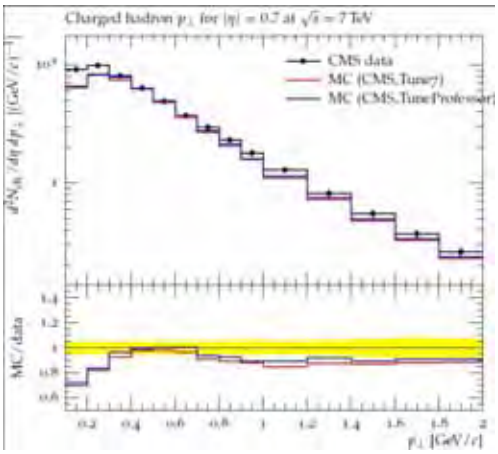

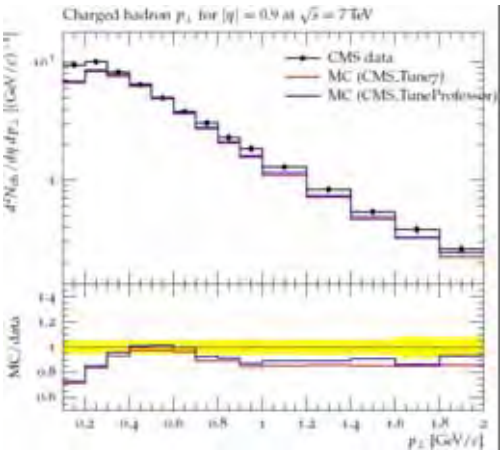

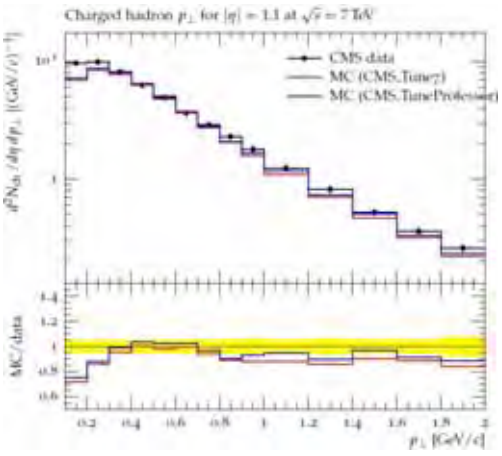

To Table of Contents

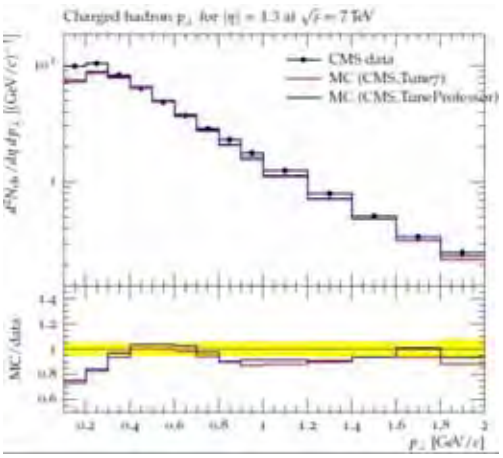

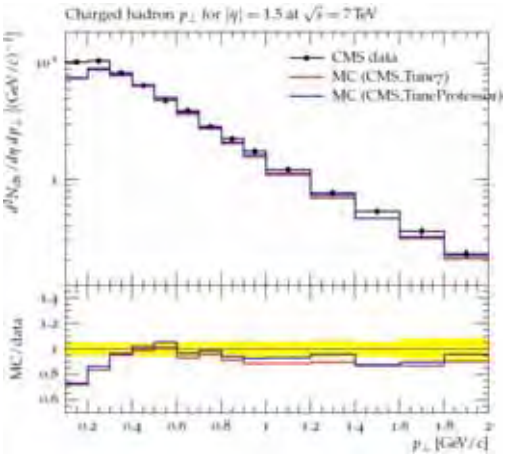

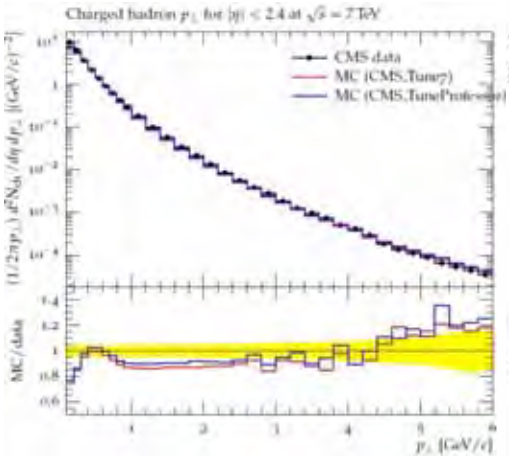

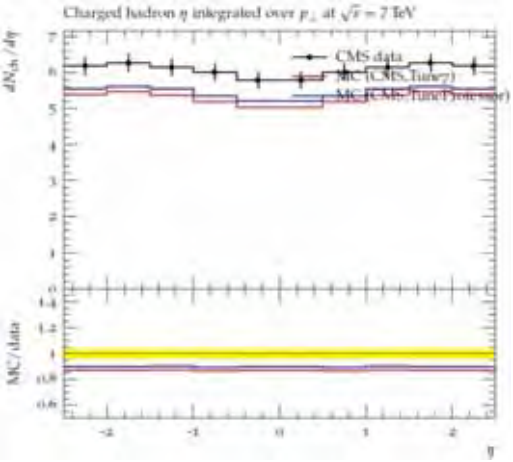

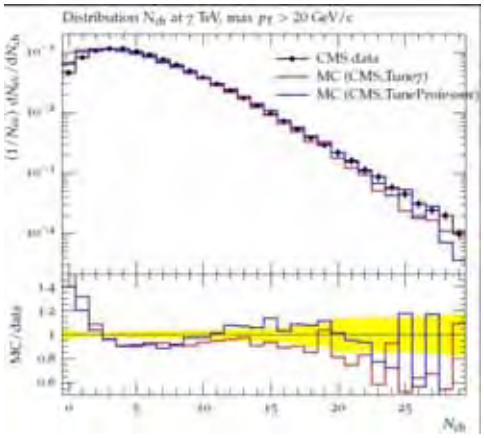

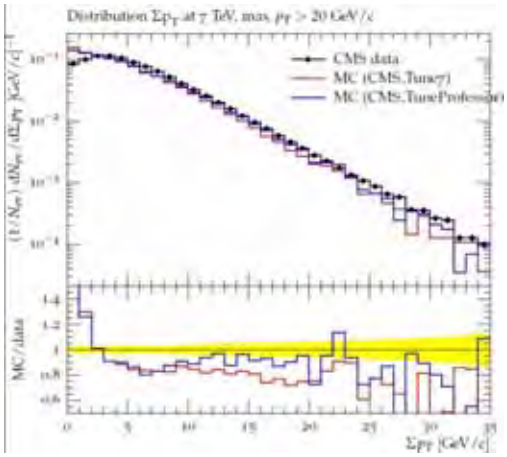

In the meantime, we have also coded up a new CMS analysis –

To Table of Contents

CMS_QCD_10_029 and put it into Rivet, for the purpose of benefiting future generator comparison and generator tuning. The work we have done this summer is just a beginning. There are many more data sets to compare and parameters in Pythia to be tuned. We have already started looking at additional measurements, and we will try to do more extensive tuning in the future.

References

Torbj¨orn Sj¨ostrand, Stephen Mrenna and Peter Skands, *A Brief Introduction to Pythia 8.1*, CERN-LCGAPP-2007-04, FERMILAB-PUB-07-512-CD-T, LU TP 07-28, October 2007

Torbj¨orn Sj¨ostrand, *Monte Carlo Generators*, hep-ph/0611247, CERN-LCGAPP-2006-06, November 2006

The ATLAS Collaboration, *Summary of ATLAS Pythia 8 tunes*, ATL-PHYS-PUB-2012-003, August 22, 2012

Constructing and Testing a Beam line for 5U Accelerator and Germanium Gamma Ray Detector Tests

Hua Zhang

2013 NSF/REU Program

Physics Department, University of Notre Dame

Advisor: Michael Wiescher

Abstract

The 5U accelerator at the Nuclear Science Laboratory is used to produce charged beam of particles with high intensity, which is over 100uA, and with voltage up to 5MV. An evacuated beam line provides an obstruction free path through which the beam travels. Various devices along this beam line are needed to optimize transmission of the beam from the source to the target. And the latest commissioning tests will be presented. High Purity Germanium Detectors are used to detect gamma rays with high energy resolution. Data are collected from the detectors using a multi channel analyzer, and then analyzed with energy calibration and efficiency calculation. The newly constructed Georgina Array has been tested using a selection of known and unknown gamma ray sources.

Introduction

The 5U accelerator constructed last year consists of creating charged atom particles and producing electric fields to accelerate them. Different from the Tandem Accelerator which has been serving for several decades, the 5U accelerator produces charged beam of particles with high intensity, which is over 100uA, and with voltage up to 5MV. Investigation in experimental nuclear astrophysics will be carried out using beams of energetic ions produced by electrostatic accelerator，in order to simulate reactions in stars.

An evacuated beam line provides an obstruction free path through which the beam travels. Various devices are needed for the purpose of conveying the ion beam over this path with the maximum efficiency. At the same time, the path with vacuum also

reduces collision between charged particles with other impurity particles. There are 4 bottles connected to the source, which is at the top of the accelerator, and the content can be changed.

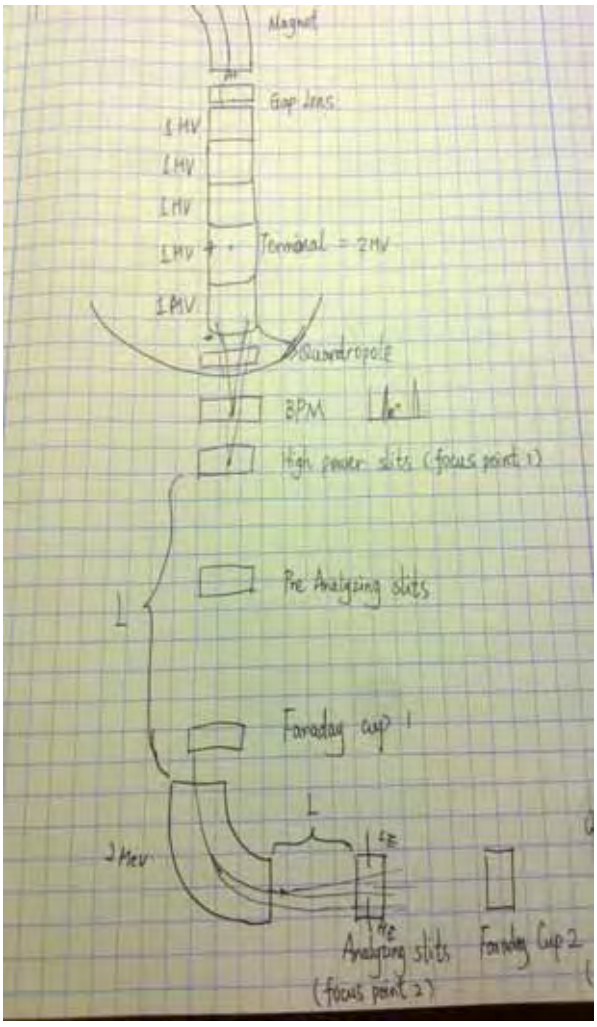

In testing the beam line, four kinds of gas sources are used, which are hydrogen, helium, oxygen and argon. When one source is used, atomic particles with different charges are created. Then beam with different charges is selected by a magnet regarding momentum over charge ratios. By testing different beams, we can keep an account of the intensity, stability and beam position.

After accelerated，the beam gets into the path and goes through a BPM(Beam Profile Monitor), which allows us to measure the size and shape of the beam without stopping it. Followed are high power slits and low power slits, both of which are created by four flexible metals. These metals can be adjusted and the distance of the narrow path is determined. When the beam goes through these slits, currents on four sides are detected and showed on

the monitor. By checking the position of the slits and keeping a balanced current on symmetric sides, we can have the rough size and shape of the beam. With two sets of slits, the beam is conformed to go perpendicularly into the magnet. With the help of BMP and the slits, we know the shape of the beam and where the beam focuses and defocuses, thus making the high intensity beam narrow and perpendicular. The purpose of the analyzing magnet is to select charged particles with certain energy. $\frac{mv^2}{r} = qvB$, r is the radius of the magnet, and B is the magnet field intensity, so mv/q=Br, and the particle energy $E=\frac{1}{2}mv^2$. When we change the B, we let particles of certain energy pass.

After bending in the magnet, the edge of the beam hit the high/low energy slits. By balancing the currents on the two slits, we make the beam travel in the center of the path. There are two faraday cups in the beam line, one is before and the other is after the analyzing magnet. A faraday cup is a metal cup designed to stop charged particles in vacuum. The current on it can be measured and used to determine the exact intensity of the beam.

During the test, we have the accelerator working on the gvm mode, which is to keep the voltage of the terminal stable, but real experiments require the beam energy to be stable, which is the function of slit mode. In slit mode, the terminal voltage changes if the current on high/low energy slits is not equal, thus changing the energy of the beam and keep the two currents equal.

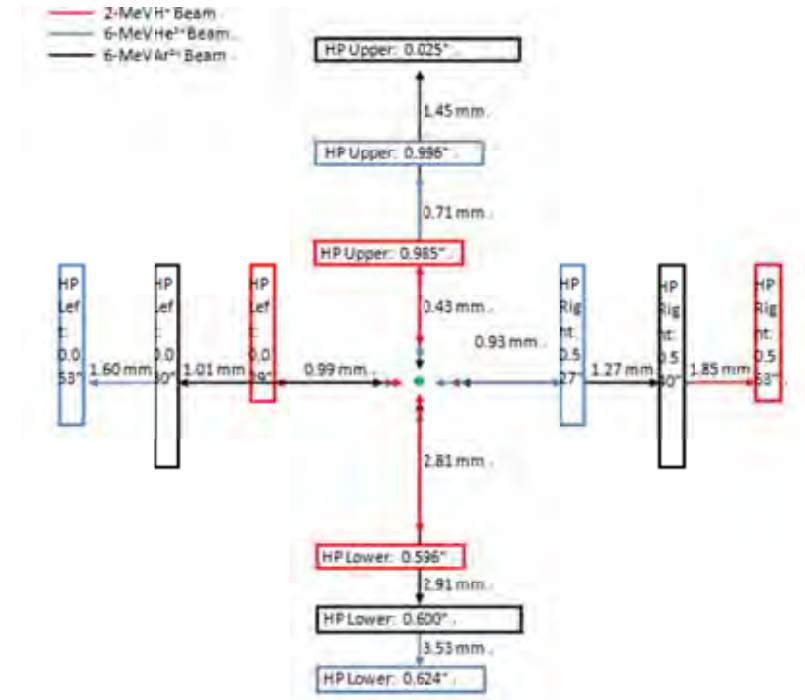

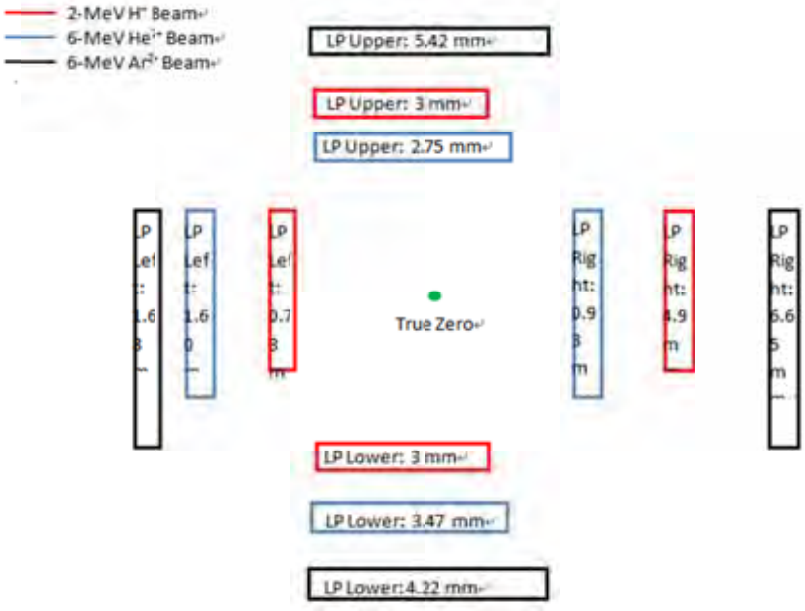

Above are the results of the slits position when we have H^+at 2MeV, He^{2+} at 6MeV and Ar^{2+} at 6MeV. The first one is for high power slits position, when current on each slit is 10% of the full current. The second one is for low power slits, when current on each slit is 10% after the beam goes through the high power slits.

From the results we can see the shape and size of the beam, and that beam directions shift slight off the mechanical zero point, which is not precise. And we will test more beams to find a more accurate zero position for the slits.

“Germanium detectors are semiconductor diodes having a P-I-N structure in which the intrinsic region is sensitive to ionizing radiation”. Because of the small bandgap of germanium, room-temperature operation is impossible because of the large thermally-induced leakage current that would result, which destroys the energy resolution of the detector. Liquid nitrogen, which has a temperature of 77K, is used to cool the detectors. “The detectors are mounted in a vacuum chamber which is attached into a LN2 Dewar”.

“When photons interact with the sensitive material within the depleted volume of a detector, charge carriers are produced and are swept away by the electric field, which is created by reverse bias. The charge, which is proportion to the energy of the photon interacted with the material, is converted into a voltage pulse by an integral charge-sensitive amplifier”.

Data are collected from the detectors using a multi-channel analyzer, and then analyzed with energy calibration and efficiency calculation. The newly constructed Georgina Array has been tested using a selection of 7 gamma sources. For the first two sources, 60Co (5.2 year) and 137Cs (30 year), we have the activity on 4/1/1981. 60Co is 11.59uCi and 137Cs is 10.95uCi. 11.59uCi=428830 decays/second, 10.95uCi=405150 decays/second. According to the exponential decay of radioactive

source $A_2 = A_1 e^{-\ln 2 * t/T}$(t stands for the time span, T stands for the half life of the isotope). So we have 60Co at 6121 decays/second, and 137Co at 191822 decays/second now.

The first picture below shows the spectrum of 60Co we collected. According to the decay scheme of 60Co, most peaks in the spectrum are background, and we only look at the peaks at 1173keV and 1332keV. The second picture comes from the spectrum of 137Cs. It shows the peak at 661keV after zooming in and the fit integral stands for the counts the detector collected.

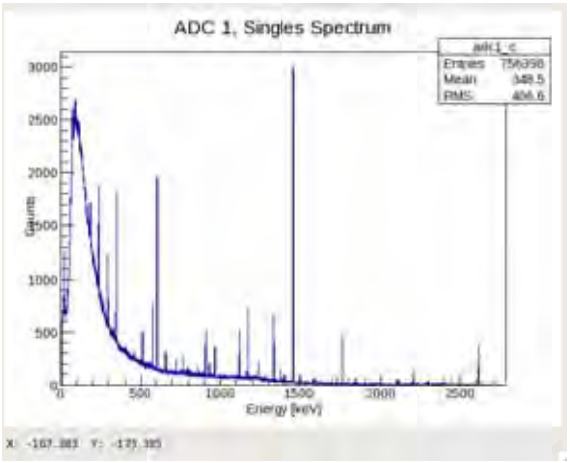

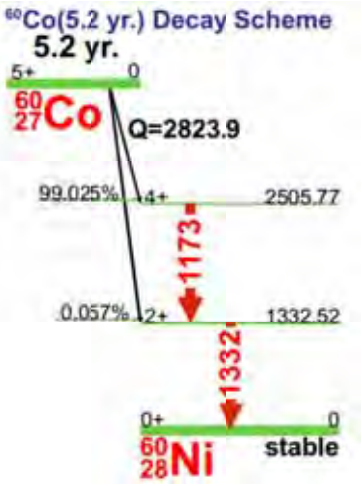

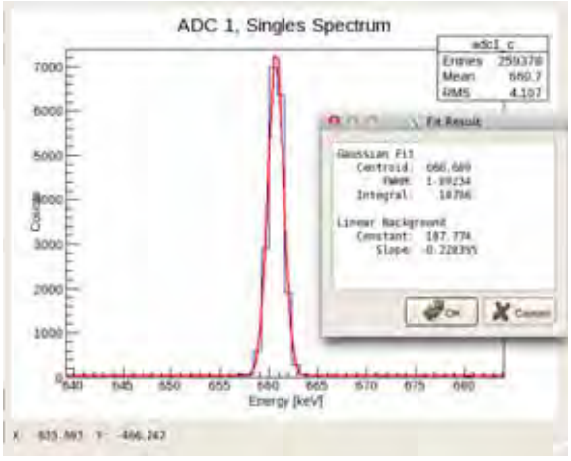

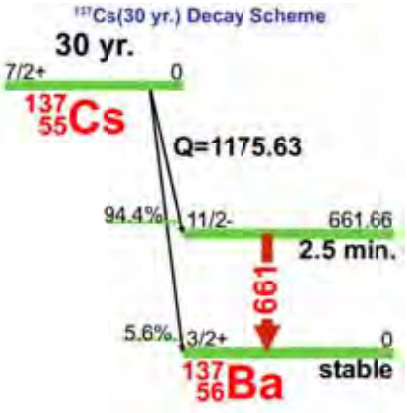

By studying the spectrum of 137Cs, we can identify peaks of the background. Sample 3,5and 7 has the same characteristic peaks, which are at 122, 136,834, 846, 1037,

To Table of Contents

1238, 1771 and 2598keV. By comparing them with decay schemes of many isotopes, we find that they consist of 57Co (271 day), 54Mn (312 day) and 56Co (77 day). Sample 6 has a peak at 88keV, which indicates the isotope to be 109Cd.

By calculating the two peaks of 60Co and one peak of 137Cs, we have three points on the efficiency curve. Efficiency=（integral/time）/(intensity*actual decay counts). When detecting gamma rays of different energies, the efficiency varies. And we have several points on relative efficiency curve due to sample Eu152.Relative efficiency=（integral/time）/intensity. Then we calculated the counting error, which is $\sqrt{N}$ and looked for intensity error, thus calculating the absolute efficiency error. We fit the relative efficiency curve, which is in the form of : $ln\ (\varepsilon) = \sum_{n=0}^{k} An * ln(E)^k$ and normalize it to the absolute points and fit an absolute efficiency curve.

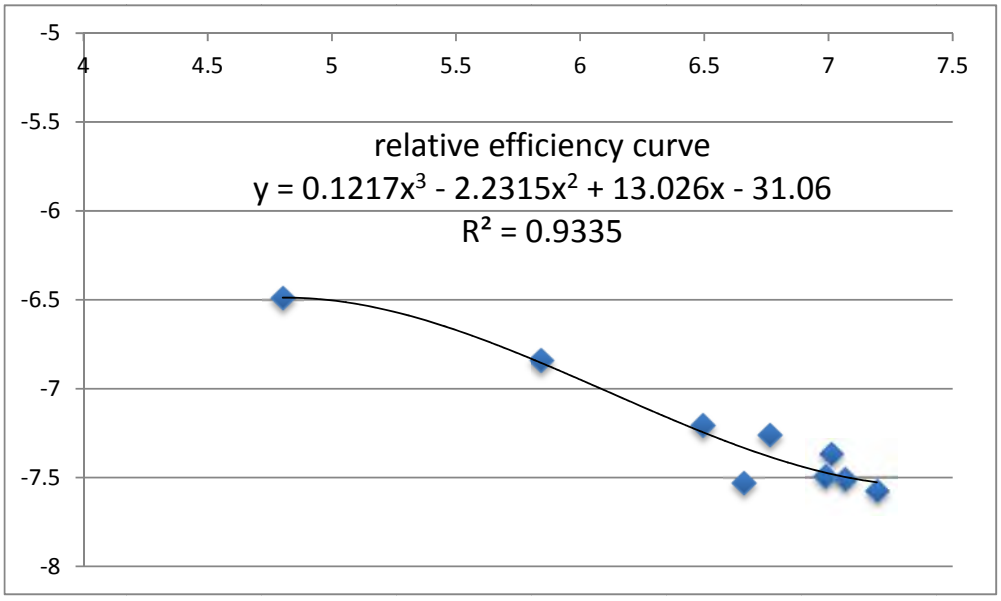

To Table of Contents

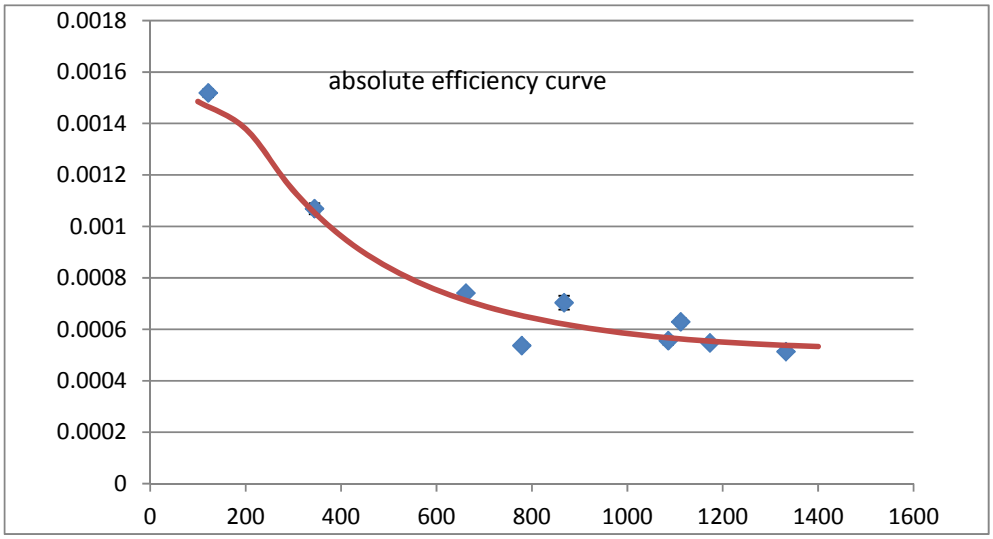

With the absolute efficiency curve, we find the efficiency at characteristic energies of the unknown samples and calculated the activity of them, activity=relative efficiency/absolute efficiency. The activity of sample 3 is, Co57 at 6.25uCi, Mn54 at 7.47uCi, and Co56 at 4.61uCi. The activity of sample 5 is, Co57 at 6.97uCi, Mn54 at 8.27uCi, and Co56 at 4.25uCi. The activity of sample 7 is, Co57 at 6.68uCi, Mn54 at 7.50uCi, and Co56 at 10.16uCi. The activity of sample 4 is, Eu 152 at 0.15uCi. And the activity of sample 6 is, Cd 109 at 4.91uCi.

Reference

Rolfs, Claus E, Rodney, William S. Rodney,(1995) Cauldrons in the Cosmos

Glenn F Knoll, (2000) Radiation Detection and measurement

Accelerator Mass Spectrometry (AMS) applied in the measurement of ^{93}Zr

Ruiyang Zhao

2013 NSF/REU Program

Physics Department, University of Notre Dame

Advisor: Philippe Collon

Abstract

According to the momentum-over-charge ratio (P/Q), the technique of mass spectrometry (MS) can be used to obtain particle separation using magnetic analysis. However, there are many limitations to this technique when the concentration of the radioisotope of interest is very low compared to the isobaric background. Accelerator Mass Spectrometry (AMS) can offer a better way to measure radioisotopes of very low concentrations by providing the possibility of using the standard detection method in nuclear physics. One of the experiments of the AMS group at the University of Notre Dame is to study the isotopes of Zirconium (Zr). Following the general principles of AMS, we designed, built and tested a Bragg peak detector in an attempt to provide better separation between ^{93}Zr and its isobar ^{93}Nb. We used it to trace different stable isotopes of Zirconium. We mapped ^{90}Zr through ^{94}Zr to predict the behavior of ^{93}Zr which is not stable and can only be found as a tracer in certain geological environments. The overall goal of the experiment is to allow the separation of ^{93}Zr from ^{93}Nb.

Introduction

Accelerator Mass Spectrometry is an analytical method which can be applied in the identification and the measurement of specific radioisotopes. This method applies standard nuclear detection techniques that rely on the measurement of a number of isotopic-specific properties such as time-of-flight (TOF), stopping power (dE/dX), total energy (E), and position of ions in a focal plane of magnetic spectrograph. The general principles of AMS are listed below.

- Ionization of the sample in an ion source.
- Initial low-energy selection which relies on the mass selection of the bending magnet.
- Acceleration to MeV energy using a tandem accelerator.
- Further high-energy selection.
- Particle identification of the radioisotope of interest using gas-filled magnet and ionization detector.

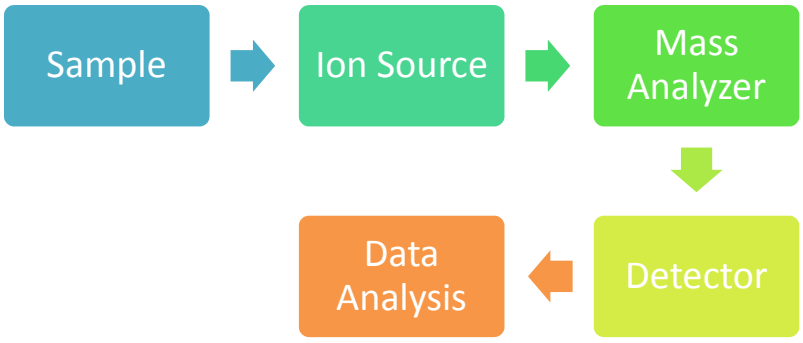

Figure 1

The general principles of AMS include four steps: ionization of the sample, acceleration of the particles, mass selection of the particles, data collection from detector and analyzation.

In the following, let's have a look at specific parts of a standard AMS beam line. The SNICS (Source of Negative Ions through Cesium Sputtering) ion source will supply the negative ions. The sample material is packed into a cathode that will be put in the back end of the chamber. Heating solid cesium will create a cesium vapor that will flow to the cathode and ionizer area. The material will form the negatively charged beam when it is sputtered by the Cs ion, and gaining an electron when passing through the cesium coating. A dipole magnet that is placed after the SNICS source will select the appropriate ion mass to be further accelerated. The negatively charged ions gain energy by being accelerated to the high positive voltage at the accelerator's center (i.e. terminal). At that location, some electrons will be stripped from the ions when passing through a carbon stripper foil. The ions become positive and are accelerated again from the high positive voltage on the termianal to the ground. Through a series of high-energy selection devices, such as analyzing magnets and a velocity filter (i.e. Wien filter), isotopic separation prior to isobar separation techniques is achieved.

Bragg curve detector

At the very end of the beam line, we need to set a detector which can do the necessary detections for our experiment. We designed, built and tested a Bragg peak detector. There are two parts in our detector, one is for position detection and the other is for energy detection. I took part in the process of assembling and testing this detector.

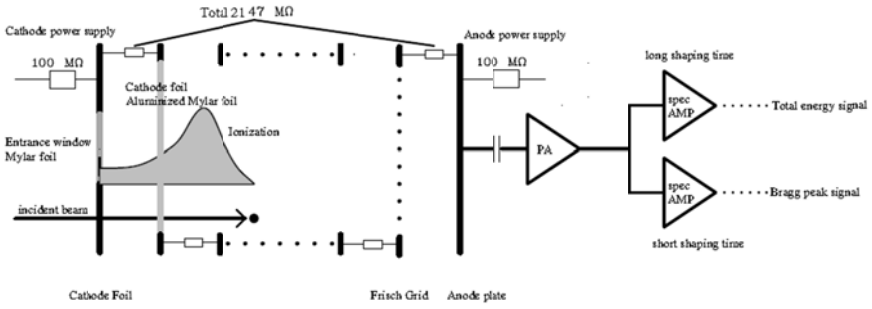

Figure 2

Bragg detector designed for the measurement of total energy and time of flight of the particles. The indicated voltages correspond to optimum values for detection of 135 MeV ^{93}Zr.

The figure above illustrates the structure of the energy detector (Bragg Curve Detector) Following our design, to form an even electric field, there are 21 resistors of 47MΩ between the cathode and anode, between which a voltage as high as 1000V can be applied. We use a capacitor to collect the ionization electrons to supply the signal we need. An Aluminized Mylar foil serves as the cathode. The Bragg detector has an applied electric field parallel to the incident particle direction and sufficient gas pressure to stop the particles in the active region. In this process, the incident particles will lose energy, ionize the gas and finally be stopped by the gas. The number of electron liberated during the ionization is proportional to the energy lost by the particles. Electrons will be collected on the anode side and deliver the signal across the capacitor. The signal we get from the detector will be separated and delivered to two amplifiers with different shaping times. The longer one outputs the total energy

signal and the shorter one output the Bragg peak signal.

Experiment and Analysis

The object of our experiment is to test whether the Bragg Curve Detector can allow a better separation between ^{93}Zr and its isobar ^{93}Nb through the measurement of its position, energy and timing.

Here is a table of the isotopes of Zirconium from ^{90}Zr to^{94}Zr. (Abundance and Half-life included)

Isotopes	**^{90}Zr**	**^{91}Zr**	**^{92}Zr**	**^{93}Zr**	**^{94}Zr**
Abundance	51.45%	11.22%	17.15%	Unnatural	17.38%
Half-life	**Stable**	**Stable**	**Stable**	**1.53×10^{6} y**	**Stable**

Table 1

Abundance and half-life time of the isotopes of Zirconium.

The dipole magnet which is placed after the SNICS source will select the appropriate ion mass to be accelerated. During the experiment, the magnetic fields, the bending radius and charge are constant. Therefore we need to change the energy of the isotopes in order to have the special isotope we interested to be injected.

$$\text{eq1: } R=\frac{\sqrt{2mE}}{qB}$$

In this experiment, we first set the tune to have 135MeV ^{90}Zr on the detector following the procedure outlined in Figure 1. This procedure is repeated for masses

91,92 and 94.

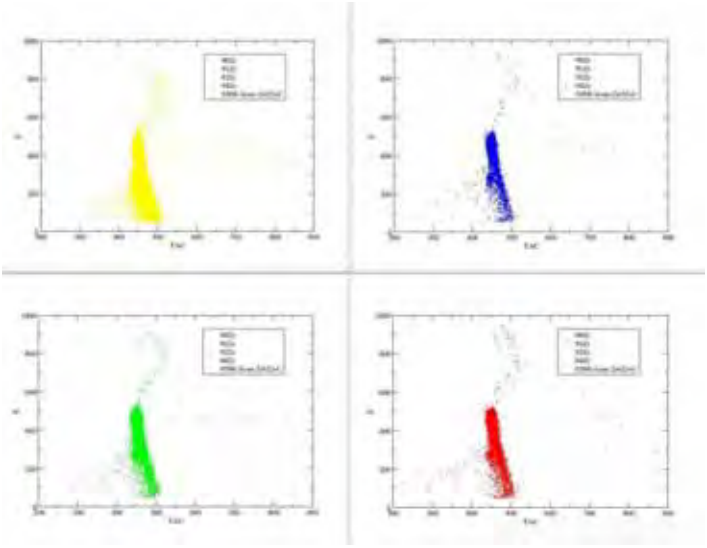

Figure 3

Total energy and time of flight of ^{90}Zr, ^{91}Zr, ^{92}Zr and ^{94}Zr. (from left to right and top to below)

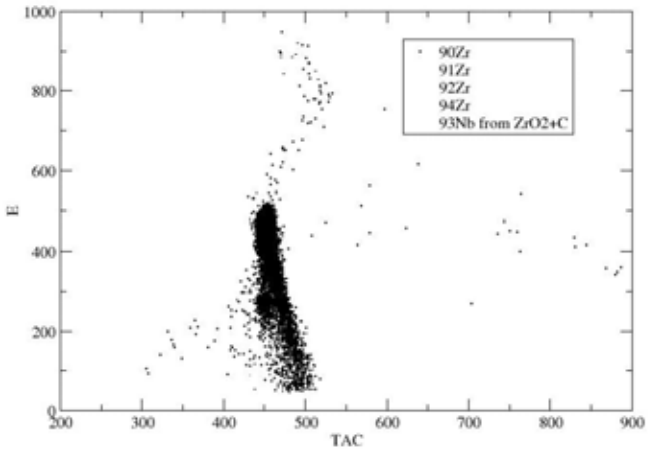

Figure 4

Total energy and time of flight of ^{93}Nb

To Table of Contents

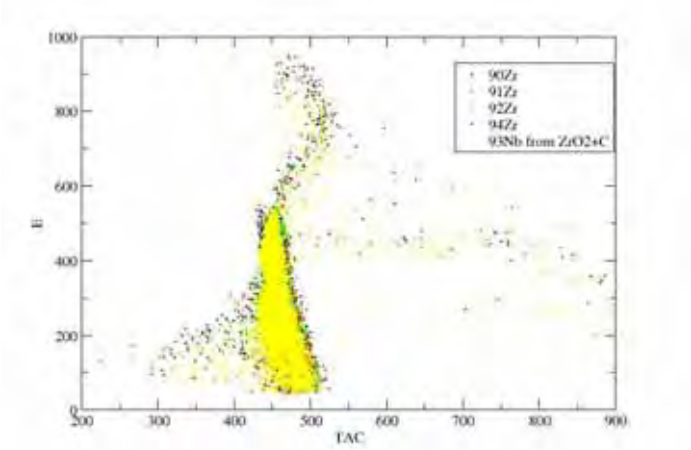

Figure 5

All data are shown in the same figure.

Shown in all the figures above, we can easily find all the 4 different isotopes of Zirconium and the Niobium have almost the similar region in the 2D graph. It means that it is hard to distinguish between ^{93}Zr and ^{93}Nb which is the isobar of ^{93}Zr.

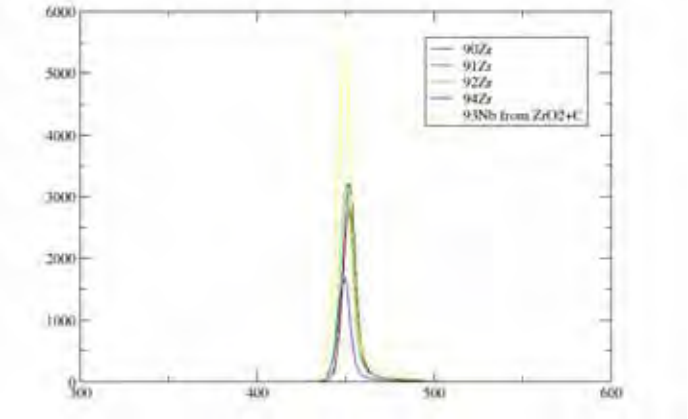

Figure 6

1D energy plot of ^{90}Zr, ^{91}Zr, ^{92}Zr, ^{94}Zr and ^{93}Nb. X axis is the energy, y axis is the counts

To Table of Contents

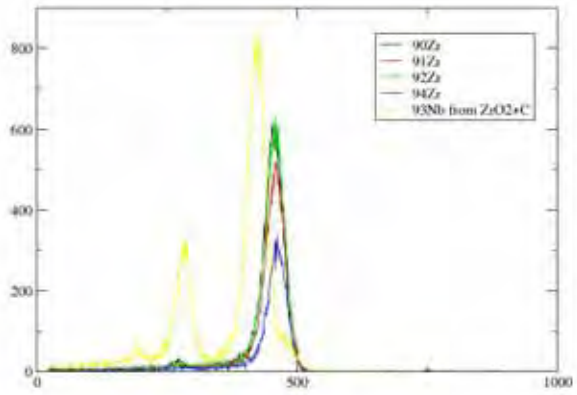

Figure 7

Time of flight of ^{90}Zr, ^{91}Zr, ^{92}Zr, ^{94}Zr and ^{93}Nb.

We can have a look at the total energy and time of flight of these ions in Figure 6 and Figure 7. In Figure 6, ^{90}Zr to ^{94}Zr have the same energy because they are Zr isotopes. But ^{93}Nb has a larger energy compared other ions. Similarly, shown in Figure 7, ^{93}Nb differs with other ions in the time of flight because it loses energy differently and stops at different depth inside the detector.

Conclusion

In our experiment, we tried to predict how the ^{93}Zr behave under standard AMS techniques. With the Bragg peak detector designed, built and tested by ourselves, we ran the experiment with ^{90}Zr, ^{91}Zr, ^{92}Zr and ^{94}Zr in order to find the behavior of ^{93}Zr. After comparing with ^{93}Nb, we found the current setting does not have a desirable separation between ^{93}Zr and ^{93}Nb.

References

[1] Nuclear Instruments and Methods in Physics Research A273(1988)262-272

[2] EMAS5 00068

[3] http://physics.nd.edu/research/research-groups/nuclear-physics-group/